6-1-2015

Ti-based functional nanoarchitectures for enhanced drug eluting stents

Yomna Emad Saleh

The American University in Cairo

School of Sciences and Engineering

Nanotechnology Program

Ti – Based Functional Nanoarchitectures For Enhanced Drug Eluting Stents

A Thesis in

Nanotechnology

By

Yomna Emad Saleh

Submitted in Partial Fulfillment of the Requirements

for the Degree of Masters of Science in Nanotechnology

May 2015

The American University in Cairo

Ti – Based Functional Nanoarchitectures For Enhanced Drug Eluting Stents

A Thesis Submitted by

Yomna Emad Saleh

To the Nanotechnology Graduate Program

May 2015

Has been reviewed and approved by:

Nageh K. Allam

Assistant Professor, Physics Department, The American University in Cairo.

Director, Energy of Materials Laboratory (EML)

Thesis Advisor

Mayyada El Sayyed

Assistant Professor, Chemistry Department, The American University in Cairo.

Internal Examiner

Amany A. Mostafa

Professor, Biomaterials Department, The National Research Center, Cairo, Egypt.

Director, Nanomedicine and Tissue Engineering Lab., Medical Research Center of Excellence,

The National Research Centre, Cairo, Egypt.

External Examiner

Hanadi G. Salem

Professor, Materials and Manufacturing Area, Department of Mechanical Engineering.

Director, Nanotechnology Graduate Program, The American University in Cairo.

Thesis Moderator.

*Signatures are on file in the Graduate program.

ABSTRACT

Ischemic events associated with coronary heart diseases (CHD) are the leading cause of death worldwide for both genders. They are directly associated with restricted blood flow caused by accumulation of atherosclerotic plaque in vessel's lumen. Percutaneous coronary intervention (PCI), including stent deployment, is currently considered as the dominant procedure for mechanically recovering myocardial perfusion to avoid lethal ischemic events. As vascular prosthesis, coronary stents suffer from two major and common complications; thrombosis and restenosis. Thrombosis is linked with insufficient migration of endothelial cells (EC) and proliferation at site of tissue injury. Restenosis is caused by unwanted proliferation of underlying vascular smooth muscle cells (VSMC). With drug eluting stents (DES) as a strategy to mitigate aforementioned complications, it only results in reducing VSMC proliferation. However, it directly causes poor endothlialization through undifferentiated inhibition of endothelial cells as well. This can result in high risk of late thrombosis, leading to death.

Different strategies are being investigated to reach optimum duration and conditions for endothelium healing as a critical aspect of enhancement for drug eluting stents. In this thesis, a nanoarchitectured system is proposed as surface enhancement for drug eluting stents. Highly oriented nanotubes were vertically grown on the surface of a biocompatible Ti-based alloys, as potential material for self-expandable stents. The fabricated nanoarchitectured system is self-grown from the potential stent substrate. This material is also proposed to enhance endothelial proliferation while acting as drug reservoir to hinder VSMC proliferation.

Two morphologies were prepared to investigate the effect of structure homogeneity on the intended application. They were characterized for morphological investigation using Field-emission scanning electron microscope (FESEM), X-ray diffraction (XRD), Raman spectroscopy, Energy dispersive X-ray spectroscopy (EDX) and X-ray photoelectron spectroscopy (XPS). Nanoindentation technique was used to study the mechanical properties of the fabricated material. Cytotoxicity and proliferation studies were done and compared for the two fabricated nanoarchitectures versus smooth untextured samples using *in-vitro* cultured endothelial cells. Finally, drug loading capacity was investigated practically and supported by computational study of release profile using COMSOL® Multiphysics software.

DEDICATION

" قُلْ إِنَّ صَلاَتِي وَنُسُكِي وَمَحْيَايَ وَمَمَاتِي لِلّهِ رَبِّ الْعَالَمِينَ"

"Verily, my Salat (prayer), my sacrifice, my living, and my dying are for Allah, the Lord of the 'Alamin (mankind, jinns and all that exists)"

The Noble Qur'an, Surat Al-Anaam, Verse No: 162

ACKNOWLEDGEMENTS

First I would like to express my sincere gratitude to my advisor, Dr. Nageh Allam for his ongoing support along the duration of my studies and research work. He has been a leading example for commitment and dedication to me and the whole group. He made me appreciate the process of learning more by time. He always reminded me why I love science through his passion towards it. I learned from you how to learn. Thanks a lot for everything.

Am as well grateful for all my professors, who taught and guided me during the course of my studies within the Nanotechnology program. I would like to specially thank Dr. Hanadi Salem, Dr. Adham Ramadan and Dr. Mohab Anis. I learned a lot from your courses way beyond the educational content alone. I enjoyed the multidisciplinarity of the program, it certainly opened for me a lot of doors for future learning.

Special thanks to Dr. Mohamed Gepreel from Egypt-Japan University of Science and Technology for supplying me with the alloy samples.

I would like to also thank all my colleagues in EML group for their continuous support and motivation. Special thanks to Basamat for her kindness and guidance since the first day I joined the group, Mohy and Amer for their dedication to make sure the Lab is always supported, you are the group's backbone, Salama for support with SEM imaging and Hafez with computational simulation.

I am thankful for my colleagues at the STRC for their continuous support to my research work. Thank you so much Ghazaly Asmaa and Ehab. Also, researchers, chemists and friends at the Chemistry department. Isra, Yasmine, Samar, Ghada, Raghda, Ahmed Omaia, Mr. Emad and Mr. Mahmoud.

I would like to express my endless appreciation to my parents and my sisters. To my father for his continuous support and encouragement. And to my sisters Haneen and Maram, my lifetime friends, companions and my backbone. I would love to take this opportunity to specially thank my mother, my number one teacher. I learned everything from her. I learned to work hard, to always seek to be better, to do my best and have faith in my capabilities. I am nothing without you, thanks for being always there for me and for everything.

Rua, Worood, Shaimaa and Nada, I can't thank you enough for your support and motivation. You are life time keepers and I wouldn't have been able to go on without you. Although we didn't work in one laboratory, but your fingerprints are all over everything I've done. AUC is not only granting me a degree, but also a gift of friends, who I will always be grateful to have.

I am grateful to have a big support system of friend that have always believed in me and pushed me toward achieving my goals. Samar, Rana, Mai, Lana and Aya thank you for always being there for me in every aspect of my life and for making me always remember what life is actually about. Last but definitely not by any means the least, I would like to specially thank Mahmoud for being the inspiration behind the thesis topic, for giving me guidance, supporting me every single day, and offering me a blessing of having someone to always rely on. You give me confidence, comfort and energy. Thank you for being my best friend.

Table of Contents

List of Figures

List of Tables

List of Abbreviations

Anti-EPC: Anti-Endothelial Progenitor Cells

BAEC: Bovine Aortic Endothelial Cells

BMS: Bare-Metal Stents

BX: Balloon Expandable Stent

CABG: Coronary Artery Bypass Graft

CAD: Coronary Artery Disease

CAS: Coronary Artery Stenting

CHD: Coronary Heart Diseases

DAPT: Dual Antiplatelet Therapy

DES: Drug Eluting Stents

EC: Endothelial Cells

ECM: Extra-Cellular Matrix

EDTA: Ethylene Diamine Tetraacetic Acid

EDX: Energy Dispersive X-ray Spectroscopy

FDA: Food and Drug Administration

FESEM: Field Emission Scanning Electron Microscope

Hap: Hydroxy apatite

HDL: High-Density Lipoprotein

HPLC: High Performance Liquid Chromatography

LDL: Low-Density Lipoprotein

MRI: Magnetic Resonance Imaging

MSC: Mesenchymal Stem Cells

NTs: Nano-Tubes

PBS: Phosphate Buffer Saline

PTCA: Percutaneous Transluminal Coronary Angioplasty

PCI: Percutaneous Coronary Intervention

SX: Self-Expandable Stent

VSMC: Vascular Smooth Muscle Cells

WCA: Water Contact Angle

XPS: X-ray Photoelectron Spectroscopy

XRD: X-Ray Diffraction

Chapter 1: Introduction and Scientific Background

Chapter 1: Introduction and Scientific Background

1.1. Coronary Heart Disease (CHD)

Coronary heart disease (CHD) is described as the leading cause of death worldwide for both genders, especially in high and middle-income countries. It is responsible for 30% of deaths annually around the world and the death of almost 700,000 patients in the United States of America alone every year [1–3]. It has been intrinsically associated with atherosclerosis since the beginning of the 20th century [1]. Atherosclerosis is a degenerative disease that can begin as early as adolescence or childhood. It progresses silently until adulthood, when it can be manifested into clinical CHD that may end with death [4]. Pathologically, atherosclerosis is characterized by the formation of localized plaques within arterial walls that hinder normal blood flow [5].

As shown in Figure 1.1, atherosclerosis starts with the accumulation of fatty streaks, cholesterol deposits and its esters in arterial intima. Later, larger lipid deposits and cellular waste are accumulated and covered by a thick intima of connective tissue and smooth muscles, resulting in a fibrous plaque. That fibrous plaque can either stay stable and get calcified or can erode exposing the inner core to flowing blood, which in turn may accumulate into occlusive thrombus [4]. When atherosclerotic plaques are localized in one or more of coronary arteries – known as coronary artery disease (CAD) – they prevent sufficient flow of oxygenated blood to the heart muscles. This results in an ischemic state at the heart muscle causing symptomatic events that range from angina pectoris to myocardial infarction and sudden death [6], see Figure 1.2.

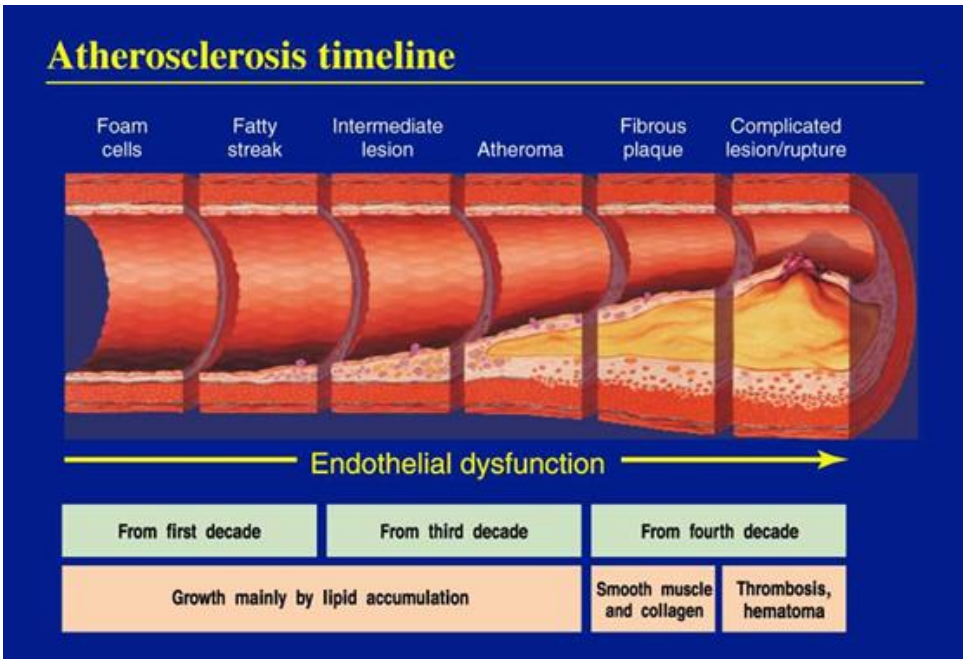

Figure 1.1: Schematic representation of atherosclerosis timeline pathologically [7]

The clear-cut cause of atherosclerosis is not well-identified up till now. However, several risk factors were highlighted to significantly contribute in disease progression; such as hypertension, diabetes mellitus, smoking and most importantly uncontrolled blood lipid profile [1]. Further identification of cholesterol role was revealed when high blood levels of low-density lipoprotein (LDL) cholesterol accompanied higher rates of CHD incidence, while high blood levels of high-density lipoprotein (HDL) cholesterol were associated with lower rates of CHD incidence. This was further confirmed via controlled clinical trials conducted to clear out controversy about lipid hypothesis [4].

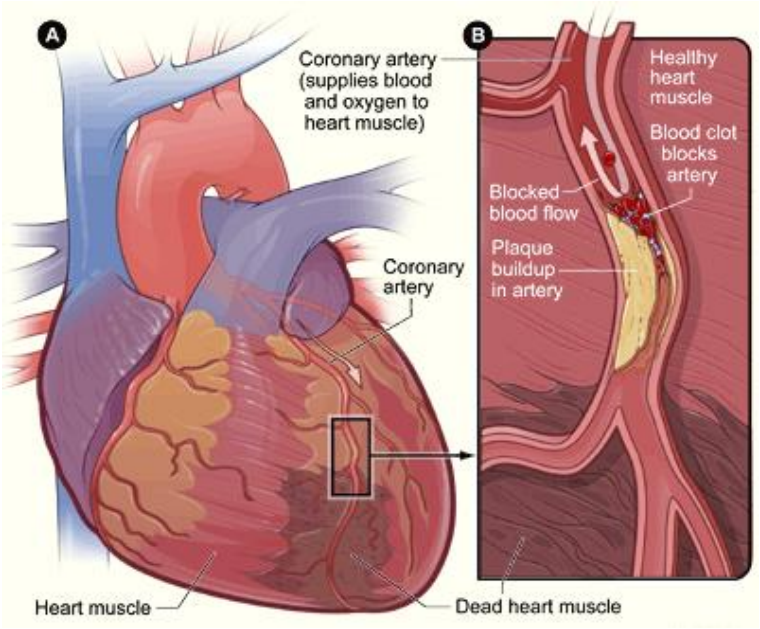

Figure 1.2: (A) death of part of heart muscle due to insufficient blood supply (B) Cross section of coronary artery with plaque built up and blood clot [8].

1.2. Coronary Artery Stenting (CAS)

1.2.1. Percutaneous Transluminal Coronary Angioplasty (PTCA)

A number of practices is well-established for the treatment of atherosclerosis in order to restore coronary blood flow [9]. For long time, coronary artery bypass graft (CABG) remained the gold standard practice for coronary artery disease treatment. CABG, however, involves an invasive intervention to bypass blocked artery using a graft harvested from other body parts. This is accompanied by either during or post-surgery morbidity and mortality risks. In 1977, the first percutaneous transluminal coronary angioplasty (PTCA) was performed to replace CABG as a minimally invasive technique that spare CAD patients post-surgical risks and complications [1]. PTCA involves the insertion of a balloon-tipped catheter through a small incision at a major limb artery. The catheter is guided over a thin radio-opaque wire that allows the procedure to be visible under the fluoroscope x-ray imaging. Contrast agents are injected in the circulation

concurrently to locate the site of the blockage. Upon reaching the site of occlusion, the balloon is then inflated to cause plaque compression and/or destruction, dilatation of arterial stenosis and allows the blood flow restoration, then the balloon is removed [10, 11], see Figure 1.3.

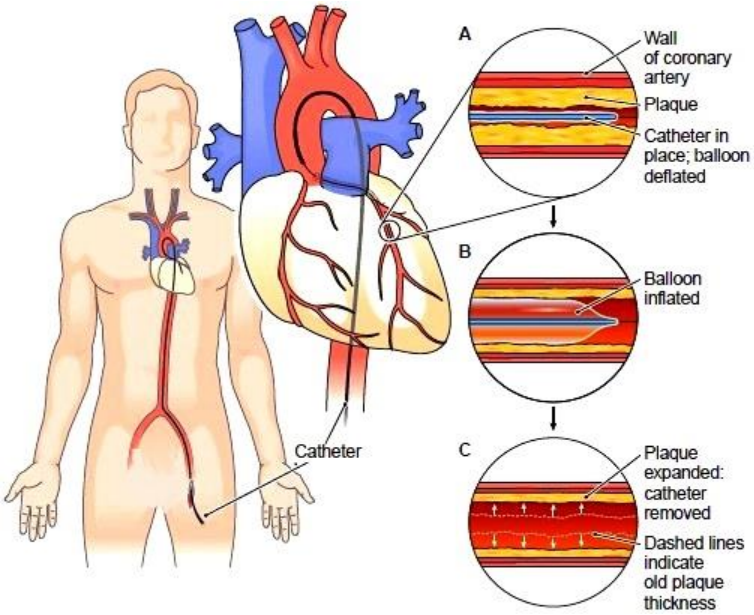

Figure 1.3: Description of PTCA from site of catheter insertion till (A) reaching diseased site, (B) Balloon inflation and (C) Blood flow recovery after balloon removal [12].

The success of the previously described plain balloon angioplasty was, however, threatened by the risk of re-narrowing and possible need of emergency CABG. It was noticed that post-procedural arterial response involved 5% risk of acute restenosis during the first 24 hours, or 20-50% risk of late occlusion during the first six months. After investigation, this was attributed to tissue trauma during the mechanical restoration of blood flow and morphological alterations that affected the arterial wall. Consequently, arterial smooth muscles undergo elastic recoiling and negative remodeling takes place through a decrease in external diameter of the artery during healing. To eliminate such serious complications, bare-metal stents (BMS) were introduced to act as a residing scaffold to prevent arterial collapse incurred by plain balloon angioplasty [10,13]. Stents are expandable wire-meshes in the form of tubes, which come in a wide range of designs

and materials, based on implantation procedure and patient's case. As shown in Figure 1.4, they are used as a supporting structure to prevent the artery from collapsing after balloon angioplasty to maintain blood flow [10,14].

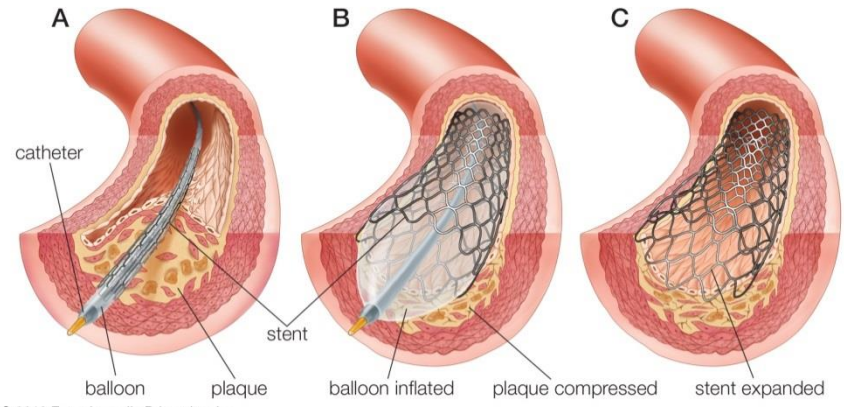

Figure 1.4: Stent delivery mounted on a balloon-tipped catheter during PTCA. (A) Stent crimped on deflated balloon, (B) stent expands with balloon inflation, and (C) balloon left in place after balloon removal [15].

1.2.2. Drug Eluting Stents (DES)

After the introduction of BMS to the angioplasty procedure, patients' follow ups and clinical studies showed that restenosis rates were only improved to 20% - 30% [16], while in patients with complex lesions, such rates can go up to as high as 60% [11]. Further investigation attributed the renarrowing at the treated location to what is known as neointimal hyperplasia. Hardly controllable intima reaction and hyper proliferation of the vascular-lining tissue led to in-stent occlusion, which required medical re-intervention [10,14]. Clinical studies that investigated the potential of avoiding this complication using systematic drugs such as antithrombotics and glucocorticoids have generally failed [17]. In a more successful attempt to reduce the number of patients that suffer from recurrent stenosis and clinical CHD, a therapeutic agent was introduced locally on the stents platform to combat hyperplasia, offering what is known as drug eluting

stents (DES) [1]. DES successfully emerged to revolutionize the field of intervention cardiology with decreased restenosis rates below 10% [18]. They became more preferred choice although they were only introduced in 2003. By 2006, 8 out of 10 deployed coronary stents were DES [19], at an annual cost between 4 to 5 billion USD [20].

The emergence and development of DES is considered a successful example of multidisciplinary research that offers a life-saving solution to one of the most prevalent death-causing problems worldwide. It combines the understanding of the restenosis biology, pharmacology and appropriate drug selection, drug release and delivery strategies as well as material in-depth studies [22, 23]. The drug is meant to inhibit neointimal hyperplasia by suppressing one or more processes involved in the biology of the restenosis. Accordingly, therapeutic modalities of the loaded drug can be classified mainly into antiproliferative, anti-inflammatory, migration inhibitors and immunosuppressive as well as prohealing and anti-thrombotic agents [24, 21]. These types of DES and most famous examples from each class are summarized in Table 1.1.

Clinical evaluations have so far overwhelmingly showed strong evidence of DES superiority over BMS in reduction of in-stent restenosis rates. However, cases of serious clinical events have raised concerns over DES long time safety and efficiency [6]. In particular risks of late and very late stent thrombosis are considered [25]. Several proposals have been offered to explain why such technical marvels would turn to be thrombogenic. Some of the most supported reasons are; 1- delayed endothelialization due to locally delivered cytotoxic or cytostatic drugs or other pathological risk factors, 2- inherent thrombogenicity of the stent as a foreign body to blood circulation, 3- hypersensitivity reactions related to the metallic material used for stent manufacturing or/and polymeric coatings used as drug carriers, 4- dual antiplatelet therapy (DAPT) early discontinuation, and 5- stent malapposition or incomplete apposition, related to technical deployment [26–29].

Table 1.1: Types of DES and most famous examples from each class [21].

Anti-inflammatory Immunomodulators	Anti-proliferative	Migration inhibitors, ECM* modulators	Promote healing and endothelialization
Dexamethasone M-prednisolone Interferon γ-1b Leflunomide Sirolimus (and analogues) Tacrolimus Mycophenolic acid Mizoribine Statins Cyclosporine Tranilast Biorest Abciximab	QP-2, Taxol Actinomycin Methotrexate Angiopeptin Vincristine Mitomycin Statins C-MYC antisense Sirolimus (and analogues) RestenASE 2-chloro-deoxyadenosine PCNA ribozyme Abciximab	Batimastat Prolyl hydroxylase inhibitors Halofuginone C-proteinase inhibitors Probucol Abciximab	BCP671 VEGF Estradiols NO donors EPC antibodies Biorest Advanced coatings Carvedilol Abciximab

*ECM: extracellular matrix, PCNA: proliferating cell nuclear antigen, VEGF: vascular endothelial growth factor, NO: nitric oxide, EPC: endothelial progenitor cell

Accordingly, the Food and Drug Administration (FDA) has increased the recommended duration for systematic DAPT to double it into at least one year, to reduce the incidence of late stent thrombosis [30]. Such increase has multiple side effects such as high risk of bleeding, complicated patient management after any surgical procedure and high costs. Therefore, current research is concerned with improving DES performance and long-term safety, using different approaches and multidisciplinary solutions that tackle any or all of the previously mentioned causes of thrombosis, while sparing the need of long-term DAPT [6, 25].

1.3. Material Perspective for Stent Substrate

A wide range of different materials has been used in the manufacturing of stents. These materials need to fulfill a number of rigorous properties; mechanical, physical and chemical ones. According to procedure of implantation, long term application and safety, these properties are strongly studied and directly affect the choice of stent [14]. An ideal stent has been described with many characteristics in plentiful reviews. They should generally possess (1) low profile, i.e. easily crimped on the balloon-tipped catheter for facile deliverability; (2) flexibility to travel through narrow vessel whenever needed; (3) satisfactory radio-opacity to be visible for the clinician during the procedure; (4) acceptable expandability ratio, i.e. as the balloon is inflated, the stent should be able to expand sufficiently and conform to the morphology of the vessel; (5) adequate radial strength supported by high tensile strength, i.e. stent should withstand imposed force by the arterial wall and avoid collapsing; (6) biocompatibility to avoid platelets adhesion and inflammatory reactions; (7) capacity to deliver drug locally to treated site; (8) compatibility with magnetic resonance imaging (MRI). In addition, an ideal stent material would have high elastic modulus to avoid recoiling, and low yield strength to expand during deployment at acceptable balloon exerted pressure [16,31].

1.3.1. Permanent Stents

Medical implants in general are not only made of metals, but also ceramics and polymers. However, ceramics and polymers lack few of the previously mentioned critical properties needed for ideal stents, especially mechanical properties. Hence, metals are the main materials used so far for the manufacturing of coronary stents. Combination of properties described above is substantially difficult to meet in a single material. Therefore well studied compromise is always essential to be found, and research is still intensively ongoing to tackle this issue [31].

1.3.1.1 Balloon Expandable Stents

The metals commonly used in the manufacturing of stents are 316 L stainless steel (SS), cobalt-chromium (Co-Cr) alloys, platinum (Pt) alloys and Nitinol (Ni-Ti), which will be

specifically described in a later section, under "self-expandable stents". Table 1.2 summarizes the main mechanical and physical properties of such materials. SS, Co-Cr and Ni-Ti alloys are widely used in different biomedical applications due to their high corrosion resistance, high elastic modulus and high ductility. Although other materials can show better corrosion resistance and biocompatibility such as titanium (Ti) alloys, currently used Ti-alloys in biomedical field, such as Ti-6Al-4V alloy, lack sufficient ductility, strength and density needed for coronary stents [16,31]. Further details are presented below describing 316L SS, Co-Cr alloy and Pt alloys as they are the three most commonly used materials in manufacturing stents currently available in the market and Ti alloys as they are crucial for the scope of this thesis.

Table 1.2: Mechanical and physical properties for selected biomaterials, used for stent manufacturing [16,31].

	SS 316L	Co-Cr (L605)	Nitinol	Pt-10Ir	Ta	Cp-Ti
Density (g/cm^3)	7.95	9.1	6.45	21.55	16.6	4.5
Elastic Modulus (GPa)	193	243	90	150	185	107
UTS (MPa)	670	1147	1400	340	207	760
Yield Strength (MPa)	366	629	195–690	200	138	485
Elongation (%)	43	46	14	25	25	30

Stainless steel (SS) is iron-based alloy that can be prepared in different grades used for different applications, according to the desired properties. These grades are differentiated according to the type and percentage of added elements that comprises the alloy along with iron. These elements include Ni, Cr, Mo, Nb, Ti, and N, and they directly affect the alloy's strength, microstructure and corrosion resistance. Although SS does not corrode in oxygen containing environment. However, they may locally corrode in chloride containing media such as human fluids [16,31,32].

Austenitic 316L SS has sufficient mechanical properties making it well-suited for stent application and the main metal used for stent manufacturing for a long period of time, see Table 1.2. The corrosion resistance of SS is increased by adding up to 3% Mo, and up to 15% Ni, while reducing carbon content below 0.030% [31,33]. However, with such relatively high content of Ni as well as presence of Mo and Cr, these ions can be released to the surrounding tissues causing local immune response and allergic reactions, which would contribute significantly to in-stent restenosis. Also, carbon content can result in the formation of carbides at the grain boundaries reducing the corrosion resistance at those areas. Moreover, with more than 60% Fe content in SS it possesses ferromagnetic properties that would clinically interfere with MRI that the patient may need to undergo. While on the other hand, it has relatively low density that hinders sufficient visibility during PCTA procedure. Therefore, the use of SS is dependent on the use of coating material that would solve some of the challenges mentioned above, yet may not be able to solve others [34,35].

Co- Cr alloys have been used broadly in biomedical applications for decades and have been replacing SS stents commercially in the past few years along with Pt-alloys. They have outperformed SS both during and post deployment [16,31]. As seen in Table 1.2, they have higher density that makes them more radiopaque and facilitate guidance during angioplasty. They have high tensile strength, which allows for thinner struts for better deliverability and lower rates of stent fracture [36]. They are also characterized by high elastic modulus limiting stent recoiling. Moreover, they demonstrate high corrosion and wear resistance, which reduce the risk of late complications [37,38].

Pt alloys possess great potential in the field driven by their biocompatibility, anti- corrosion and improved radiopacity [31]. For example Pt-Cr alloy showed enhanced endothelialization, high corrosion resistance and comparable mechanical properties to stainless steel due to its chromium content [39]. While Pt-Ir (90% Pt – 10% Ir), for example, showed enhanced radiopacity, reduction in inflammatory reactions and incidence of thrombosis. However, they showed higher rate of recoiling and their mechanical properties are still under question [40].

Titanium (Ti) and its alloys have been widely used in biomedical field especially in dental and orthopedic applications. They show excellent biocompatibility and high corrosion resistance due to the oxide layer formed on their surface, which is highly stable. However, for coronary stent manufactory, Ti application has been limited to bio-inert coatings that showed significantly reduced thrombogenicity and intimal hyperplasia, such as Ti-nitride-oxide layer on Titan© stent (Hexacath, France) [16,31,41]

The reason why pure titanium or some of its common alloys are not used as stent material is due to its mechanical properties that does not match the requirement of ideal stent. It has high yield strength but relatively low tensile strength. Therefore, during deployment with balloon expansion, they will need to expand to stresses beyond their yield strength. Furthermore, with Ti-alloy low tensile strength and low ductility, the stent will be easily prone to fracture. Using materials in the alloy that would reduce its yield strength might be a good strategy to make it mechanically acceptable, while keeping the original tensile strength. Some of the promising Ti-alloys for making stents are Ti-based Tantalum (Ta) and Niobium (Ni) alloys, which showed outstanding haemocompatibility [42]. Also, Ni-Ti alloys are extensively used in stents manufacturing at almost equal percentages of both elements. This will be briefly discussed below under "self-expandable stents" section [43].

1.3.1.2. Self-expandable Stents

One of the stents classifications depends on method of deployment into the vessel during the PCTA. Accordingly, they are classified into balloon expandable stent (BX) – as described previously and shown in Figure 1.4 – and self-expandable stent (SX), see Figure 1.5. BX is manufactured crimped and mounted on a balloon that inflates at the required site expanding the stent along with the balloon inflation. SX is manufactured at or slightly above vessel diameter then constrained in the crimped state within a sheath till it reaches site of delivery [44]. Therefore, materials used for BX should have the ability to undergo plastic deformation during deployment, and then preserve required size once positioned. However, materials for SX should have enough elasticity to be compressed while delivered, and then expand in place [14,16]. And it is fair to say that balloon expandable stents resist balloon expansion, whereas self-expandable ones assist it.

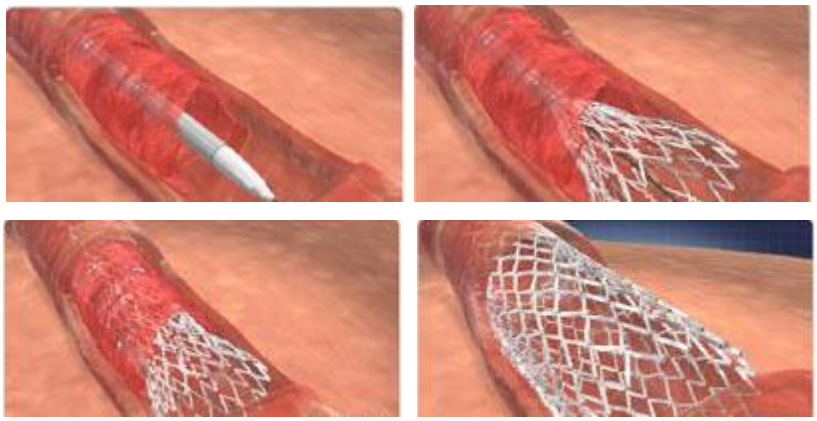

Figure 1.5: Self-expandable stent; introduced crimp within a sheath. After reaching delivery site, sheath is removed and the stent expand to its original shape [45].

BX can suffer from mechanical failure and collapse if subjected to external pressure that exceeded its critical value. While on the other side, SX will not suffer from same strength limitation by virtue of its elastic properties that permit its radial recovery. Also, SX was found to be superior to BX in maintaining vessel radial compliance after stenting, which is a measure of yielding to pressure without disruption. Therefore, if a healthy vessel would have 6%/100 mmHg compliance normally, this number would be 3-4%/100 mmHg compared to less than 1%/100 mmHg compliance after SX and BX stenting, respectively. Furthermore, bending compliance is higher for SX, which gives an advantage at both delivery and deployment. This leaves the stent more conformable and adaptable to vessel shape avoiding high stresses at the end of the stent, which may contribute to intimal hyperplasia. However, on the other hand, concerns regarding SX are still raised due to risk of acute recoil with calcified lesions, recovery from buckling with large stents and placement technical challenges [44,46].

One of the most widely used materials for self-expandable stent manufacturing is Nitinol (Ni-Ti alloy). It consists of approximately equal atomic amounts of both nickel and titanium; 49.5-57.5% wt% Ni and the rest is Ti [16,31]. They have unique mechanical properties that highly favor their use in SX, such as shape memory and superelasticity. Shape memory effect allows the material to return from its deformed shape into its original one by heating. Superelasticity allows apparent plastic deformation to return to original shape when load is released. Nitinol SX are

manufactured at a size slightly higher than vessel diameter. They deform plastically under room temperature and are crimped onto delivery system. Under the effect of body temperature, they expand to regain their original shape conforming to the vessel diameter. As shown in Figure 1.6, Nitinol has similar behavior to natural body structural materials such as bones, hair and tendons. These materials can be deformed elastically up to 10% strain. Such strain can be recovered at lower stresses after the release of the stress, and loading/unloading curves are characterized by the so called hysteresis [31,43].

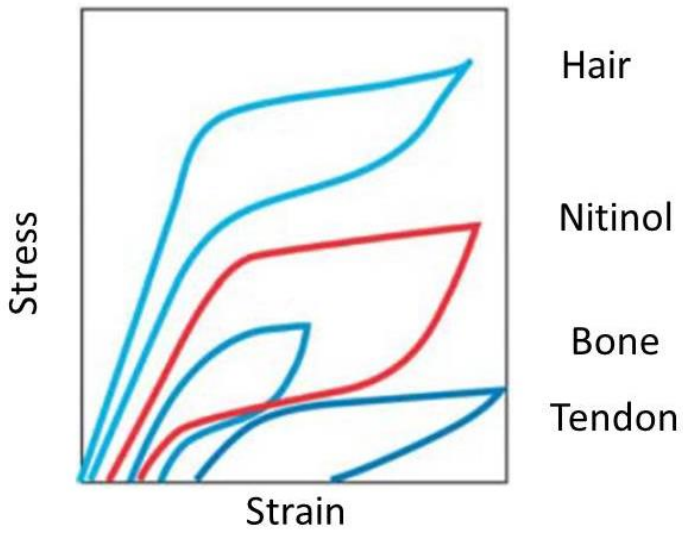

Figure 1.6: Mechanical compatibility of Nitinol with body structural material [43].

1.3.2. Biodegradable Stents

Basically, stents are supposed to function as a mechanical support for the blood vessel and prevent acute recoiling until endothelial tissue is regenerated and regain its integrity. Hence, the stent role is temporary and long term existence can be unnecessary. The concept of biodegradable stent became, therefore, very appealing and drew the attention of research community as well as stents industry. It spares patient from long term complications such as risks of in-stent restenosis, late stent thrombosis, persistent vessel stiffness and incompatibility with future interventions [47].

Ideal biodegradable stent material should be able to compromise mechanical integrity versus degradation on implantation site. As shown in Figure 1.7, degradation would begin theoretically at low rate when mechanical integrity is still needed and maintained. After a period of 6-12 months, vessel remodeling is believed to be completed, hence higher rate of degradation thereafter is acceptable. Two classes of materials are used for biodegradable stents; metallic materials such as Mg- or Fe- based alloys, and polymeric materials such as lactic, glycolic and caprolactone families. Although biodegradable stents witnessed high research and market interest, many concerns are yet to be evaluated and answered before replacing current technology. These concerns include safety issues regarding degradation products and degradation mechanism [48], as well as practical implication of mechanical compromise over time that was discussed above.

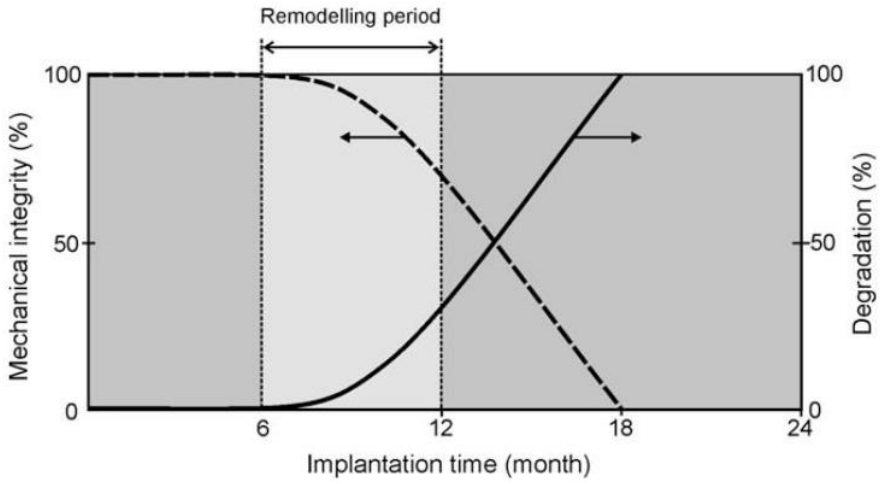

Figure 1.7: Theoretical material biodegradation over time, versus its mechanical integrity [47].

1.4. Surface Treatment

1.4.1. Polymeric Coating

Coatings have been initially used to enhance the biocompatibility of stent materials within vascular environment. Later, they were used as vehicle for drug loading and a platform to offer advanced solution for better endothelialization. Currently, the most widely used coating materials for different types of stents are polymeric coatings [16]. Permanent polymer coatings, which have been used initially for DES, showed impaired vascular healing and were found to be responsible for inflammatory responses due to permanent contact with the arterial wall [49]. It carried the blame on late stent thrombosis along with other patient and lesion related factors [50].

Biodegradable polymers have, therefore, appeared to be an appealing alternative to durable polymers as stent coating. They are more likely to avoid chronic inflammatory response and long term complications, as they degrade over certain amount of time and their degradation product theoretically get washed out from human body. Materials used for such coatings may include poly lactic acid (PLA), poly lactic-co-glycolic acid (PLGA) and poly caprolactone (PCL) [48]. Drug release is controlled with these materials based on their degradation profile over time. Challenges are though still remaining for advancement in polymeric coatings. These challenges include for example; establishing optimal formulation and degradation time, pharmacokinetics of drug release during degradation and fate of degradation by-products. [50].

1.4.2. Nanoporous Surface

Reference to polymer-related concerns described above, porous platforms offer a promising step forward in the advancement of DES as polymer-free surfaces. They avoid polymer long term inflammatory responses, improve healing process, improve surface integrity by avoiding polymer peeling and can still act as drug reservoirs. Moreover, they were found to promote rapid endothelialization. This was first investigated by creating micropores on the vascular graft wall, as shown in Figure 1.8, using different techniques [51–53].

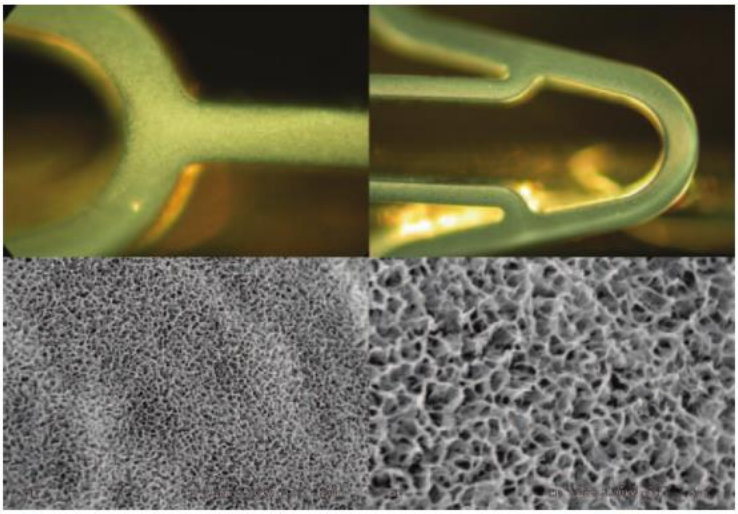

Figure 1.8: VESTAsync DES system. Top images picturing stent struts at different magnification and bottom ones are SEM (Scanning Electron Microscopy) images of their microporous Hap (Hydroxy apatite coating [51].

It was found that increased pore density resulted in an enhanced endothelialization and formed thinner intima [54]. Also to better control sustainable release of the drug from the porous reservoir and avoid burst effect, smaller pores may be required to retard quick release [16]. Hence, the use of nanotechnology advances in stents surface treatment is investigated in attempt to fulfill such favored requirements. It involves the design and development of structures and materials with at least one dimension ranging in size between 1- and 100- nanometer. Such size allows the structure to manipulate matter at its atomic scale, offering exceptional opportunities at biological interfaces. Using nanoporous assemblies on surface of graft material not only act as drug reservoir but also play a critical role in fast healing [55].

The concept certainly have merits and their positive influences on tissue regeneration have been already explored for different medical devices, however, research is still extensively required to study the potential use of this kind of surface treatment. Concerns that still need answers include; thrombogenicity of such rough surfaces, mechanical performance during and after deployment, drug-release profiles of different morphology and preparation techniques for controlled morphologies on the surface of different biocompatible materials [38].

1.4.3. Other Surface Treatment

A wide range of other coating types has been explored for stent material for different functional advantages [38]. For example, 1- anti-corrosive metal oxides such as titanium dioxide, significantly decrease metal ion release from core material enhancing biocompatibility; 2- silicon carbides that allow electron transfer between the metallic surface of the stent and blood proteins to reduce in stent fibrinogen deposition and stent thrombosis; 3- carbon coating for lower rates of metal ion release and platelet aggregation; 4- titanium- nitride-oxide coating as barrier against metal ion and to regulate endothelialization; 5- endothelial cells seeding on stent surface to promote endothelialization and fast healing; 6- biotechnology advances that use anti-endothelial progenitor cells (anti-EPC) in contact with blood flow to capture EPCs, which are seed for endothelial tissue growth, promoting controlled tissue growth (see Figure 1.9). Some of those previously mentioned approaches are proven clinically insignificant or even failed avoiding late complications, while others are being currently adopted commercially and considered state-of-the art material treatments, which are beyond the scope of this thesis and discussed efficiently elsewhere [16,25,29,31,38,50].

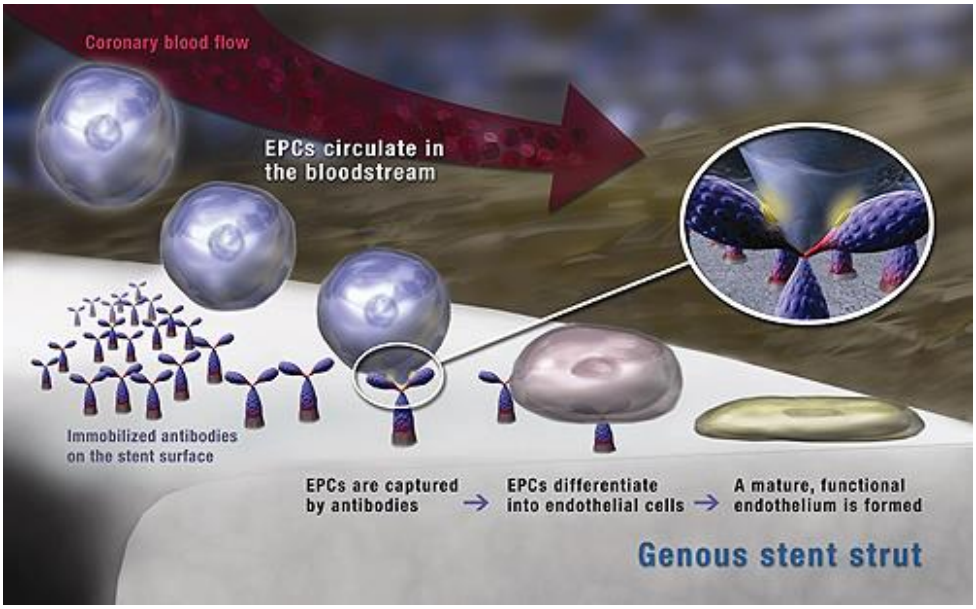

Figure 1.9: EPCs capturing technology by Genous ® stent for enhanced endothelialization [56].

Thesis Scope and objectives

Reference to the challenges facing Drug Eluting Stents (DES) described earlier in this chapter, we can summarize saying that ideal surface properties for DES should offer the following:

(1) Material biocompatibility.

(2) Pro-healing bioactivity to avoid neointimal hyperplasia, while promoting control endothelial healing.

(3) Capacity for drug loading.

(4) Mechanical integrity.

With the aim to fulfill these objectives, nanoarchitectures were investigated in this thesis as surface treatment for potential biocompatible DES material. As will be elaborated in chapter 2, nanoporous structures and nanotubes arrays were found to be very promising for enhancing tissue regeneration and as drug loading vehicle to be used for wide range of biomedical applications. For extending and supporting these efforts to be used for intravascular stents the following work will be covered in this thesis.

(1) Fabrication of nanoarchitectures on the following materials, a) pure titanium, b) Ti-45Ni alloy and c) Ti-17Nb-6Ta which possesses mechanical properties matching with those required for self-expandable stents.

(2) Studying different properties for fabricated nanoarchitectures through various characterization techniques. Characterization would include; morphological, mechanical, compositional and structural.

(3) Investigating the effect of different nanoarchitectures as surface treatment on biological response. And comparing their bioactivity versus smooth surface of the same material. This will be assessed through *in-vitro* studies using vascular endothelial cells.

(4) Studying the drug loading capacity of different morphologies.

(5) Calculating drug release profile for the most promising nanoarchitecture using computational simulation.

Chapter 2: Literature Review

Chapter 2: Literature Review

2.1. Formation of Nano-tubular Anodic Oxide Layer on Ti and Ti-alloys

There has been an amplified interest recently in exploring nanoscale surface topography for implantable devices such as dental and orthopedic prosthetics, grafting materials and intravascular stents – as will be described below [57]. Titanium and titanium alloys possess superior properties relative to many other materials in terms of biocompatibility, corrosion resistance, specific densities as well as mechanical properties that are tuned with alloy material and according to the intended application [57,58]. Consequently, nanotubular oxide structures formed on the surface of titanium and its alloys have been extensively investigated for enhancing the performance of biomedical implants, especially TiO_2 nanotubes [57- 66].

Different techniques have been used for the fabrication of these structures such as sol-gel, atomic layer deposition, hydro/solvothermal methods and micelle templates [59–66]. However, among these methods, one technique showed superior control on the dimensions and morphology of the nanostructure, which is electrochemical anodization in fluoride-containing electrolytes. It is also relatively simple, scalable, cost-effective and applicable for complex-shaped base material [67]. Early report of achieving self-organized TiO_2 nanostructure using anodization was by Zwilling, et al in 1999 who produced nanoporous assembly of TiO_2 on Ti-based alloy in acidic medium [68]. In 2001, Gong, et al first reported the formation of highly ordered TiO_2 nanotube array by anodizing titanium in dilute HF electolyte [69]. Efforts to optimize these nanotube arrays have been ongoing for more than a decade now to be used for a wide range of promising applications. It was found that anodization process, and accordingly the final surface nanomorphology and composition, are drastically affected by anodization conditions, such as, applied potential, time, pH and fluoride species concentration [67]. Some of these efforts are summarized in Table 2.1 below.

Since the work of Grimes, et al in 2001, the development of TiO_2 is grouped into three generations reference to the nature of the electrolyte used. First generation TiO_2 nanotubes were

achieved by aqueous HF based electrolytes, see Figure 1.2. They are characterized by relatively short length with maximum of 500 nm [69,70].

Table 2.1: Summary of titania nanotubes properties under different anodization conditions [71].

Length /µm	Wall Thickness/ nm	Diameter /nm	Voltage/ V	Time/ h	Main solvent	Conditions	Ref.
0.12	9	22	10	6	H_2O	0.5% HF + acetic acid (7 : 1)	72
1.76		65	20	10	EG*	0.2M NH_4F+0.1M $H3PO_4$+2% H_2O	73
0.36	17	46	12		H_2O	0.5% HF + acetic acid (7 : 1)	74
0.50	<10	150	5–15	4	Glycerol	0.5 wt% NH_4F	75
3.5			60		EG	0.25 wt% NH_4F	
18			20–60		EG	0.25 wt% NH_4F	
0.5	15	100	20	2	H_2O	0.5 wt% NH_4F	76
1.9–5.7	8	30	20	16–70	GL	0.5 wt% NH_4F	77
6	20	110			H_2O	0.1 M KF + 1 M $NaHSO_4$ 0.2 M trisodium citrate sodium hydroxide	78
10	<20	15-110	20-50	1	EG	0.25 wt% NH_4F 10 wt% H_2O	79
15			50	12	EG	0.25 wt% NH_4F	80
7-35	15	130	60		EG	0.25 wt% NH_4F 2 vol.% H_2O	81
134	25	160	60	17	EG	0.25 wt% NH_4F	82
45	15	120	40	69	DMSO**	2% HF	
93	-	200	60	70	DMSO	2% HF	
220	50	110	50	17	Formamide	NH_4For HF, 2% H_2O	83
360	20	120	60	96	EG	0.3 wt% NH_4F, 2% H_2O	84
380				168		0.3 wt% NH_4F	
538				168		0.4 wt% NH_4F, 2.5% H_2O	
1000				216		0.3 wt% NH_4F, 3.5% H_2O	

*EG: Ethylene Glycol

** DMSO: Dimethyl Sulfoxide

For the second generation, nanotube length was increased up to 7µm. This was achieved by controlling the electrolyte pH and accordingly the chemical dissolution of TiO_2 during the process of anodization. In 2004, Grimes, et al used electrolyte solution containing sodium fluoride (NaF) or potassium fluoride (KF) to produce nanotube arrays that would belong to the second generation. They adjusted the pH to 4.5 using sulfuric acid, sodium hydrogen sulfate, sodium hydroxide and/or citric acid. They were able to produce nanotubes up to 4.4 µm, see Figure 2.1 [85]. One year later, Grimes, et al were able to again produce longer nanotubes – relative to first generation – using different electrolytes and conditions. They used 1:1 flourinated dimethyl sulfoxide (DMSO) and ethanol to produce nanotube arrays of 2.3 µm [86].

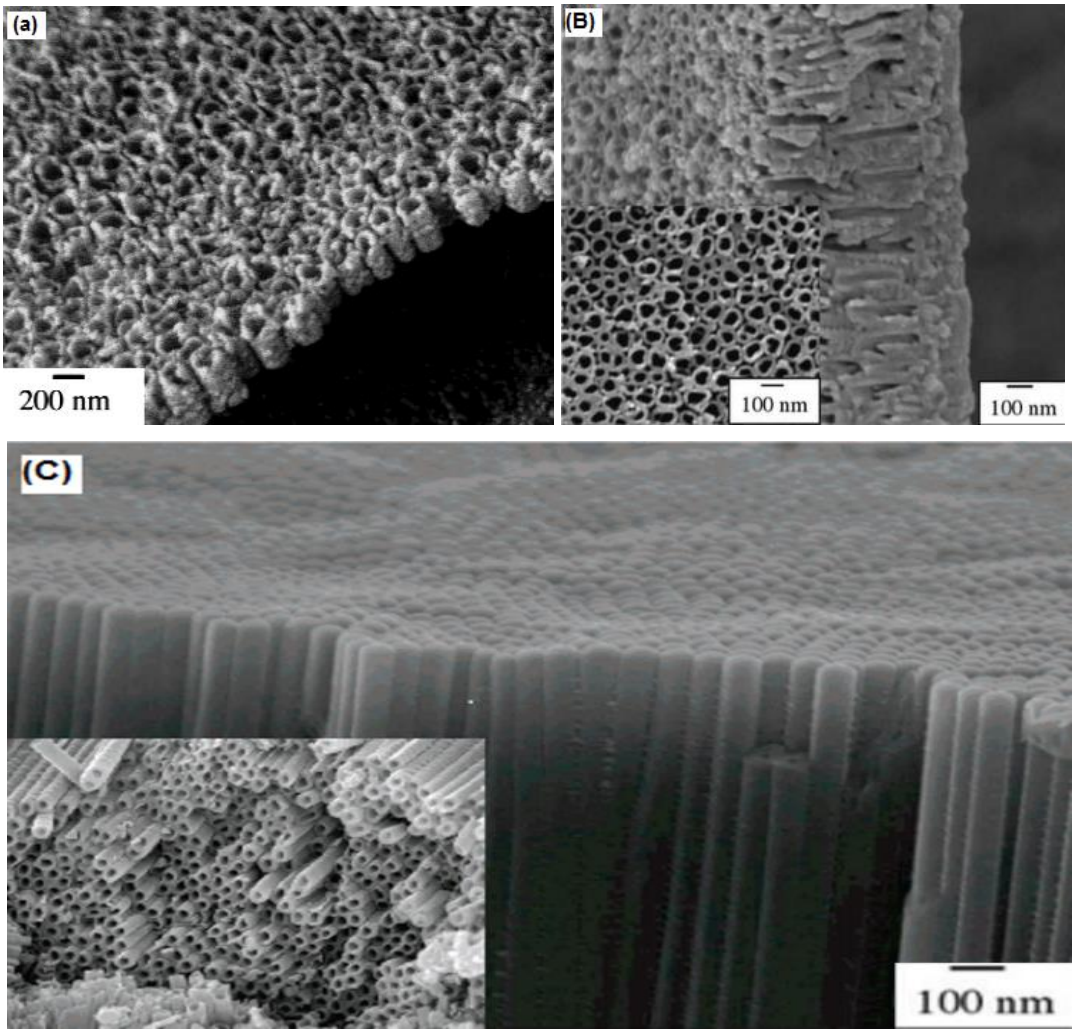

Figure 2.1: SEM images for TiO_2 nanotubes arrays for (a) first generation [69], (b) second generation [85], (c) third generation [82]

Third generation of TiO_2 nanotubes array was achieved in later work by processing in non-aqueous, polar organic electrolytes such as ethylene glycol and formamide, reaching tubular length of up to 1000 µm. In 2006, Grimes, et al succeeded to produce nanotube array up to 134 µm in length, see Figure 2.1. They used a variety of polar organic electrolytes as mentioned earlier, along with fluoride ion donor as KF, NaF or HF. They reported that the key to successful fabrication of long arrays is in keeping water content below 5% [82]. This was followed by several successful attempts to produce arrays of length above 100 µm. In 2007, they reported for the first time self-aligned nanotube arrays of titania about 1000 µm in length and 10 000 aspect ratio, using NH_4F and ethylene glycol-based electrolytes [84], see Figure 2.2. Finally, fourth generation is suggested to be one with fluoride-free electrolyte chemistries [87].

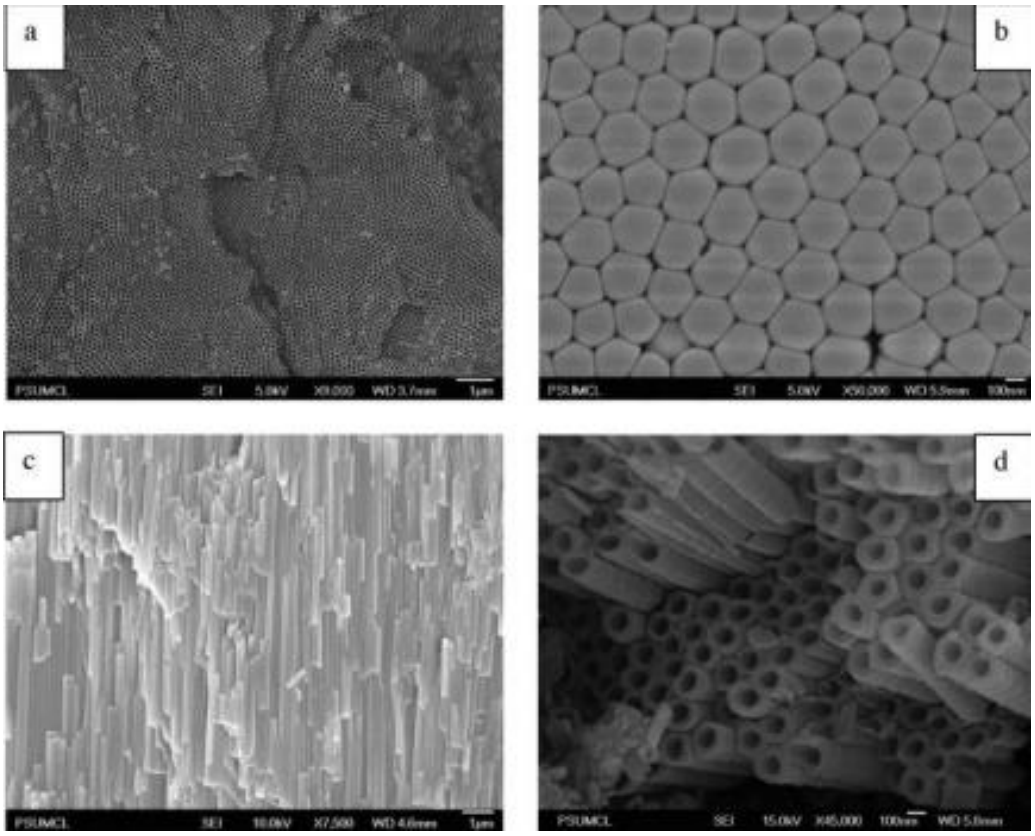

Figure 2.2: SEM images of the first reported nanotube arrays of length 1000 µm (third generation) using organic electrolyte. (a) top view, (b) bottom/barrier view, (c), (d) cross-sectional view [84].

In addition to morphological characteristics of the titania nanotubes arrays, their properties depend on the crystallinity and isomorph type. This directly affects its utility for different applications, including efficiency at biological interfaces in biomedical applications. As-fabricated nanotubes are amorphous. Upon annealing in oxygen at elevated temperatures, tube walls are converted into anatase and rutile phases, respectively. As the anodization voltage increased, amount of anatase formation becomes higher [88–92]. The rutile phase initially starts at the interface between the nanotube arrays and the support. At elevated temperatures (above 550 ^{o}C), rutile crystallites merges with the nanotubes and transforms into compact rutile layer as temperature reaches 800 ^{o}C [93].

In-application efficiency also relies on the integrity of the titania nanotubes layer at the functioning site. Unfortunately, weak adhesion has been reported between the nanotubes layer and the metallic substrate, leaving them prone to be peeled of easily [94], [95]. Therefore, several attempts have been conducted to understand the main cause of such phenomenon and offering practical solution to it. Schmidt-Stein, et al thermally treated TiO_2 in acetylene atmosphere to transfer it to its semi-metallic form (TiO_xC_y). They explained that incorporating carbon to its microstructure enhanced the layer's mechanical strength [96]. Xiong, et al annealed TiO_2 nanotubes for different time durations and reported that adherence improved actually with annealing time [97]. Recently in 2014, Yu, et al introduced 200 nm thick oxide layer near the nanotube bottom by adding fluoride-free anodization step prior to the main anodization process, see Figure 2.3. They introduced this approach to reduce the fluoride rich TiO_2 layer found at the interface with metallic substrate that is believed to be responsible for poor layer adhesion. They reported that this approach, increased adhesion strength almost three folds [98].

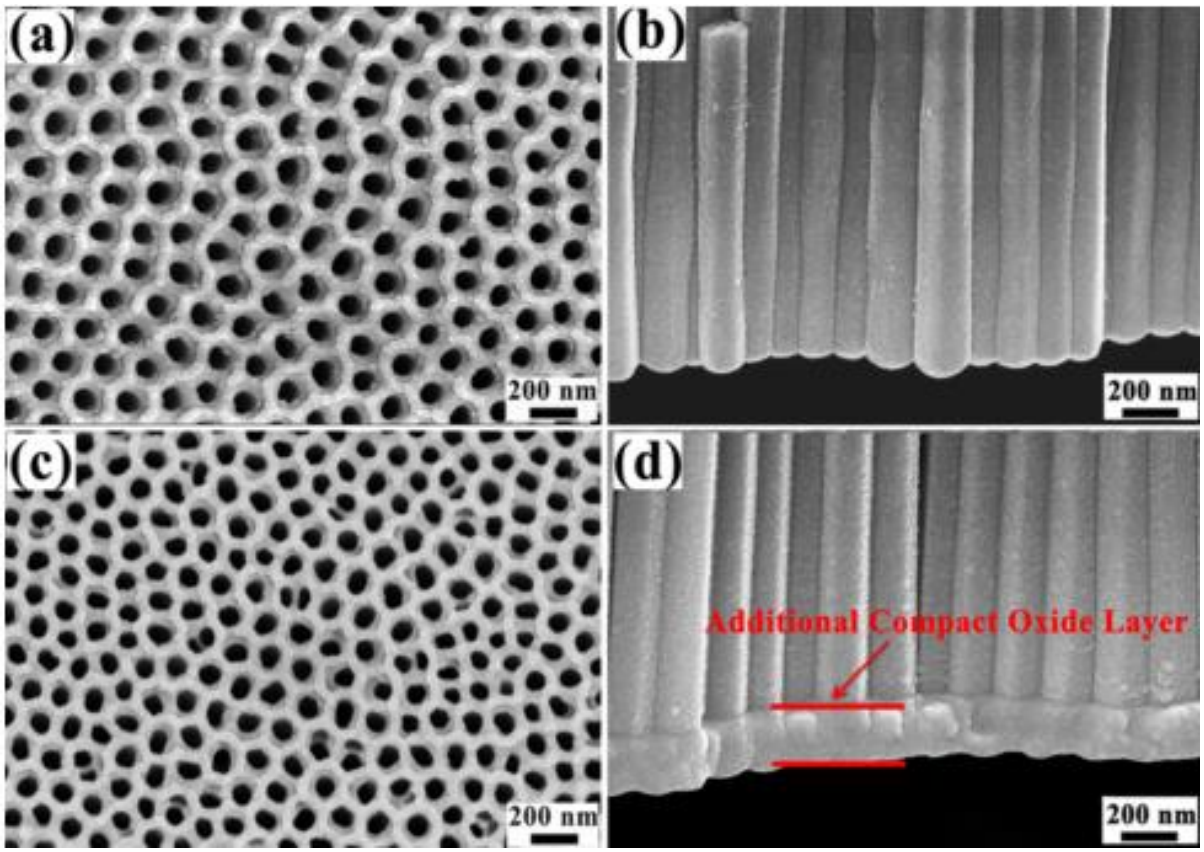

Figure 2.3: SEM images of top view on the left and side view on the right of titania nanotube arrays (c,d) with and (a,b) without additional oxide layer by fluoride free anodization [98].

The same principle of using electrochemical anodization technique was extended to titanium alloys for producing oxide layer of nano-scaled topographies [67]. In fluoride-containing electrolytes, fabrication of nanostructured oxide layer for titanium alloys using anodization technique was tailored for wide range of alloys with endless virtual possibilities, to be used in different applications; some of which are summarized in Table 2.2 below.

Table 2.2: Summary of TiO_2 nanotubes' properties made from alloys under different anodization conditions [71].

Alloy	Length / μm	Diameter/nm	Vol/V	Time/ min	Main solvent	Conditions	Ref.
Ti45Nb (45 wt% Nb)	2.9 6.3	60	20	120 20h	water	1 M NaH_2PO_4, 0.5 wt% HF	[99]
TiMo (7 wt% Mo)	4-16	15-45	20-60		EG	0.05 M HF	[100]
Ti–0.2 wt% V Ti–3 wt% V Ti–18 wt% V	1	120-130	60	15-20	EG	0.2 M HF	[101]
TiNb (0.1 wt% Nb)	1-15	50-65	50	5-120	EG	0.1 M NH_4F+ 1 M H_2O	[102]
Ti–0.2 wt% W Ti–9 wt% W	1.1-1.2	85-95	120	10 12	EG	0.2 M HF	[103]
TiN	650	20-80	20	120	Glycerol + water	0.27 M NH_4F	[104]
Ti -45wt% Nb Ti- 35wt% Ta Ti- 50wt% Zr	50 50 30	20-50 30-90 10-15	40	<1	Cl-perchlorate	0.05 M $NaClO_4$ +0.05 M NaCl in 50:50 vol% of H_2O:C_2H_5OH	[105]

Generally, the composition of the oxide layer and the ratio of materials, directly reflect the properties of the alloy. This was demonstrated by Kamkin, et al for anodic oxide films on titanium-aluminum alloys. They showed that the mainly amorphous oxide film consists of TiO_2 and Al_2O_3 mixture with ratios perfectly consistent with the alloy matrix [106]. This phenomenon was likewise observed for TiTa alloy by Jha, et al. However, they also reported another behavior observed for other alloys, such as TiNb and TiZr. These alloys showed mixed oxides in the anodized layer along with oxides of individual components, as shown in Figure 2.4 [105]. On the other side, full conversion of the anodized surface into mixed oxide was reported by Yasuda, et al for TiZr alloy, as shown in Figure 2.5 [107].

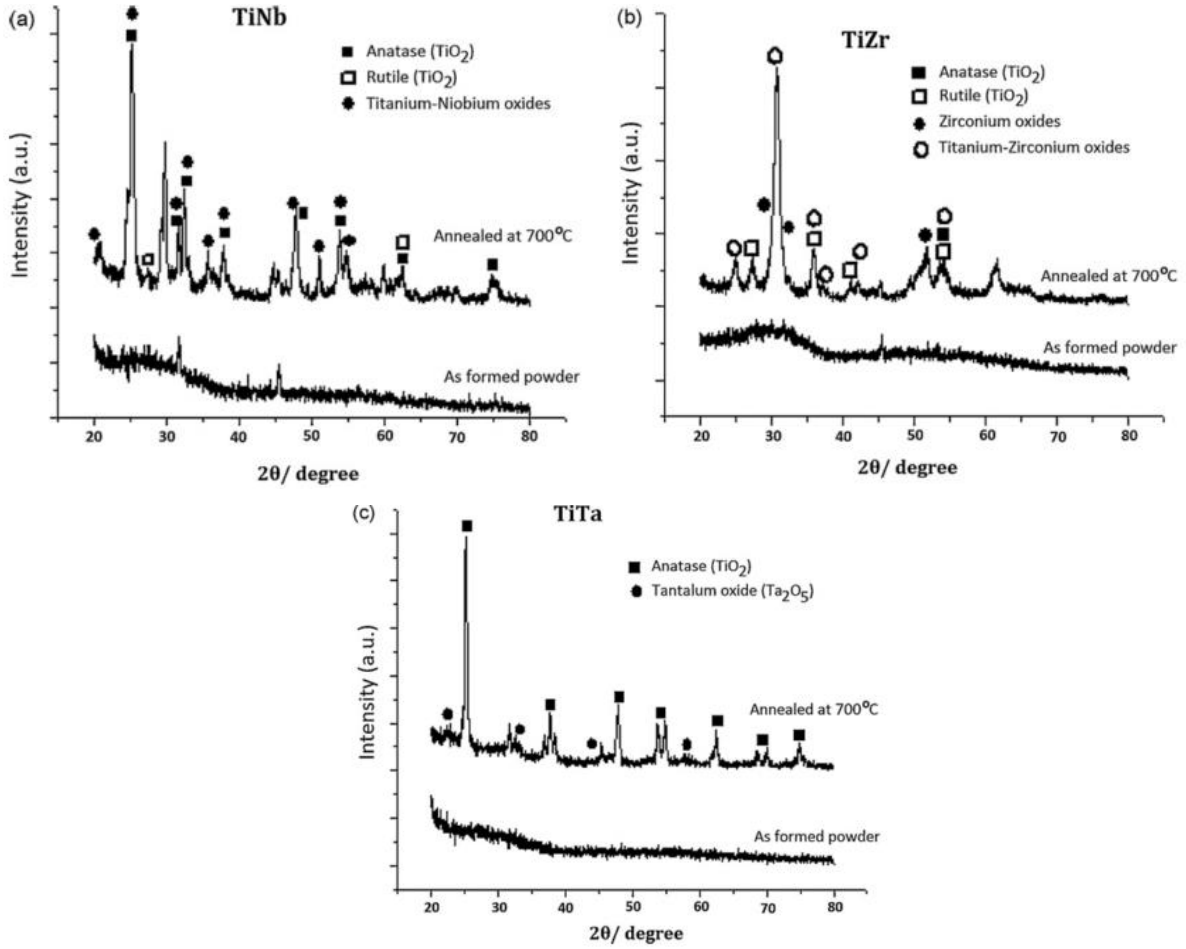

Figure 2.4: XRD spectra of oxide nanotubes for different titanium alloys, before and after annealing. Oxides from (a) TiNb alloy, (b) TiZr alloy, and (c) TiTa alloy [105].

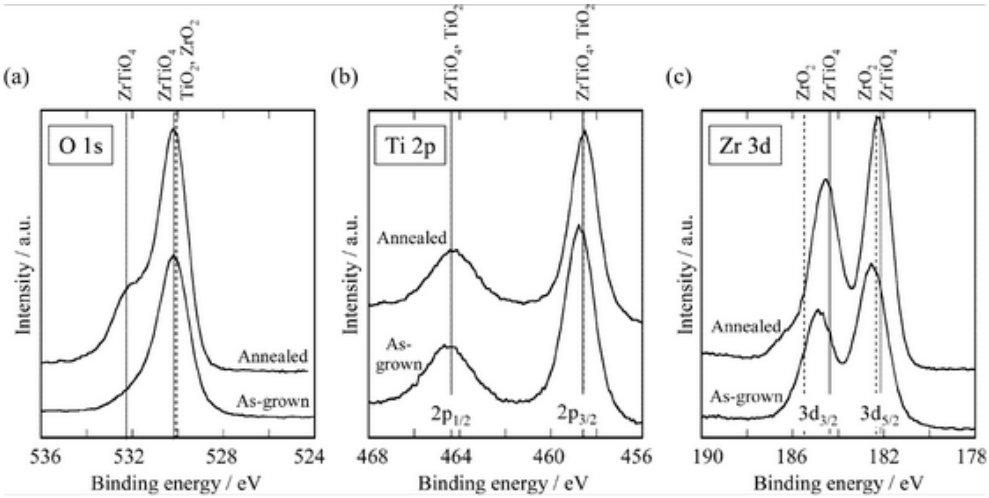

Figure 2.5: XPS spectra of (a) O 1s, (b) Ti 2pa (c) Zr 3d, for the as-grown and annealed nanotubes of TiZr alloy [107].

2.2. Biological Response of Nanotopography on Surface of Titanium and Titanium Alloy

The response of biomaterials entirely depends on biocompatibility and surface properties. Hence, beside the choice of substrate material, paying attention to surface treatment is crucial for all biomedical applications [108]. As mentioned earlier, nano-architectures have been extensity studied as surface treatment for biomaterials. They are considered as biomimetic interfaces that accordingly provide solutions to few biocompatibility challenges and enhance tissue regeneration [57]. Experimental evidences have recently been accumulated to show the importance of surface topography of biomaterials at the nanoscale and its effect on biological microenvironment [109].

For orthopedic implants, this has been studied for years now and positive effects of nanostructures on tissue adhesion and regeneration are well-established. This motivated the exploration of those structures for other applications in contact with human tissue or blood components such as intravascular stents. Minagar, et al reported that bone cells response to implant material is affected by topography, mechanics, physicochemical and electronics of implant surface [110]. Hence, as suggested by Webster, et al the bioactivity of the implants can be considerably improved using nanostructured oxide materials [111]. Hamlekhan, et al further elaborated that anodized nanotubular surfaces were found to promote osteoblast cell adhesion, hydroxyapatite growth, improved integration and proliferation. This is attributed to increased surface area offering more area for cell interaction, protein adsorption, surface energy as well as increased hydrophilicity [112].

Oh, et al studied MC3T3-E1 cell growth and proliferation on TiO_2 nanotubes array versus pure Ti. Cell growth on TiO_2 nanotubes substrates was found to be much faster. This was justified by the surface area presented by the nanotubes pores and in-between gaps that offered ions, proteins and nutrients continuous supply [113]. Effect of pore diameter on osseointegration was an area of investigation for many research groups. Wang, et al studied diameter effect on mechanism of biological attachment of implants to surrounding tissue. They used 30, 70 and 100 nm nanotubes structures with *in-vivo* implants and observed histological features of bone surrounding the implant. Best results were reported for 70 nm diameter nanotubes [114]. Kang, et al

also studied osseointegration over the same range of diameters. Highest values were also reported for 70 nm after 4 weeks. However, higher values with 30 nm nanotubes structure were observed after 12 weeks [115].

Almost 2 decades ago, Steele, et al have reported that protein adsorption is higher on hydrophilic surfaces than hydrophobic ones [116], which presents a critical step in cell adhesion and implant bioactivity. Giordano, et al demonstrated that TiO_2 nanotube formation on the substrate surface decreased water contact angle (WCA) [117]. Therefore, in order to enhance tissue integration, adhesion and proliferation efforts have been accordingly exerted to increase hydrophilicity of the implant surface. Terriza, et al induced superhydrophilicty on titania layer by light using UV illumination. They reported highly enhanced cell attachment on immediately illuminated titania surface [118]. Chang, et al studied titania nanotube contact angle at different anodization time (5, 20, 40, 60, 90 min and 24 hrs) at constant voltage (30 V) and at different annealing temperatures (no annealing, 300, 400, 500 ^{0}C). They reported that contact angle decreased with increasing anodization time, as shown in Figure 2.6, and increasing annealing temperature [119]. Also, it was reported by Uchida, et al that anatase phase of titania nanotubes after annealing is much more efficient for nucleation and growth of bone tissue. This is attributed to its ability to promote growth of hydroxyapatite layer [120].

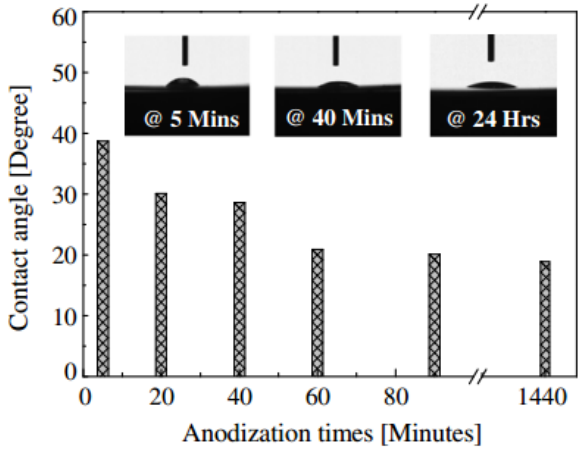

Figure 2.6: Contact angle of titania nanotubes surface versus anodization time [119].

Influence of nanoarchitecture on bioresponse for intravascular stent surfaces are not as thoroughly reviewed in literature as for orthopedic prosthesis. Yet, a significant number of research groups have investigated the effect of rough topographies on stent surfaces for almost two decades now, and attention has been paid lately to nano-scale treatment. Back in 1997, De Scheerded, et al suggested that stents with electropolished smooth surfaces are less thrombogenic than non-polished ones. This was demonstrated on a rat AV (atrioventricular) model and a porcine coronary model using an electropolished sample versus untreated one. Total weight of the formed clot was found to be much lower with electrochemically polished sample [121]. Tepe, et al used an *in-vitro* model with human fresh whole blood to study hemoresponse of electropolished stent surface reaching the same conclusion. It was found that platelet activation and thrombogenicity was reduced on such treated samples versus smoother ones [122]. These reports can significantly discourage the use of rough surface in stent applications, despite its promising potential for offering polymer-free drug loaded surfaces.

However, on the other side, Palmaz, et al were able to demonstrate faster endothelialization on stent surface decorated with parallel grooves at the microscopic scale than smooth counterpart. This was studied using *in-vitro* culture of endothelial cells [123]. They, furthermore, confirmed their results using *in-vivo* studies through placing sample stents in porcine carotid arteries [124]. They explained stating that microscopic grooves assisted endothelial cell (EC) migration to stent surface, which was found to be more influencing in endothelialization than EC proliferation [125]. This fast endothelialization on rough topographies was found to significantly reduce rates of thrombosis as well as neointimal hyperplasia. However, delayed endothelialization with their smooth counterpart has been linked with late intravascular complications [26,126–130]. These findings strongly supported studies that were extensively undertaken on stent rough surface treatment for enhancing drug eluting stents.

These efforts were initially invested in studying the biological interaction of microporous surface architectures fabricated by different techniques. Doi, et al demonstrated positive influence of microporous polyurethane surface treatment on endothelial tissue response using *in-vitro* analysis [131]. Also, Nakayama, et al supported this data by *in-vivo* studies. They covered the stent surface with microporous elastomeric film – fabricated by laser ablation – with

immobilized FK506 for prevention of neointimal hyperplasia. After one month implantation in rabbits, no significant lumen loss or hyperplasia was observed [132]. Dibra, et al performed an *in-vivo* evaluation as well but on human sample, they conducted a randomized double blind study to investigate the influence of stent surface topography on patient outcome after stent implantation. They used 316L SS stent roughened with sand blasting into 0.09 and 0.21 μm minimum and maximum root mean square roughness reference to a smooth surfaced stent. Data reported from this study encouraged the use of rough surface treatment not only due to ability to significantly reduce late lumen loss versus smooth reference, but also due to its potential to be used for storage of anti-restenotic drugs [133]. Transferring micro-scale stent surface treatment into the market, Yukon™ stent was released by Translumina, Hechingen, Germany. Post marketing clinical data demonstrated comparable performance with other well-established stent (Taxus), while failed to prove non-inferiority with another (Cypher). Therefore, long term efficacy and safety of Yukon stent is still under question and investigation.

For higher pores density, larger surface area, more controlled drug release profile and better biomimicry, nanoporous surfaces on stent materials became highly attractive for investigation [134]. Wieneke, et al coated a 316L SS stent with aluminum thin layer then electrochemically converted it into nanoporous structure with pore diameter from 5 to 15 nm. They investigated the effect of this architecture loaded with tacrolimus drug on the biological response of surrounding tissue. They reported that the coating as well as loaded drug resulted in a positive synergistic effect reducing the local inflammatory response and intimal hyperplasia, as seen in Figure 2.7 [135]. This led to the release of Jomed™ stent into the market of intervention cardiology [136]. However, Kollum, et al carried out in-depth investigation to assess the effect of this nanoporous aluminum coating on in-stent restenosis, using porcine restenosis model. Particle debris was found to be shed from the coating into the media and the intima, resulting in augmented inflammatory response. This can potentially counteracts the effect of the antiproliferative loaded drug resulting in neointimal hyperplasia and late lumen loss, see Figure 2.8 [137].

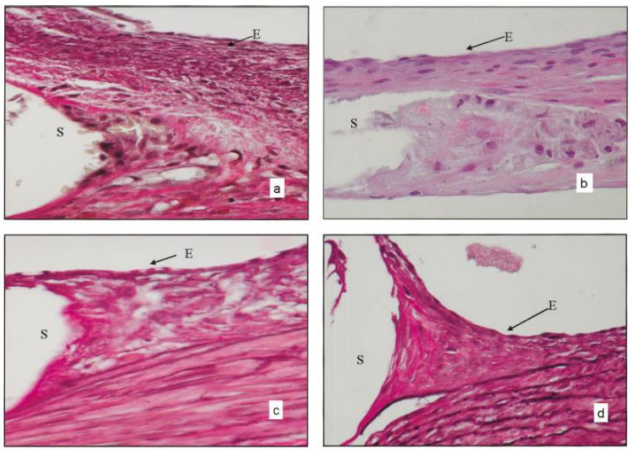

Figure 2.7: Inflammatory cells migration to stent strut. A) Bare metal stents. B): with Al_2O_3 coating. C): with Al_2O_3 coating loaded with tacrolimus 60 µg. D): with Al_2O_3 coating loaded with tacrolimus 120 µg [135]

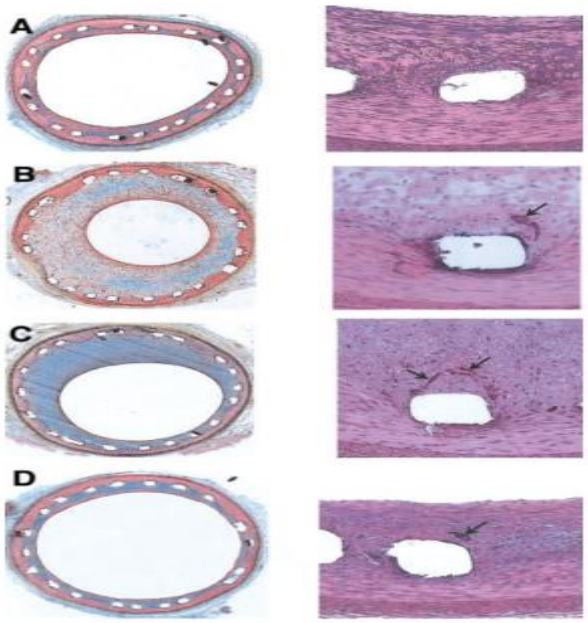

Figure 2.8: Cross sectional histomorphometric images of porcine arteries 4 weeks after implanting A) bare stents, B) aluminum oxide ceramic-coated stents, C) aluminum oxide ceramic-coated stent eluting FK506 (50 µg) D) aluminum oxide ceramic-coated stent eluting FK506 (180 µg) . Presenting: A) thin neointima; well healed. B) Thick neointima with fragments of ceramic stent coating present (arrow, right). C) moderately thick neointima; well healed with fragments of ceramic stent coating (arrow, right). D) neointima; well healed and similar in area to bare metal stent with fragment of ceramic stent coating (arrow, right) [137].

On the other hand, the use of TiO_2 nanotube arrays for stent surface treatment showed highly promising biological response that has driven its thorough investigation for the last few years. Jin, et al have reported in 2008 an enhanced endothelial cells migration, faster proliferation and increased reliability in the presence of TiO_2 nanotubes. They underwent *in-vitro* analysis using bovine aortic endothelial cells (BAEC) to compare between flat Ti surface versus nanostructured oxide counterpart. They observed enhanced focal cells adhesion, contact stimulation and an upregulated antithrombotic state with the nanoarchitectured surface, see Figure 2.9 [138].

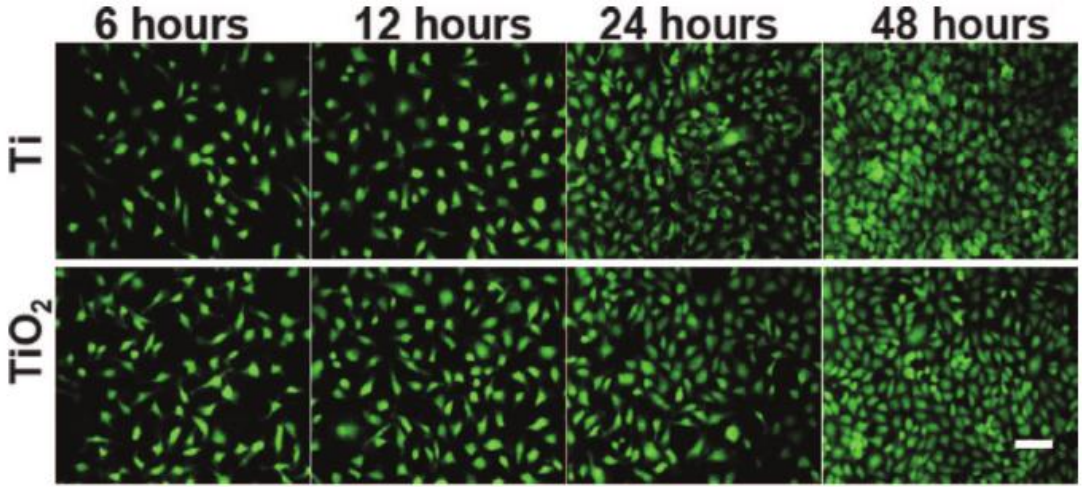

Figure 2.9: BAECs viability on flat Ti (upper panel) versus TiO_2 nanotubes (lower panel) after different time intervals (6, 12, 24, 48 hours). Cell survived over the two substrated, however, it showed more flat monolayer of cells on nanotubes at 48 hours versus aggregated and relatively disrupted ones on flat Ti at the same time [138].

In 2009, Mark, et al used another *in-vitro* model to study the impact of TiO_2 nanotubes on biological response of stent materials. The model involved studying the cellular activity of mesenchymal stem cells (MSC) on the nanoarchitectures. They examined the influence of not only surface geometry, but also surface chemistry and crystallinity. Their data reported significant dominance of effect of geometry over other parameters on biological response. Data supported better cells migration, adhesion and proliferation on TiO_2 nanotubes versus smooth surface. Furthermore, they observed enhanced MSC differentiation on nanotubes with smaller diameter (15nm) as compared to larger diameters (about 100nm), see Figure 2.10 [109].

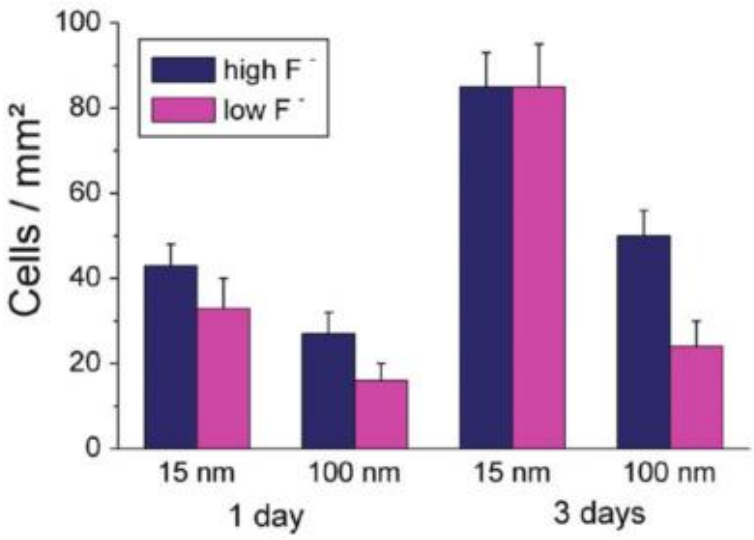

Figure 2.10: MSC adhesion to 15 and 100 nm TiO_2 at high and low F^- content at 2 time intervals [109].

These findings were supported by Desai, et al by immunofluorescence staining, SEM imaging, proliferation assay, and immunoassay using endothelial cells (EC) and vascular smooth muscle cells (VSMC) cultures. Results suggested that nanotopography may influence EC and VSMC in a manner useful for vascular stents applications. As shown in Figure 2.11, TiO_2 nanotubes promote EC proliferation, which would result in faster healing, while does not support VSMC proliferation, which would result in lower risk of neointimal hyperplasia [139]. One year later they further reinforced these data using gene expression analysis. Microarrays indicated positive effect on EC proliferation and favored negative effect on VSMC proliferation, and expression of inflammatory precursors and well as coagulation involved molecules [140].

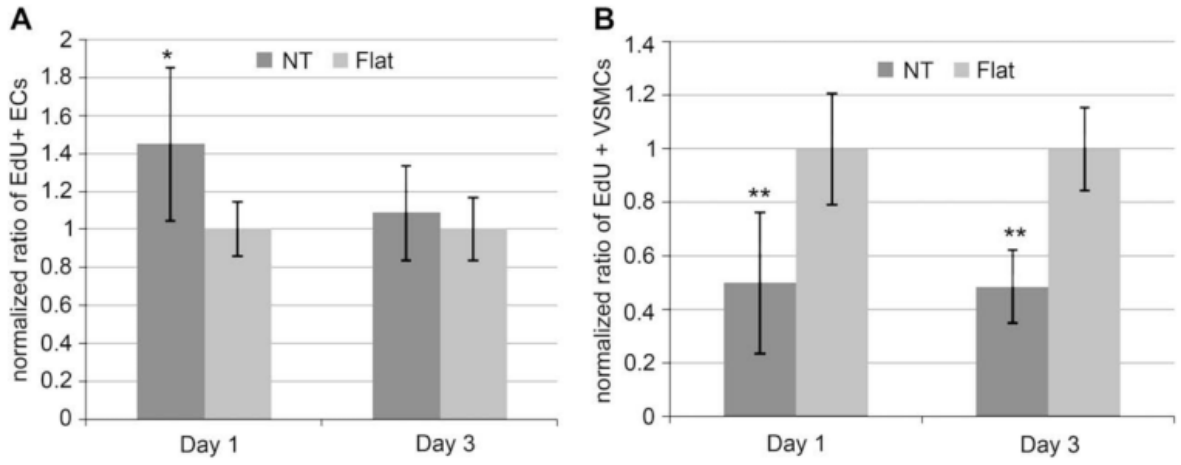

Figure 2.11: Ratio of 5-ethynyl-20-deoxy- uridine (EdU) positive, which is incorporated to detect cell proliferation according to the assay protocol. (A) ECs, (B) VSMC on nanotubes versus smooth muscles, normalized by the average proportion of positive cells on flat surfaces on day 1 and 3. Data is presented as average + or - standard deviation. *p<0.05, **p<0.01 versus same day flat control, n=6 [139].

As blood contacting biomaterials, hemocompatibility is an essential property to be investigated for TiO_2 nanotubes as part of evaluating its biological response. Smith, et al have investigated the adhesion and activation of platelets, clotting kinetics of whole blood and key blood serum proteins adsorption on titania nanotubes arrays. Their initial results reported high protein adhesion, platelets activation and whole blood clotting kinetics. However, they highlighted that hemoresponse is highly affected by surface geometry and can be altered and adjusted by controlling tubes size parameters, which required further proper investigation in this area [57]. On the other hand, Menon, et al suggested that enhanced proliferation of endothelial cells on grown TiO_2 nanotubes would consequently contribute to hemocompatibility through regulating platelet activation and accordingly reducing the risk of thrombosis. This was elaborated by highlighting that one of the main roles of endothelial cells is to secrete anti-thrombogenic products such as nitric oxide (NO) and prostaglandin I_2 (PGI_2), which help maintaining vascular homeostasis [141].

2.3. Nanoarchitectures as drug reservoirs

As mentioned previously, the great interest of using nanoscale topographies on the surface of biomaterials is not only driven by their ability to enhance biological response, but also by their high potential to be used as drug reservoirs for local drug delivery. Choice of the drug active ingredient is directly related to the application and site of biomaterial implantation. For example local delivery of antibiotics is applied for orthopedic implants to ensure environment sterility and ensure proper healing. On the other side, for intravascular stents, for example, cytotoxic drugs are mostly delivered locally to avoid neointimal hyperplasia and preserve blood flow. Local drug delivery does not only target the dosage to the site of application but also avoid higher risks of side effects associated with systematic drug intake [142,143]. Nanoarchitectures as local drug delivery systems can offer a number of advantages over few of currently followed techniques; 1) It can be grown on material whose biocompatibility has been well-established and already widely used for biomaterials such as titanium and titanium-based alloys, 2) synthesis techniques can provide a control over the surface structure's size and morphology, offering potential control over release kinetics, 3) nanoarchitectures can be fabricated on 3 dimensional (3D), non-planar surfaces, hence being adaptable to a variety of implant technologies, 4) and surface wettability can be easily controlled [143].

For intravascular stents, local drug delivery using nanoarchitectural reservoirs was first investigated by Wieneke et al in 2003. They used nanoporous anodic aluminum oxide (AAO) to release tacrolimus for studying rabbit intimal proliferation [135]. Positive results have driven the interest of Kim et al in 2007 to further investigate the drug release kinetics from such structures. 316 SS stents were coated with nanoporous anodic aluminum oxide (AAO) fabricated via anodization, which have different tubes dimensions (diameter and length). 2-deoxyadenosine drug was loaded to the (AAO) coated sheets by immersion in drug solution for certain amount of time. *In-vitro* drug release was investigated in phosphate buffer saline (PBS) using high performance liquid chromatography (HPLC). It was observed that drug release is directly proportional with nanotubes pore diameter, while inversely proportional with their depth, see Table 2.3 [144]. In another study, Kim et al used lipophilic paclitaxel drug loaded in the same AAO platform to study its release kinetics, versus the hydrophilic 2-deoxyadenosine. Paclitaxel release

from different nanotube diameters and depths showed that amount of drug released did not depend on pore diameter but varied inversely with depth, see Figure 2.12 [145].

Table 2.3: Amount of drug release/µg from AAO film [144].

Time (hour)	Diameter (nm)				
	26.46	13.5	19.7	13	27.2
	Depth (µm)				
	1.33	0.943	1.4	3.2	4.4
2	500.97548	397.58979	197.72221	573.01701	304.32572
5	3.15701	3.00	0.93224	2.81911	2.39437
11	0.75078	0.4815	2.17619	0.3778	0.37863
23	0.9379	0.40268	0.93244	0	0
47	1.08203 0 0	0	0.49764	0	0
95	0	0	0	0	0
143	0	0	0	0	0

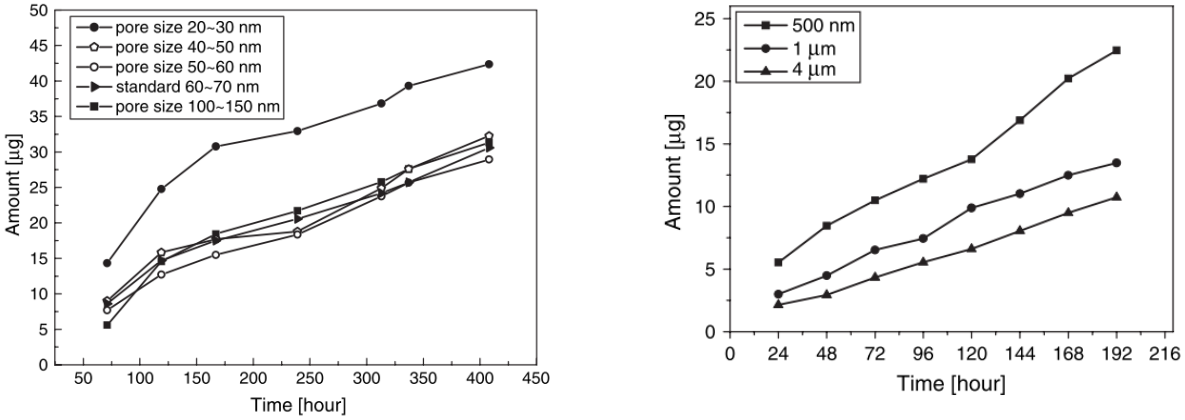

Figure 2.12: Cumulative release of paclitaxel from AAO with different pore diameter (to the left) and depths (to the right) [145].

However, data on biological studies of nanoporous alumina versus titania nanotubes described earlier could possibly indicate better *in-vivo* response with titania nanoarchitectures [146]. This encouraged their in depth investigation as drug reservoirs for a number of applications including intravascular stents, some of which are summarized in Table 2.4 below. This was early studied by Ayon et al using nanoporous TiO_2 to load dexamethasone drug with target value

comparable to dexamethasone-eluting BiodivYsio^{TM} stent. They reported that with fabricated structural dimensions, one step loading resulted in unfavourable value of loaded drug with 70 ng/mm^2 versus target of 500 ng/mm^2. However, subsequent and sequential drug loading procedure would increase total loaded amount and potentially reach desired target, as seen in Figure 2.13 below [147].

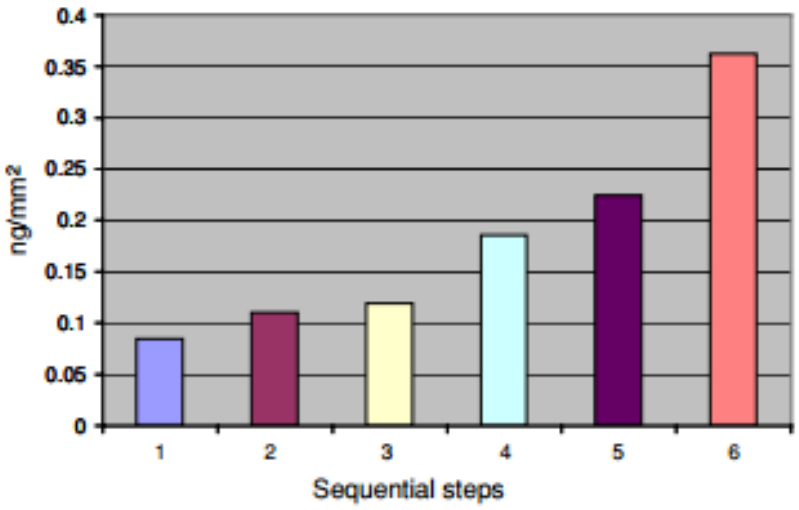

Figure 2.13: Amount of loaded dexamethasone per sequential loading, using HPLC [147].

Popat, et al investigated the use of TiO_2 nanotubes as another nanoarchitecture that can act as drug reservoir. Through fabrication strategies, they offered better control over drug loading capacity and release kinetics through controlling nanotubes dimensions. In one study, they fabricated TiO_2 nanotube arrays of 80 nm pore diameter and 400 nm in length for loading Gentamicin antibiotic to avoid bacterial infection at site of bone implants. They reported that 70-85% of the drug was retained in the nanotubes after washing. For drug release they reported that total time needed for all drug to be eluted from the array is directly proportional to the initial loaded amounts, with total time of 45, 90, 150 minutes taken to release 200, 400, 600 µg gentamicin respectively [148]. In another study, Popat, et al studied the drug release rate by varying the loaded amount and the drug molecules polarity. They used two different loaded biomolecules; 1) Bovine serum albumin (BSA) with molecular weight 67 kDa and net charge -18 at pH 7, 2) and Lysozymes (LYS), with molecular weight 14 kDa and net charge +7 at pH 7 [143]. They used three different initial loaded amounts of BSA and LYS; 200, 400, 600 µg, and

expressed the loading efficiency as percentage of the loaded protein after washing. The results showed that 60-80% of protein is loaded in the nanotubes regardless of the initial loading, see Figure 2.14. Their release profile demonstrated that release kinetics can be also controlled by varying nanotubes diameter and length [143].

Table 2.4, summarizes some of the ongoing efforts that are being exerted to study drug loading and release kinetics for TiO_2 nanoarchitectural reservoirs. Studies included are reporting a wide range of therapeutics for different biomedical applications, such as anti-inflammatory, antibacterial, anticancer and immunosuppressants. Factors, which affect drug delivery functionality, including nanotubes morphology, dimensions (diameter and length), surface chemistry, loaded drug properties, hydrophilicity …etc are described.

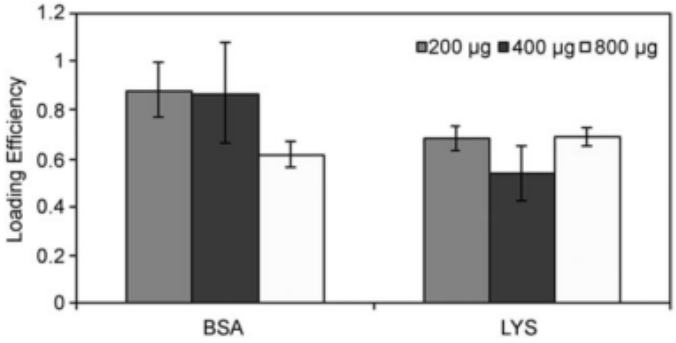

Figure 2.14: Loading efficiency of BSA and LYS at different initial loaded amounts [143].

Table 2.4: Summary of using TiO_2 nanotubes for delivering selected therapeutics [146].

Main Target	Therapeutic loaded	Additional features	Ref
Antibacterial	Vancomycin	*In-vivo* studies	149
	Penicillin/streptomycin	Loaded using simulated body fluid	150
	Gentamicin	Osseointegrating	148
	Cefuroxime		151
	Silver nanoparticles	Osseointegrating/*in-vivo* studies	152
	Zinc ions	Osseointegrating & anti-inflammation	153

	Antimicrobial peptide hhc-36	Also targets antibiotic-resistant bacteria	154
	Enrofloxacin		155
Anti-inflammatory	Ibuprofen	Osseointegrating/mechanical stability studies	156
	Indometacin		157
	Indometacin loaded and chitosan/poly(lactic-co-glycolic acid) coated	Antibacterial and osseointegrating	157
	Naproxen		
	Dexamethasone	Loading using simulated body fluid/osseointegrating	158
Antifungal	Itraconazole		159 160
Osseointegrating	Gelatin stabilized gold- NPs		
	Bone morphogenetic- protein-2 (BMP2)		161
	Pamidronic acids	Treatment of osteoporosis and Paget's disease	162
	Pre-synthesized- hydroxyapatite		163
	Strontium		164
	Bisphosphonates (BPs)	Study on Ti-6Al-4V alloy surface/ *In-vivo* investigations	165
	C-terminal (connective- tissue growth factor)- fragment		166
	Doxorubicin		167
Anticancer	Selenium	Antibacterial and osseointegrating	168
	Paclitaxel		169
	Cisplatin	Osseointegrating	170

Immunosupressant	Sirolimus	Study on vascular smooth muscle cells	[171]
Neurotransmitters	Dopamine	Implantable drug delivery system for brain conditions	[172]

Furthermore, many techniques were investigated to enhance drug loading and release rates from TiO_2 nanotubes. These are diagrammatically represented in Figure 2.15 and included for example, (A) precise control over length and diameter, (B) surface chemistry, (C) using plasma polymerization for tuning pore opening, (D) applying degradable polymeric coating on pore surface, (E-F) loading with drug nanocarriers that may be used for multiple drug delivery as well, (G-I) triggering drug release using external field, such as, magnetic field, temperature, radiofrequency and ultrasound [146].

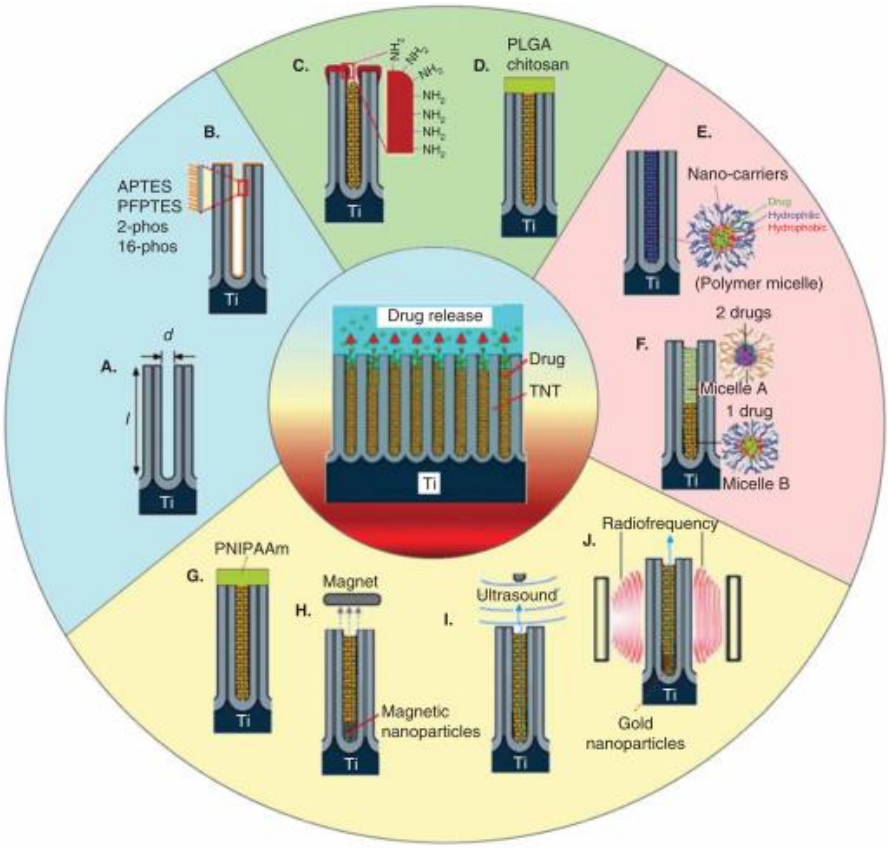

Figure 2.15: Strategies for enhancing drug release from TiO_2 nanotubes (visualized using one nanotube) [146].

Chapter 3: Materials and Methods

Chapter 3: Materials and Methods

3.1. Materials and Supplies

Titanium metal foils with thickness 0.25 mm and purity 99.95% were purchased from Alfa Aesar, USA. Ti-45Nb alloy sheets with 45 wt% Nb and thickness of 2.5 mm were purchased from Allegheny Technologies, Japan. Ti-17Nb-6Ta of thickness 0.3 mm were received as prepared by Department of Materials Science and Engineering, Egypt-Japan University of Science and Technology (E-JUST), Egypt, which was prepared by arch-heating in argon gas (high purity) atmosphere. It was then homogenized at 1000 ^{o} C for 7.2 ks in same atmosphere. Subsequently, samples underwent cold-rolling by 90% thickness reduction (CR).

Ammonium fluoride (ACS reagent, ≥ 98.0%), Formamide (purum, ≥ 98.0% (T)) and Glycerol (ACS reagent, ≥ 99.5%) were purchased from Sigma Aldrich, USA. Ethylene Glycol (Pure P.A.) was purchased from Lab-Scan analytical sciences, Poland, while Ammonium Sulphate (Ex-Pure) was purchased from Oxford Laboratory, India. Hydrochloric acid (35-38%) was purchased from Alpha Chemika, India. Sulphuric acid (98%), phosphoric acid (98%) and perchloric acid (70% AR) were purchased from S D Fine-Chem Limited, India.

2'- Deoxyadenosine drug (99%) and phosphate-buffered saline (PBS, 1X), sterile liquid were purchased from Alfa Aesar, Germany.

3.2. Potentiostatic Anodization

Anodization technique was used to fabricate arrays of Titanium and Titanium alloy nanoarchitecture. Prior to the anodization process, Ti and Ti-alloys sheets were cleaned ultrasonically in acetone then ethanol then distilled water. Platinum foil was washed in dilute HCl then distilled water. The anodization electrochemical setup is built up from counter electrode (platinum foil or graphite rod was used) and a working electrode of the substrate material of interest (cleaned Ti and Ti- alloy sheets). Electrodes were immersed in different

fluoride containing electrolytes in room temperature. Mixtures of different aqueous and organic electrolytes that were used are summarized in Table 3.1 below.

Table 3.1: Summary of the anodization process conditions used for different substrates and/or to obtain different morphology of nanoarchitectures

Electrolyte Code*	Electrolyte composition	Voltage/V	Time/hour
PD1	0.2 M NH_4F and 0.1 M H_3PO_4 , then complete to final volume of 50 ml with distilled Water	20	1.5
FP2	0.2 M NH_4F + 3 vol % H_2O + 0.1 M H_3PO_4, then complete to final volume of 50 ml with formamide	30	1.5
FG3	0.35 M NH_4F + 5 vol % H_2O + 20 vol% formamide, then complete to final volume of 50 ml with glycerol	50	3
			2
AD4	0.11 M NH_4F + 1 M $(NH_4)_2SO_4$, then complete to final volume of 50 ml with distilled water	40	2

*Electrolyte code: (Two main electrolyte components plus a serial numerical value)

Constant voltage between the counter and the working electrodes was applied using E3641A key sight DC power supply for predetermined amount of time. Voltage and time differed with the electrolyte used and are also summarized in Table 4.1. After anodization, samples from aqueous electrolytes were ultrasonicated in distilled water, while those from organic electrolytes were sonicated in acetone. Sample were afterward left to dry in air. Figure 3.1 demonstrates the setup used for this experiment and described above.

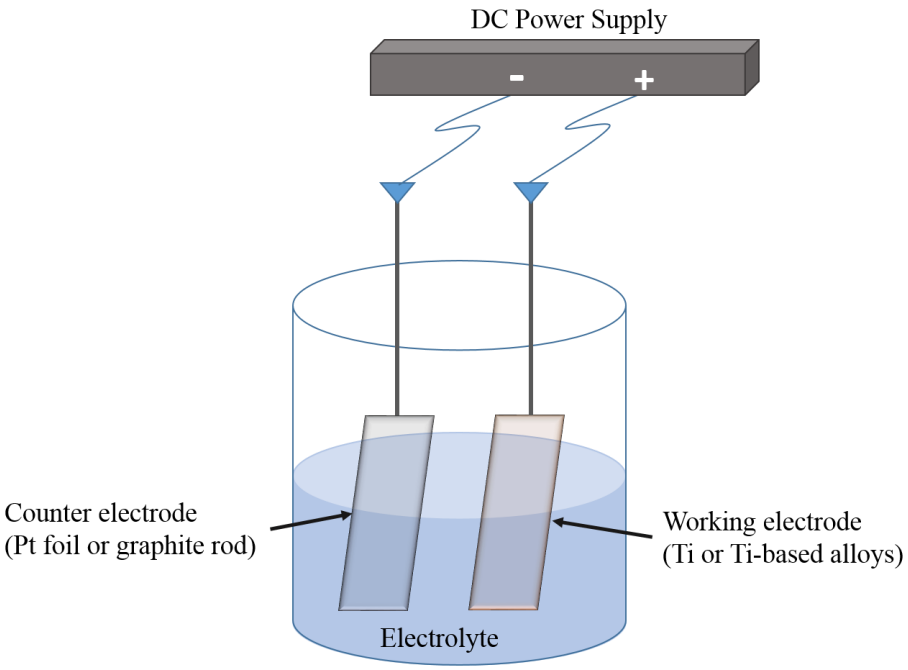

Figure 3.1: The two-electrode potentiostatic anodization setup.

3.3. Surface Polishing

In attempt to enhance nanoarchitecture morphology and avoid the effect of surface oxide layer on final structure, different surface polishing techniques were tried:

3.3.1. Mechanical Polishing

Mechanical polishing was done either manually or automatically. For manual polishing, samples were fixed manually on a smooth surface and gently rubbed with grinding paper (600 grit/inch^2). For automated mechanical polishing, samples were fixed on a metallic stage using heated wax. Samples were exposed to grinding wheel with 600, 800 and 1200 grit/inch^2 silicon carbide papers, respectively and then treated with alumina of 0.5 µm. After polishing, samples were detached from the metallic stopper by immersion in acetone under ultrasonication.

3.3.2. Electrochemical Polishing

System used for electrochemical etching is the same as described previously in potentiostatic anodization sector and demonstrated in Figure 4.1. However, the difference between the two setups would be in the used electrolyte solution, voltage and time. Two different systems were explored for electrochemical etching of desired samples.

System #1: Electrolyte of 30 vol. % H_3PO_4 and 70 vol. % ethyl alcohol is used. Solution is stirred using heating magnetic stirrer, AREC at 500 rpm. The electrochemical setup is surrounded by ice for temperature adjustment to 0 ^{o} C. Potential of 60 V is applied for 20 minutes.

System #2: Electrolyte of 20 vol. % $HClO_4$ and 80 vol. % acetic acid ($C_2H_4O_2$) at room temperature is used. Potential of 35 V is applied for 4 minutes.

3.3.3. Chemical polishing

Chemical etching was done using etching system of hydrofluoric (HF) and nitric acid (HNO_3). Prepared etching solution consisted of 5 vol.% HF, 15 vol% HNO_3, 80 vol.% distilled water. Samples were immersed in the etching solution for 10-15 minutes. After removal, it was cleaned with distilled water under unltrasonication for 1 minute.

3.4. Morphological characterization

Images were obtained for morphological characterization of Ti and Ti-alloys samples fabricated and treated with different conditions, using Field Emission Scanning Electron microscope. FESEM, Leo Supra 55 – Zeiss Inc., operated at 9.00 kV, was used to capture these images. Images were used to detect the success of nanoarchitecture fabrication, measuring dimensions, and study the effect of surface treatment prior and after anodization. FESEM was

also used to study cell proliferation on different samples morphology as will be explained in a later section. Finally, it was used to detect the accumulation of drug on sample surfaces post drug loading experiment.

Only samples upon which is attached the cell culture are gold-sputtered before imaging to enhance conductivity for better imaging. Otherwise, all samples were imaged as is.

3.5. Thermal Annealing

As required, as-anodized samples were thermally annealed in a furnace for a pre-specified time. They were subjected to a temperature of 450 ^{o}C in air, with ramping heating rate of 1 ^{o} C/min. Samples were annealed either prior to some characterization techniques, including XRD, second run for the nanoindentation and number of FESEM-characterized samples, or as surface treatment for controlling surface oxide layer. Steady temperature of 450 ^{o}C was maintained for time interval of 2, 3 or 4 hours according to the purpose of the treatment. Furnace used was Lindberg/Blue M^{TM} Tube furnace, Thermo scientific, as shown in Figure 3.2.

Figure 3.2: Lindberg/Blue M^{TM} Tube furnace, Thermo scientific, used in samples annealing.

3.6. Structural and Compositional Characterization

Four different techniques were used to identify and confirm structure and/or composition of fabricated NTs layer on Ti-17Nb-6Ta alloy. These techniques included:

- XRD diffractometer (D8, Brucker) with a copper tube of 1.54Å wavelength.
- High Performance Raman Analyzer (ProRaman-L) with an excitation laser beam, wavelength of 532 nm.
- Energy Dispersive X-ray Spectroscopy (EDX) detector equipped on FESEM, Leo Supra 55 – Zeiss Inc.
- X-ray Photoelectron Spectroscopy (XPS) on a Thermo Scientific K-alpha XPS with an Al anode. Spectra charged at 532 eV reference to O 1s.

3.7. Mechanical Characterization

Young's Modulus and Hardness of the samples were measured before and after annealing (at 450 ^{o}C for 3 hours). Tests were done using Nano Indenter XP, MTS with berkovitch tip (20 nm) creating 6 X 6 array of indentations, separated by 150 µm. Nanoindentation was done with CSM Tip Calibration mode, strain 0.05 S^{-1}, depth 3000 nm and strain rate 10 nm/sec. FESEM was used to image the indentation projected contact area caused by the Berkovich tip.

3.8. Assessment of Nanoarchitectures' Biological Response

For biological assessment vascular endothelial cells were extracted from mice umbilical cords and cultured *in-vitro*. They were used for cytotoxicity measurements, cells adhesion and proliferation on NTs. These tests were conducted at the holding company for biological products and vaccines (VACSERA) and described as follows:

3.8.1. Cytotoxicity Measurements

Cytotoxicity was assessed for Ti-17Nb-6Ta sheets as received, with Homo-NTs and Hetero-NTs structures using MTT assay.

3.8.1.1. Sample Preparation

- Samples were incubated in shaker incubator at temperature of 37 ^{o}C in culture media overnight.
- Samples' extracts were collected after incubation.
- Extracts were diluted serially to study cytotoxicity with MTT assay as will be described as follows.

3.8.1.2. MTT Kit

- MTT kit is based on reductive coloring reagent to detect mitochondrial dehydrogenase in living cells. MTT in this assay is reduced by NADH to purple formazan.
- Needles shaped crystals colored in purple are formed by MTT formazan due to its water insolubility.
- To solubilize these crystal, organic solvent is used. This allowed measurement of absorbance to quantify cells viability.

3.8.1.3. MTT Assay:

1- Vascular endothelial cells were grown in culture media as monolayer. Media is supplemented with fetal bovine serum, inactivated, 10%.

2- Cells were plated in 96-well tissue culture plate with 10^4 /well. They were incubated at temperature 37 ^{o}C with 5% CO_2 in a humidified incubator for 24 hours to allow cells

attachment to the plate before adding samples extract. This step is excluded for blank wells, which is used with no cells.

3- Different dilutions from samples extracts were added for testing cytotoxicity, except for cell control wells. For each concentration, eight replicates were prepared, as shown in plate design in Table 3.2 below.

Table 3.2: Plate design used for cytotoxicity MTT assay of different nanoarchitectures versus as received substrate material.

	Blank	Cell Control	Homo-NTs			Hetero-NTs			Alloy substrate			12
A			0	-1	-2	0	-1	-2	0	-1	-2	
B			0	-1	-2	0	-1	-2	0	-1	-2	
C			0	-1	-2	0	-1	-2	0	-1	-2	
D			0	-1	-2	0	-1	-2	0	-1	-2	
E			0	-1	-2	0	-1	-2	0	-1	-2	
F			0	-1	-2	0	-1	-2	0	-1	-2	
G			0	-1	-2	0	-1	-2	0	-1	-2	
H			0	-1	-2	0	-1	-2	0	-1	-2	

4- Cells were cultured with the added samples extracts for 48 hours at temperature 37 ^{o}C with 5% CO_2.

5- After 48 hours, attached viable cells were separated by discarding culture media through decantation. Discard media contained both samples extracts and dead cells.

6- Plate is afterward washed twice, using PBS (pre-warmed).

7- MTT reagent of 40 µl was added to each well including negative control wells and blank.

8- After adding MTT, plates were incubated for 4 hours in the dark to allow for the reductive effect of mitochondrial dehydrogenase from viable cells to take place on MTT reagent. Accordingly, MTT will change into purple needles of Formazan.

9- Purple needles of Formazan were solubilized by 150 µl DMSO, added to each well.

10- To determine concentration in different well, absorbance was measured with microplate reader (ROBONIK TM P2000 Eliza plate reader) at 570 nm.

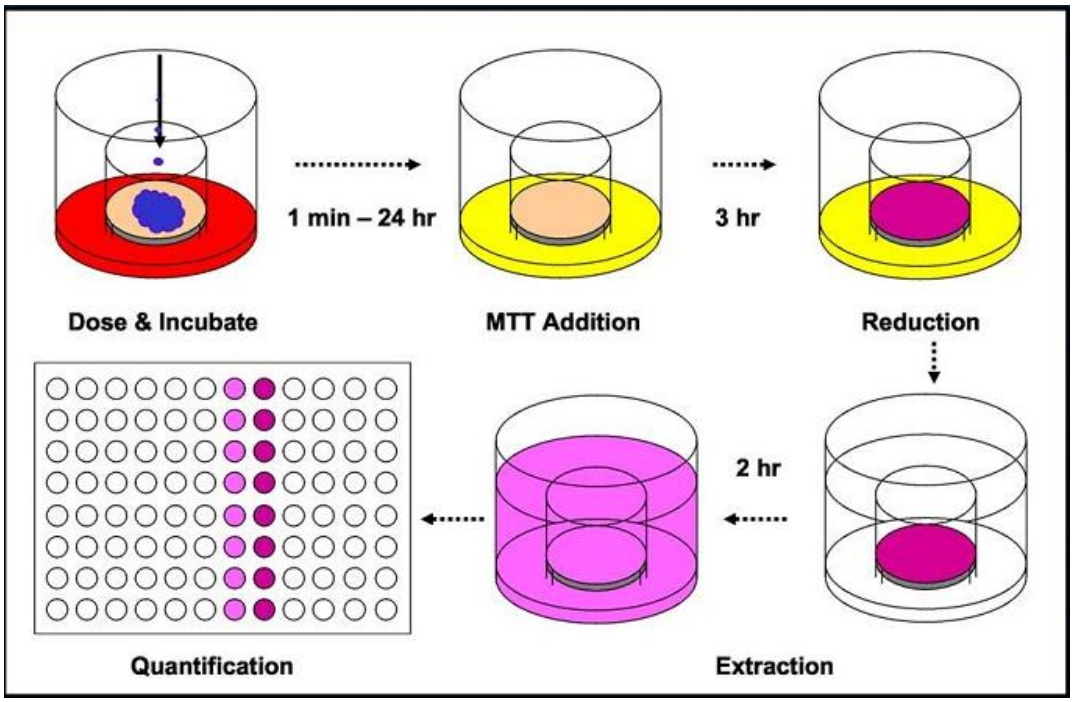

Figure 3.3: Diagrammatic representation of MTT assay steps [168].

3.8.2. Cell Proliferation Assay

The following assays were conducted to study vascular endothelial cells proliferation on different nanoarchitecture morphologies versus as received smooth Ti-17Nb-6Ta surface. Endothelial cells were plated on the three Ti-alloy samples (As received, Homo-NTs, Hetero-NTs) with cell densities of 5000 /cm^2. Cells were incubated at 37 ^{o} C with 5% CO2 and 70% humidity for 24 hours. Afterwards, non-adherent cells were washed away using phosphate buffer saline (PBS), to only leave adherent cells on surface of Ti- alloy samples.

Cell growth was analyzed after plating by counting adherent cells at days 1, 3 and 7. Analysis was done by MTT viability assay (described earlier), Tryptan blue viability assay and imaging under FESEM as described below:

3.8.2.1. Tryptan Blue Viability

1- The cells monolayer was detached by trypsinization with Trypsin/EDTA (Ethylene Diamine Tetraacetic Acid) solution (0.25%). Detached cells were re-suspended in fresh medium that contains fresh bovine serum.
2- 100 µl of re-suspended cells were mixed with equal amount of tryptan blue (dilution factor = 2) by gentle pipetting.
3- Hemocytometer and cover slip (shown in Figure 3.4) were thoroughly cleansed using 70% ethanol, before sliding the cover over the chamber.
4- 10 µl of cells suspension were added to both chambers of the hemocytometer and inverted microscope was used to examine cell viability.
5- Bright non stained cells indicated viable cells, while blue stained ones indicated dead cells. Both types of cells were counted under the microscope to calculate percentage of cells viability.

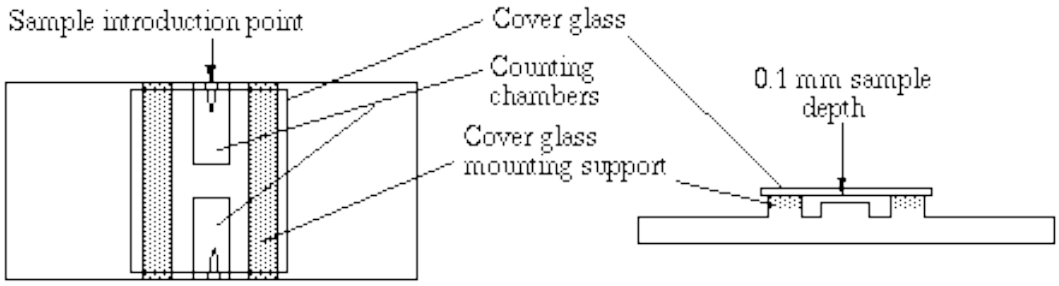

Figure 3.4: Diagrammatic representation of hemocytometer used in Trypan blue assay [169].

3.8.2.2. Cell Imaging by FESEM

Endothelial cells were cultured on the as anodized samples for 3 days. Afterwards, fixation of proliferated cells was done using gluteraldehyde, diluted with PBS. Samples surface were gold-sputtered at 20 mA for 1 minute, using SEM coating unit E5000, Polaron Equipment Limited. Samples were imaged using FESEM, Leo Supra 55 – Zeiss Inc., operated at 5.00 kV.

3.9. Study of Nanoarchitecture as Potential Drug Carrier

3.9.1. Drug Loading

Both Homo-NTs and Hetero-NTs were studied as potential drug reservoirs for the application of drug eluting stents (DES). Amount of loaded drug were compared between the two systems to determine the more favorable platform. Triplicates were prepared and examined for each platform to ensure reproducibility. Hydrophilic 2'-deoxyadenosine was used as the cytotoxic drug molecule.

Steps for quantifying the percentage of drug loaded are described below:

1- For each sample, known concentration of the drug solution was prepared as 1 mg 2'-deoxyadenosine per 1 ml distilled water in a 10 ml beaker (applying sink conditions).
2- Solution was stirred on magnetic stirrer (AREC) at 500 rpm for 2 minutes till complete solubility.
3- One side of the as anodized cleaned samples were covered by an insulating material to ensure drug loading into one side of the Ti-based anodized sheets.
4- Samples of 1 cm^2 were immersed in the prepared solution and left for 36 hours without stirring.
5- After the 36 hours, samples were removed from the drug solution and left to dry in air for 12 hours.
6- Insulating material was removed from the samples.
7- Each of the samples loaded with drug was immersed in a 10 ml beaker, containing 10 ml PBS under magnetic stirring for 3 minutes at 700 rpm.
8- 1 ml of the PBS were withdrawn from the beaker using a pipette and its absorbance was measured using CARY 500 scan, UV-Vis-NIR spectrophotometer at 260 nm.
9- For calculating the unknown concentration of drug released into the PBS, calibration curve presented in Figure 3.5 was used. For preparing the calibration curve, serial dilutions of known concentrations of the drug in distilled water were prepared and their

absorbances were measured at 260 nm. Absorbance was plotted versus concentration with setting trend line interception to zero.

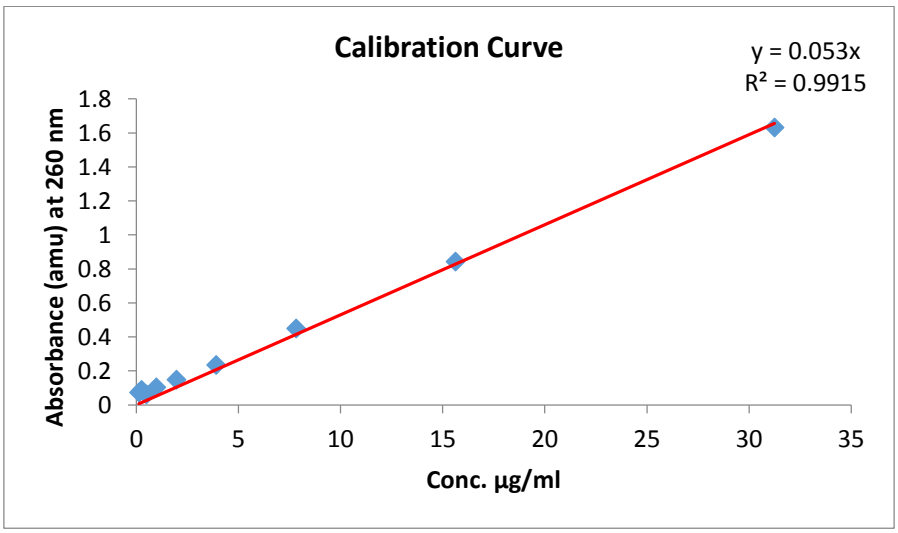

Figure 3.5: Calibration curve of 2'-deoxyadenosine in distilled water.

3.9.2. Drug Release Computational Study

Drug release profile from NTs was theoretically predicted using computational simulation. The model was built using COMSOL Multiphysics ® 4.1 modeling software. To simulate the kinetics of drug release from the NTs, "Transport of diluted species" module was used, with Fick's law equation governing the drug motion. Boundary conditions stated that flux outside the boundaries of the NTs and the tissue is equal to zero.

Chapter 4: Results and Discussion

Chapter 4: Results and Discussion

Reference to the challenges currently facing drug eluting stents, which were discussed earlier in chapter 1, the need for surface optimization of stent materials is considered crucial. Efficient surface composition and morphology should allow controlled endothelial tissue healing to avoid late thrombosis. On the other side, it should offer an ability to act as a drug carrier for local drug delivery to avoid neointimal hyperplasia and vessel restenosis. This chapter covers the results and discussion of the work undertaken to fabricate a nanoarchitectured system that shall enhance tissue proliferation and can possibly act as drug reservoir.

4.1. Fabrication of Highly Ordered Arrays of Ti and Ti-Alloys Nanoarchitecture

As discussed in chapter 2, few attempts were conducted to study the use of nano-surface morphology for the use in drug eluting stents. However, reported results studied nanoarchitectures fabricated from a material coated on the main stent substrate material. This is done for two main reasons: 1- due to the sensitivity of the application to the material mechanical properties. Stent material needs fine adjustment and tradeoff between mechanical properties affecting the stent flexibility and strength that was not offered by the coating material alone. 2- The coating was used as a biocompatible insulator between the vessel tissue and stent substrate material that can possibly release cytotoxic metal traces. Nevertheless, self-grown nanoarchitectures from the stent substrate can potentially be of greater benefit than different coating-substrate materials. This shall reduce the number of processing steps required for material coating and prior treatment to enhance adhesion. Self-grown layer would better avoid stresses gradient and allow for better stronger bond.

In an attempt to present this self-grown system, fabrication of nanoarchitectures on Ti-17Nb-6Ta alloy was investigated. Ti-17Nb-6Ta alloy is a potential material for self-expandable stent that is meeting the biocompatibility and mechanical properties required for such application. Their mechanical properties are comparable to Nitinol, which is currently the most widely used material for self-exandable stents. Ti-17Nb-6Ta alloy has a Young's modulus of 68 GPa, ultimate tensile strength (UTS) of 700-1050 MPa, Elongation of 10-30% and corrosion

resistance of -44.1 E_{corr} (mV). Furthermore, the tantalum content can possibly enhance radio-opacity and stent visibility during PCTA due to its relatively high density. To fabricate ordered morphology of nanoarchitectures on Ti-17Nb-6Ta ternary alloy, Ti pure and Ti-Nb binary alloys were first investigated for optimization.

4.1.1. Pure Ti as Nanoarchitecture Substrate

Both aqueous and organic electrolytes for anodization setup were investigated. For aqueous conditions, electrolyte PD1 from Table 3.1 was used. While for organic conditions, electrolytes FP2 and FG3 were used. Figure 4.1 shows FESEM images for the as-anodized nanotubes arrays. Aqueous electrolyte resulted in the formation of nanotubes (NTs) that are distributed over the entire substrate. The NTs diameter varied widely along the layer (from 70 to 100 nm). However, outer diameter was observed to be irregular in structure with circumferential serration and ridges, which is common with aqueous electrolytes. Hence, organic electrolytes were investigated to optimize the NTs morphology, including alignment, dimensions and wall regularity.

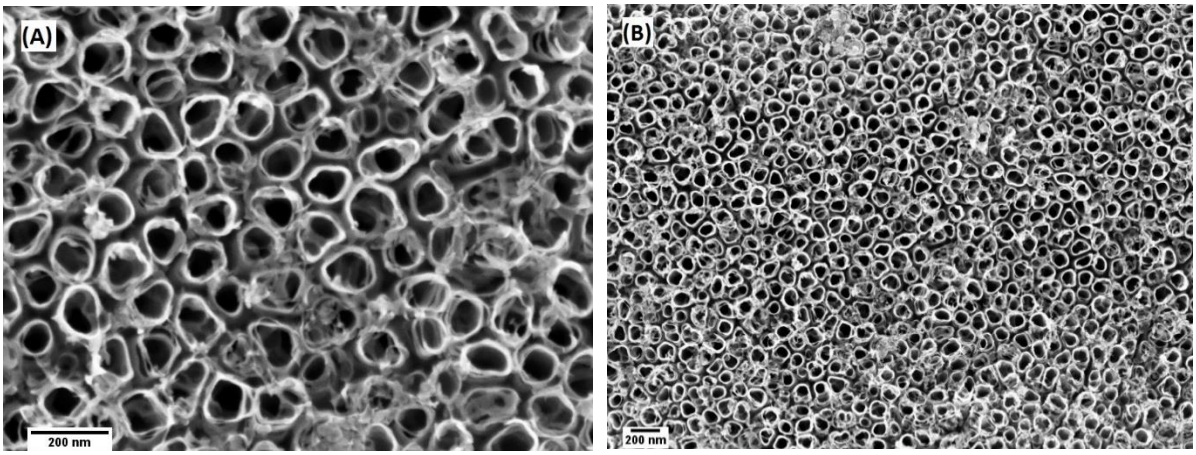

Figure 4.1.: Top view FESEM images of as-fabricated TiO_2 NTs anodized in aqueous electrolyte at (A) higher and (B) lower magnification.

Regarding the use of organic electrolyte, first, formamide-based electrolyte (FP2) was used. As shown in Figure 4.2. (A) and (B), the NTs structure was observed to be more defined. NT diameter became more uniform (110 ± 10 nm). However, circumferential serration is still observed. Furthermore, nanotubes are slightly bent inwards forming nanoscaled islands, distributed along the substrate. Reducing the formamide content was followed for glyceol-based electrolyte (FG3). It can be seen in Figure 4.2 (C) and (D) that NTs were significantly enhanced towards more vertical alignment and smoother surface.

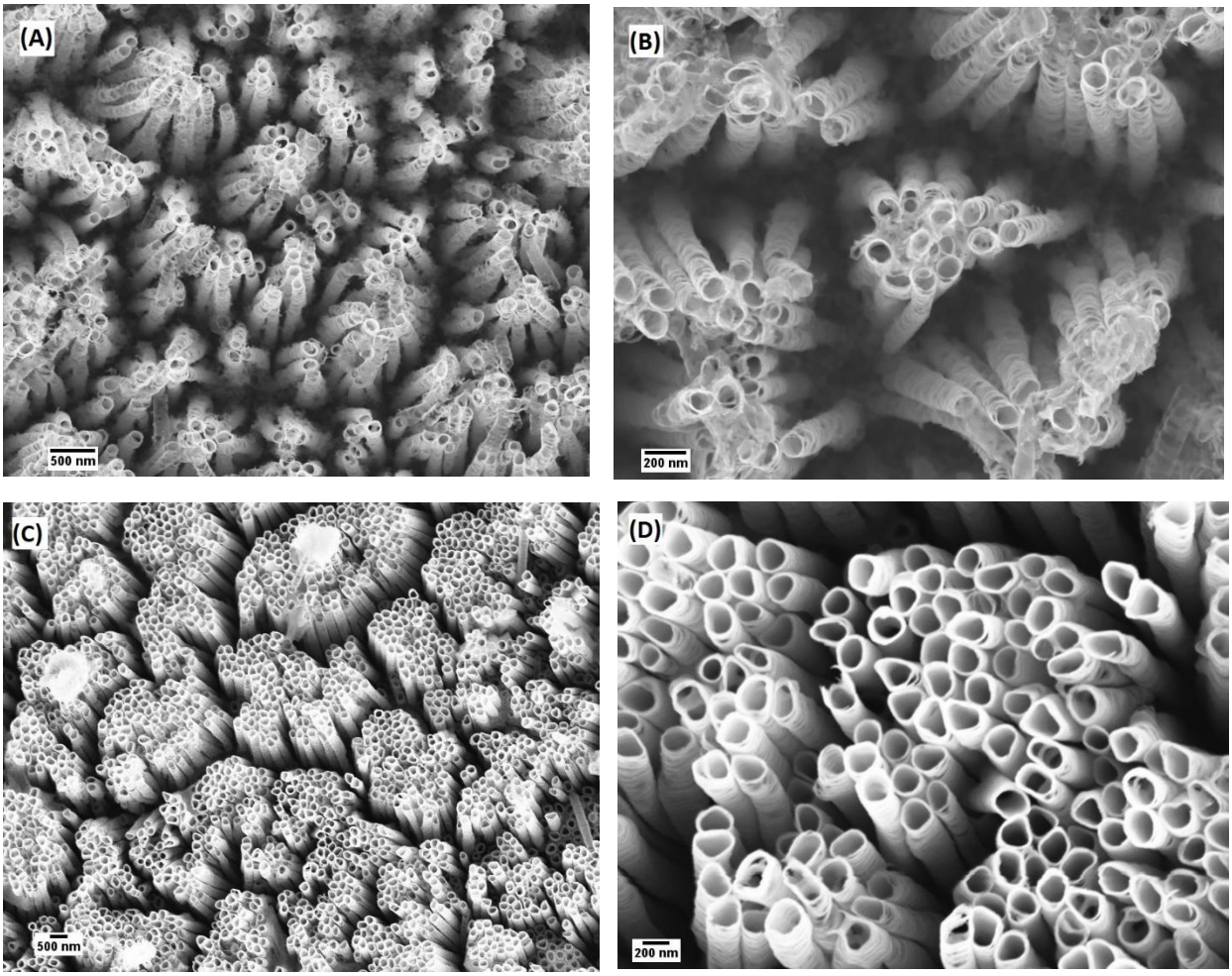

Figure 4.2.: Top view FESEM images of as-fabricated TiO_2 NTs in formamide based electrolytes at (A) lower and (B) higher magnification, and glycerol based electrolytes (C) lower and (D) higher magnification.

4.1.2. Ti-45Nb Alloy as Nanoarchitecture Substrate

Aqueous and organic electrolytes were explored for the anodization process of Ti-Nb alloy to study the effect of electrolyte type on surface morphology. For aqueous-based electrolytes, AD4 electrolyte was used at 40 V for 2 hours. It is evident from the FESEM images of Figure 4.3 that vertically aligned nanotubes were successfully fabricated.

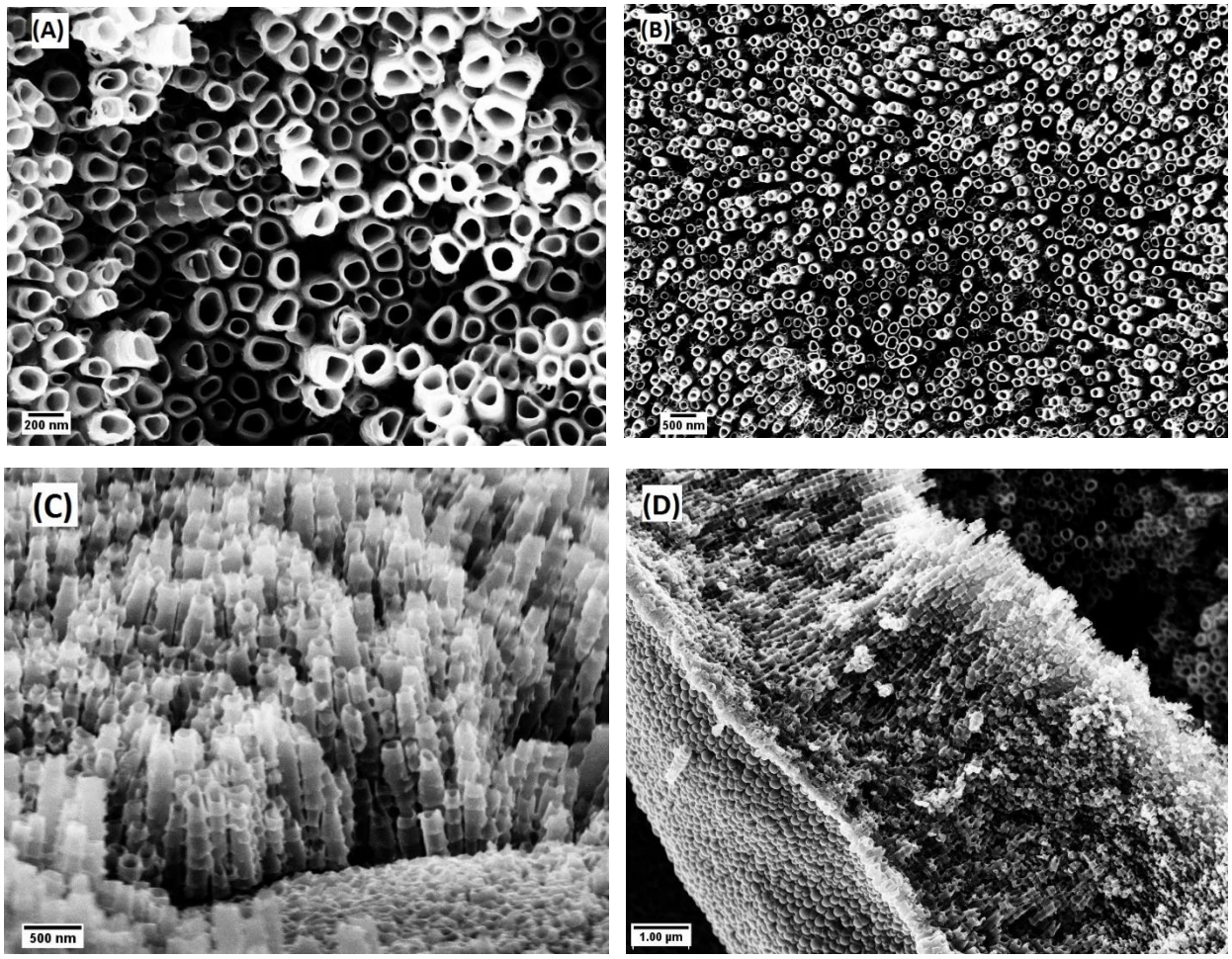

Figure 4.3.: FESEM images of as-fabricated NTs of Ti-45Nb obtained in aqueous (AD4) electrolye. (A) and (B) are top views of the NTs at high and low magnification, respectively, showing NTs heterogeneous dimensions and well distribution. (C) Side view of the NTs from imaging the sample at 90 degrees, showing the circumferential serration. (D) Side view of the NTs layer through imaging a detached area, showing the NTs base and the layer total length.

Although the NTs are more defined, they still have circumferential serrations. It was also observed that the NTs are well-distributed over the substrate with heterogeneous dimensions within the same layer. NTs inner diameter varied widely between 75 and 145 nm, while the NTs wall thickness ranged between 5 and 20 nm. The measured thickness of the NTs layer (as shown in Figure 4.3 (D)) was found to be of average 5 µm despite of observed irregularity.

As described earlier, the NTs morphology was significantly enhanced with glycerol-based relative to formamide-based electrolytes in case of pure Ti. Accordingly, Ti-45Nb sheets were anodized using FG3 electrolyte. When as-anodized samples were imaged under FESEM, thick oxide layer was observed covering the NTs layer, which can negatively affect the NTs functionality for the specified application. As shown in Figure 4.4 (B), well-defined NTs can be seen beneath the oxide layer. Anodized samples were therefore further cleansed for longer amount of time. They were ultrasonicated in acetone for 30 minutes and imaged again.

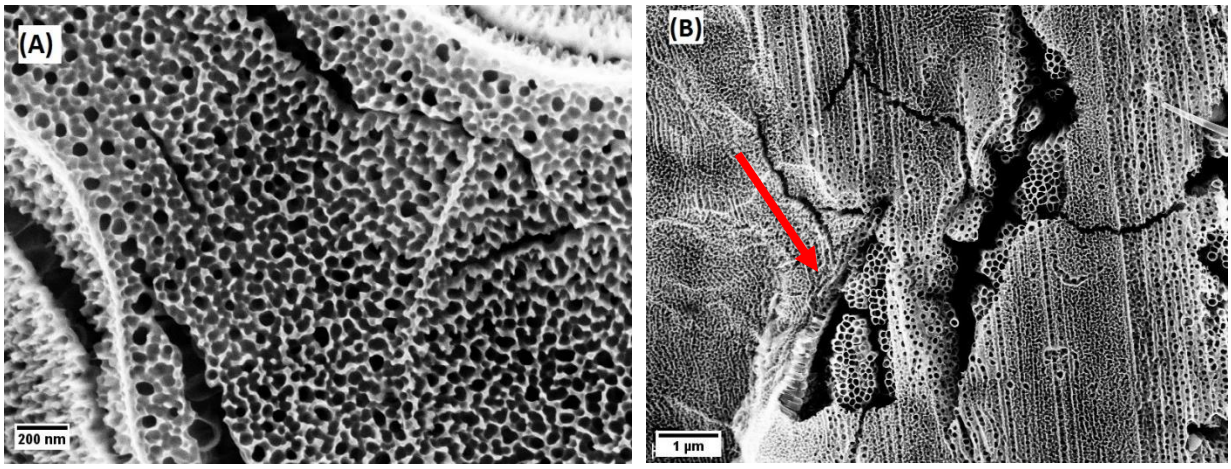

Figure 4.4: Top view FESEM images of as-anodized Ti-45Nb sheets in FG3 electrolyte. (A) Thick porous oxide layer formed on the surface of the NTs and (B) arrow points to the well-defined NTs beneath the oxide layer.

It can be clearly seen from Figure 4.5 that sonication for long duration successfully removed the undesired oxide layer without compromising the nanoarchitectured layer. Highly ordered vertically oriented assemblies of nanotubes were revealed. They appear as closely packed NTs with almost fused walls at the surface between adjacent NTs. They are assembled into honey-comb like islands separated by grooves. It can be observed that NTs walls are highly uniform and free from circumferential serration.

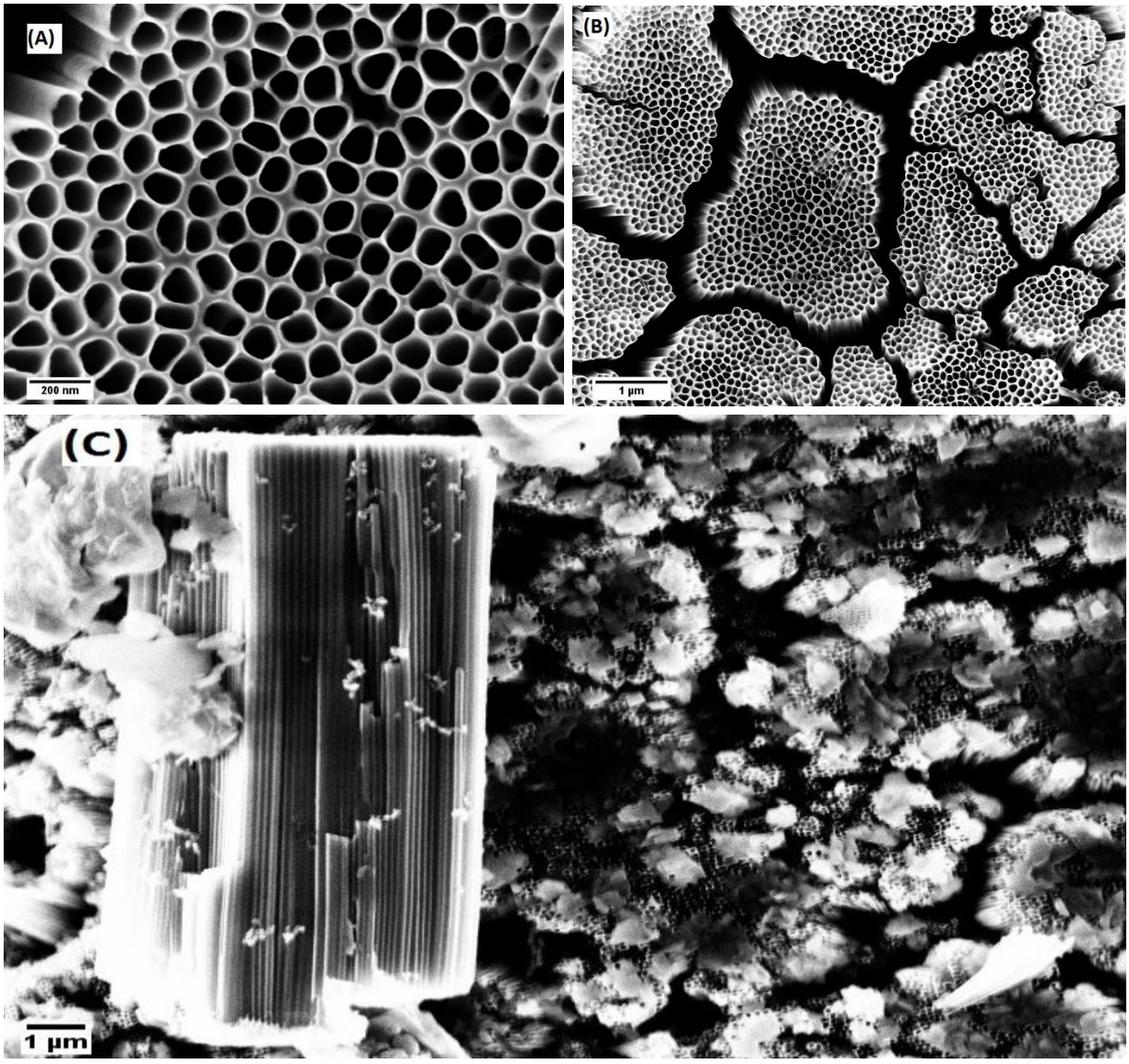

Figure 4.5: FESEM images of Ti-45Nb honey-comb like nanoarchitectures, fabricated using glycerol-based electrolytes. (A) and (B) top view images of low and high magnification, respectively, and (c) side view from detached area after surface scratching.

Furthermore and most importantly for the intended application; the NTs are homogeneous in structure and dimension. Measured inner diameter is of average 90 ± 10 nm and fused walls thickness of 11 ± 2 nm. Detached area from the NTs layer was imaged showing the layer side view in Figure 4.5 (C). It showed long highly uniform vertically aligned NTs with average length of 14 μm. It is evident from the figure that dimension of the tubular structure is nearly uniform throughout the tubes' length.

4.1.3. Ti-17Nb-6Ta as Nanoarchitecture Substrate

Based on the extremely promising results obtained from using FG3 electrolyte with Ti-45Nb alloy, it was studied with the Ti-Nb-Ta alloy sheets to reproduce such ordered nanoarchitectural structure from Figure 4.5. As received samples were anodized using the same conditions of FG3 electrolyte mentioned in Table 4.1. First outcome resulted in the morphology observed in Figure 4.6. It showed highly rough layer that is totally covering the substrate. Evidence of NTs assembly were clear from Figure 4.6 (B) and (C) where NTs were seen either detached or underneath the rough surface. However, this structure can completely hinder the functionality of the nanoarchitecture and it is essential to remove it. Cleaning attempts using ultrasonication for long duration failed to overcome this problem and other techniques needed to be explored.

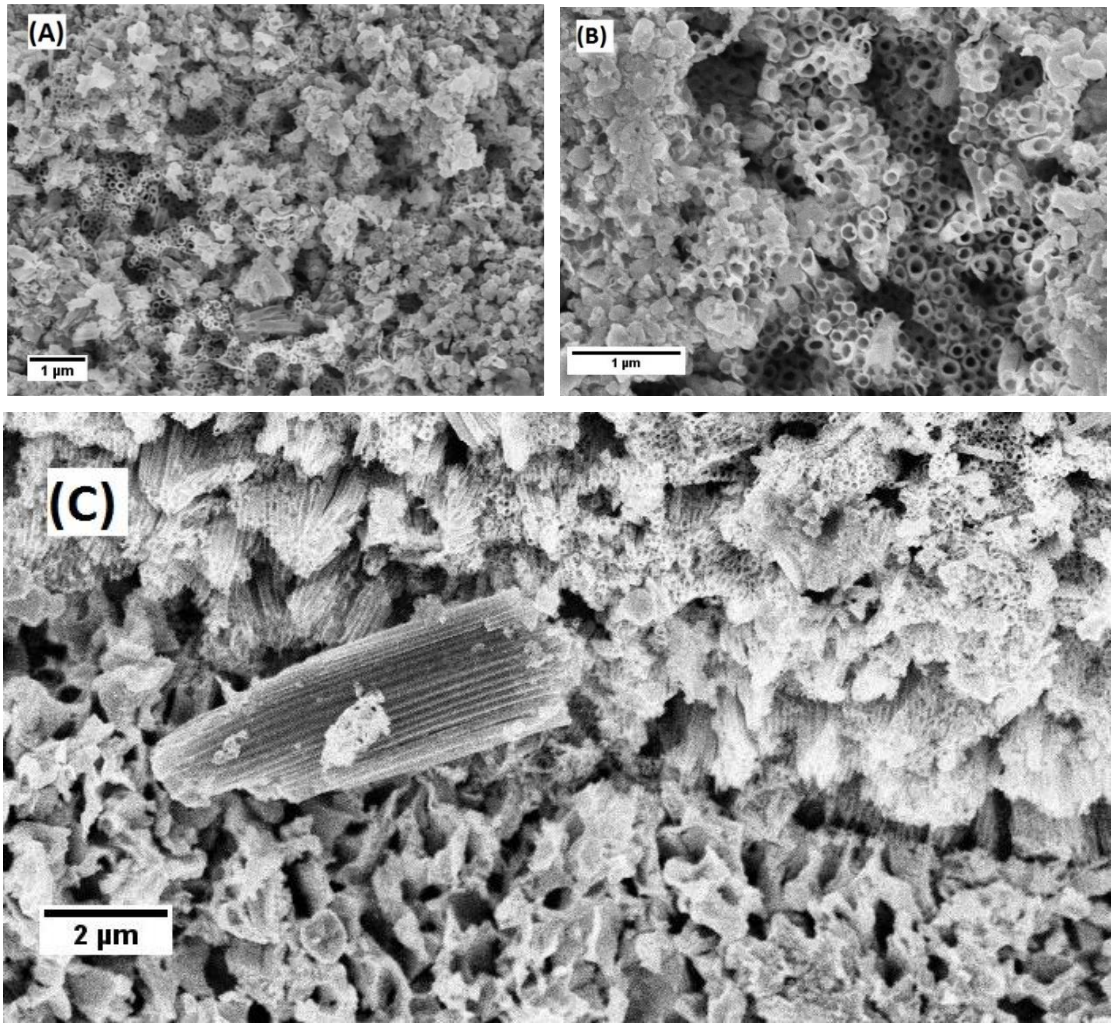

Figure 4.6: FESEM images of (A) high rough surface on as anodized samples, (B) NTs beneath the layer, and (C) detached NTs assembly.

Referring back to the thermal history of the received Ti-17Nb-6Ta alloy sheets, it was found that they were oxidized at high temperature of about 800 ^{o}C. This is sufficient to result in a thick oxide layer prior to any electrochemical processing. As received samples were therefore imaged prior to anodization to examine surface roughness and optimize accordingly. As shown in Figure 4.7 highly rough surface was observed on Ti-17Nb-6Ta substrate. This rough structure can most probably remain persistent after anodization and cause the observed rough layer covering the nanotubes. Prior anodization processing was therefore essential to prepare the sample for NTs fabrication. Accordingly, sample polishing prior to anodization was studied through a sequence of different techniques with varying outcomes.

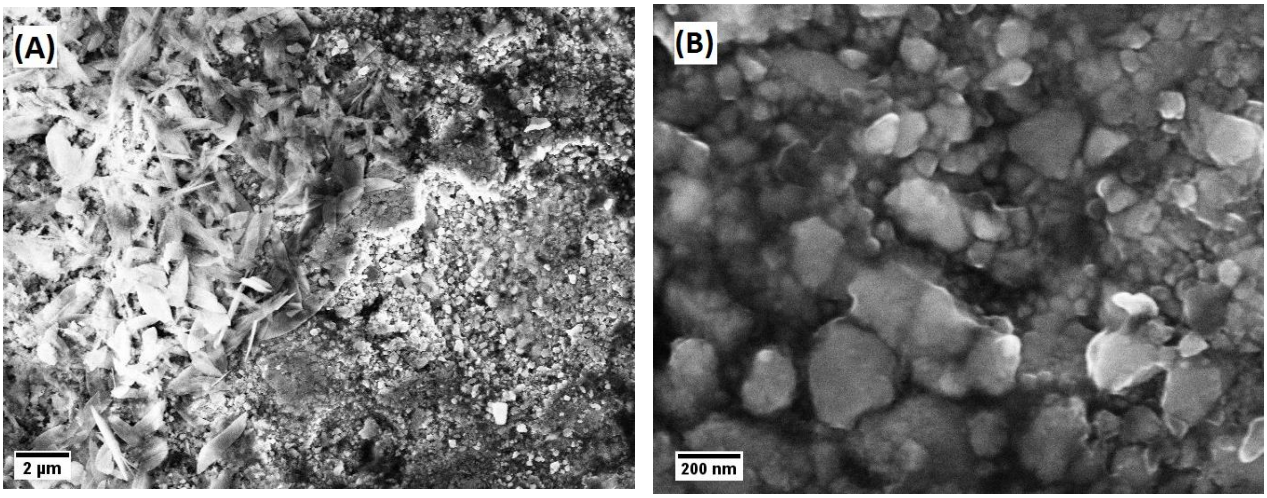

Figure 4.7.: Top view of FESEM images for as received Ti-17Nb-6Ta alloy sheets prior to anodization, at (A) lower and (B) higher magnification.

4.1.3.1 Mechanical Polishing

Manual polishing was first explored using grinding paper to gently polish the surface manually prior to anodization. Samples were afterwards anodized using FG3 electrolyte conditions. For as anodized samples, FESEM images showed improvement in surface morphology. Highly rough surface was not observed anymore. However, it was replaced by another morphology of oxide layer covering almost all the substrate surface. This layer can be described as thick nanoporous oxide layer with NTs of thick walls appearing beneath, as shown in Figure 4.8.

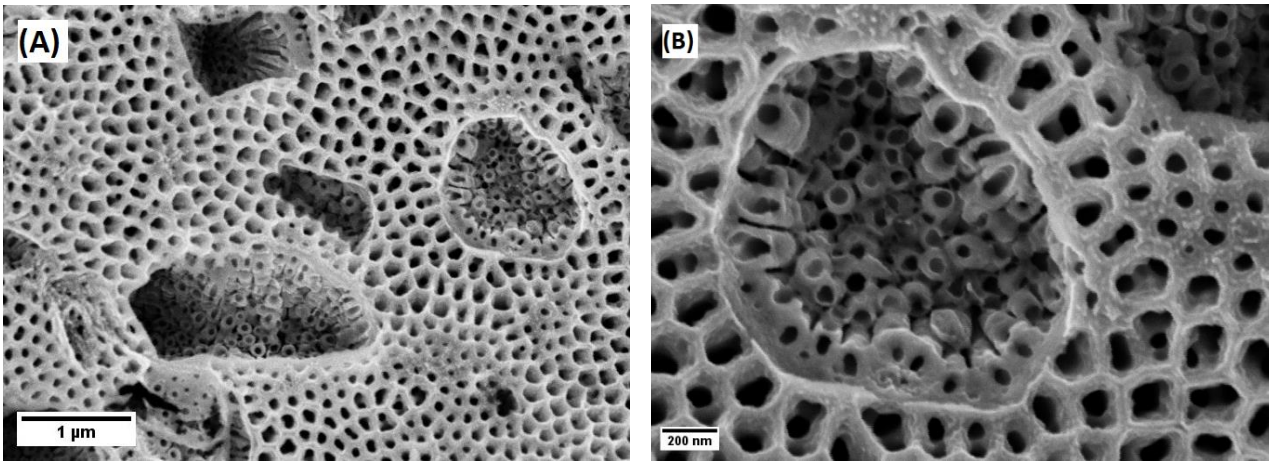

Figure 4.8: Top view FESEM images for pre-polished anodized Ti-17Nb-6Ta sheets, showing nanoporous oxide layer covering the underneath NTs at (A) low and (B) high magnification.

In attempt to avoid the build-up of the oxide layer, manual polishing was replaced by automated mechanical polishing described in chapter 3. Samples were anodized post polishing using FG3 electrolyte with the same conditions previously described. As shown in Figure 4.9 (A), it was found that density of thick nanoporous oxide layer from Figure 4.8 decreased significantly. It showed larger pores diameter with thinner walls in between. Furthermore, NTs appearing beneath the layer became more uniform and vertically oriented, as shown in Figure 4.9 (B). The anodized layer, including both oxide layer and underlying nanotubes, was removed by ultrasonication in acetone for 30 minutes. Another step of anodization was performed on the same sample in attempt to guide a more uniform assembly of nanotubes, using the same electrolyte. As observed in Figure 4.9 (C), the less dense oxide layer appeared only in scattered areas along the substrate surface after second anodization. And large areas of nanoarchitectures started to be revealed. However, various morphologies of nanoarchitecture was observed in different areas along the sample, as shown in Figure 4.9 (D). These non-uniform assemblies can hinder the control over the intended outcome during application.

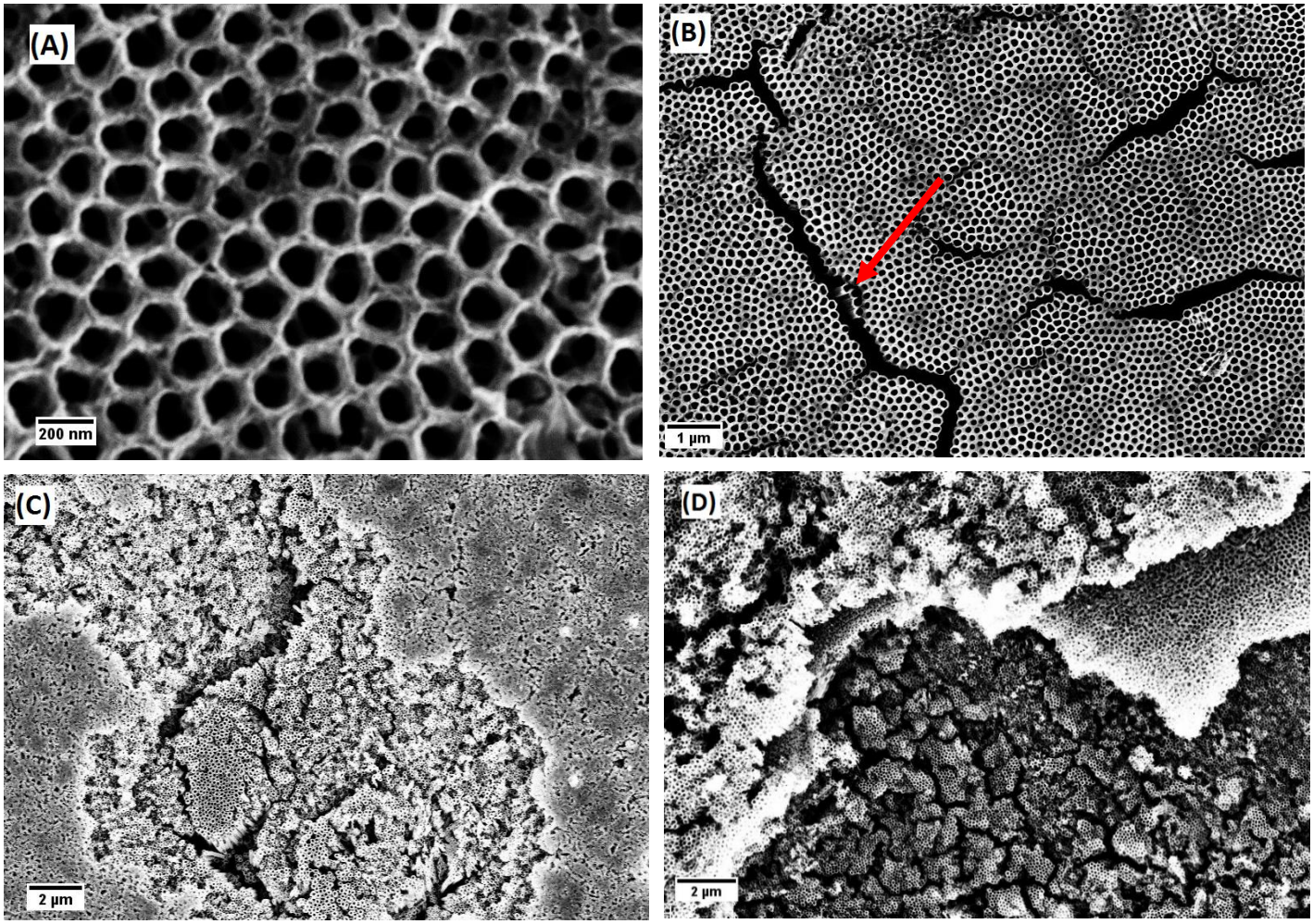

Figure 4.9: Top view FESEM image of the two steps anodization of Ti-17Nb-6Ta sheets after automated mechanical polishing. (A) and (B) shows the less dense nanoporous oxide layer covering the nanotubes at higher and lower magnification respectively. Arrow on image (B) shows uniform vertically oriented NTs beneath the oxide layer. (C) and (D) shows resulted structure from second anodization after removing the as anodized layer from step one using ultrasonication. (C) Shows that larger area of NTs started to reveal leaving the oxide layer with significant distance apart. (D) Covers different NTs morphology that was observed along the same substrate.

4.1.3.2. Electrochemical Polishing

In order to avoid surface abrasion, strains and contamination that can potentially be caused by mechanical polishing, electrochemical polishing was explored to optimize pre-anodization surface treatment. Two electrochemical setups were studied as described in chapter 3, followed by samples anodization using FG3 electrolyte. System #1 that used phosphoric acid at 30 vol. % was not successful in avoiding the oxide layer formation on the NTs surface. It can be seen in Figure 4.10 that pre-treatment with system #1 resulted in uniform NTs with relatively thick wall underlying a low-porosity oxide layer. The assemblies, however, showed islands-like morphology, separated by grooves characteristic for FG3 electrolyte.

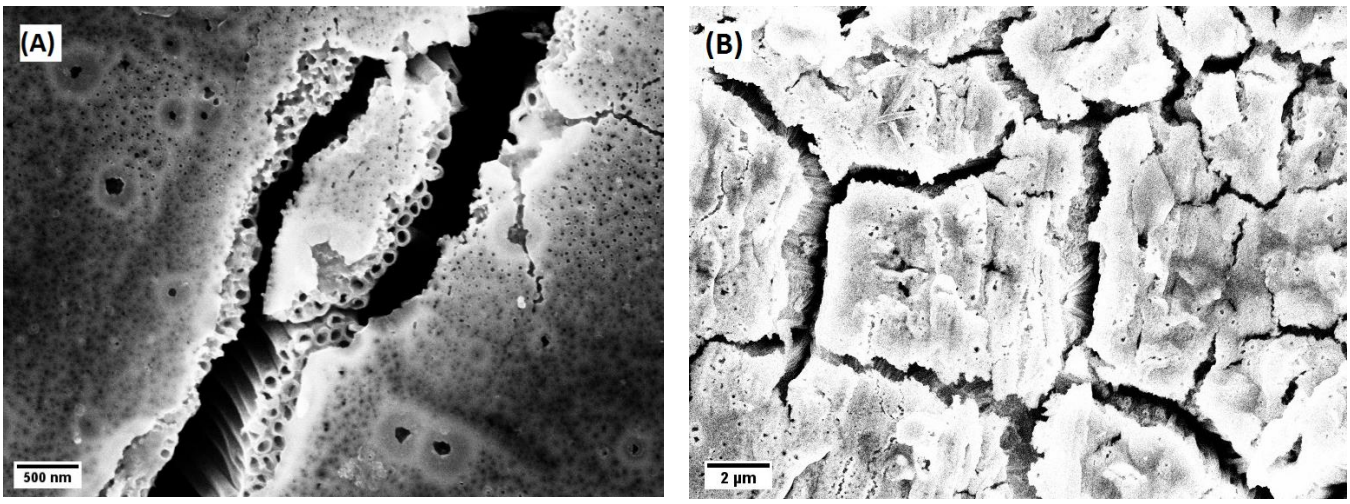

Figure 4.10: Top view FESEM images of as anodized Ti-17Nb-6Ta sheets after pre-anodization treatment using system #1 electrochemical anodization. (A) higher magnification showing uniform, vertically aligned nanotubes below the oxide layer. (B) lower magnification showing the island like assembly of NTs covered with low-porosity oxide layer.

Stronger acid (perchloric acid) was accordingly studied through system #2 for pre-anodization electrochemical treatment. More underlying NTs were revealed, as shown in Figure 4.11. NTs morphology was closer to the expected FG3 outcome with relatively thinner tubes wall, high vertical alignment and uniformity. However, although oxide layer was found more distant apart, it remained persistent with this polishing technique. Also, overall electropolished area was found to be about only 20% of the whole substrate surface area. Furthermore, NTs layer assembled on electropolished areas was easily detached with minimum stress. Hence, another technique had to be explored for sample polishing.

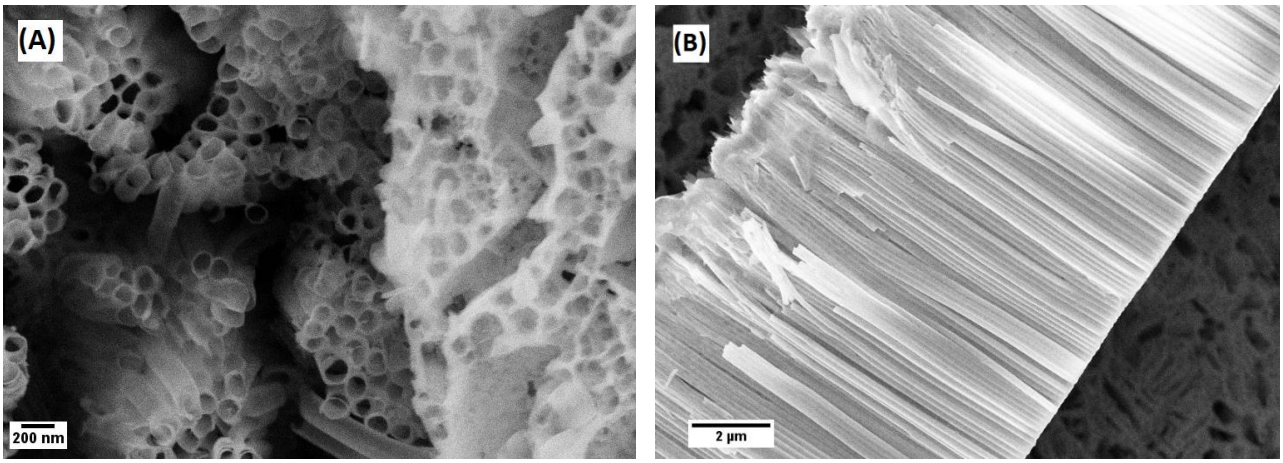

Figure 4.11.: FESEM images of as-anodized Ti-17Nb-6Ta samples, post electrochemical polishing using system #2. (A) Top view for relatively thin walled NTs close to the morphology produced by FG3 electrolyte. And it can also be seen to the right, oxide layer deposited on the surface. (B) Side view of highly ordered nanotubes assembly, detached from the layer of almost 11 µm in length.

4.1.3.3. Chemical Etching

Pretreatment in chemically etching solution as described in chapter 3, revealed the best results among the different explored polishing techniques. The very strong acid (HF) used resulted in the most successful solution to remove the oxide layer built on NTs surface without the need of external forces either mechanical or electrochemical. As seen in Figure 4.12, it only

left randomly distributed debris revealing highly ordered NTs. Among the previously described polishing techniques, chemical etching showed the best results. Results obtained from different polishing treatments confirmed that substrate preparation and pre-anodization treatment directly and greatly influence the final NTs morphology, uniformity and distribution.

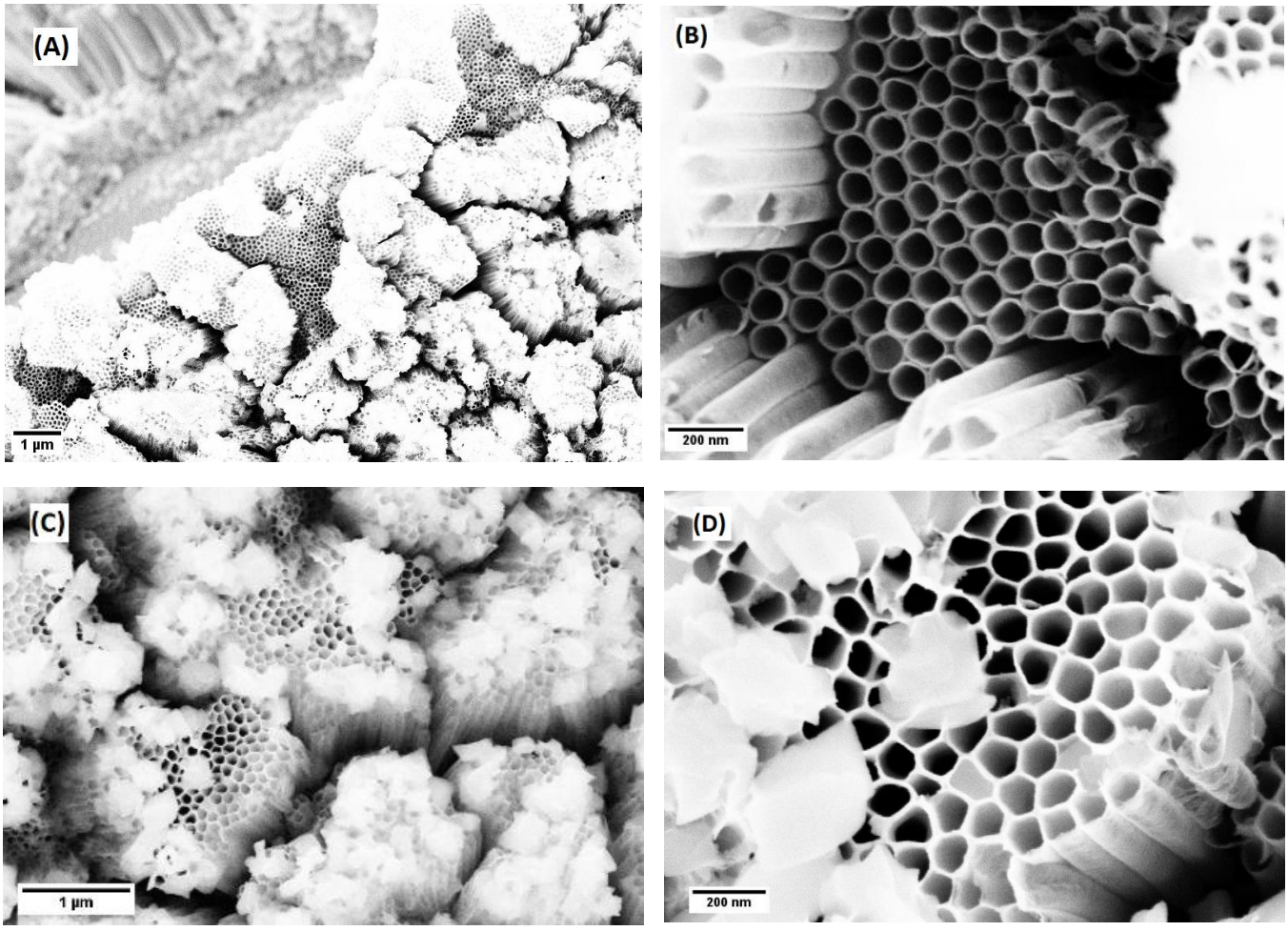

Figure 4.12.: Top view FESEM image of as anodized Ti-17Nb-6Ta samples, post chemical etching. (A) Lower magnification showing the relatively heterogeneous nanoarchitecture along the surface. (B) High magnification at area of highly ordered, vertically oriented NTs with morphology and dimensions as expected from FG3 electrolyte. (C) and (D) show the randomly distributed debris on as anodized NTs surface.

4.1.3.4. Unprocessed Ti-17Nb-6Ta Alloy

Based on the previously reported findings, anodization was done for samples with no thermal treatment history post preparation. After samples were cold rolled, they were directly anodized in attempt to avoid the oxide layer formation without the need of sample polishing. As expected, it is clear from Figure 4.13 that anodization using FG3 electrolyte conditions was successful to fabricate highly ordered, vertically oriented NTs for Ti-17Nb-6Ta substrate.

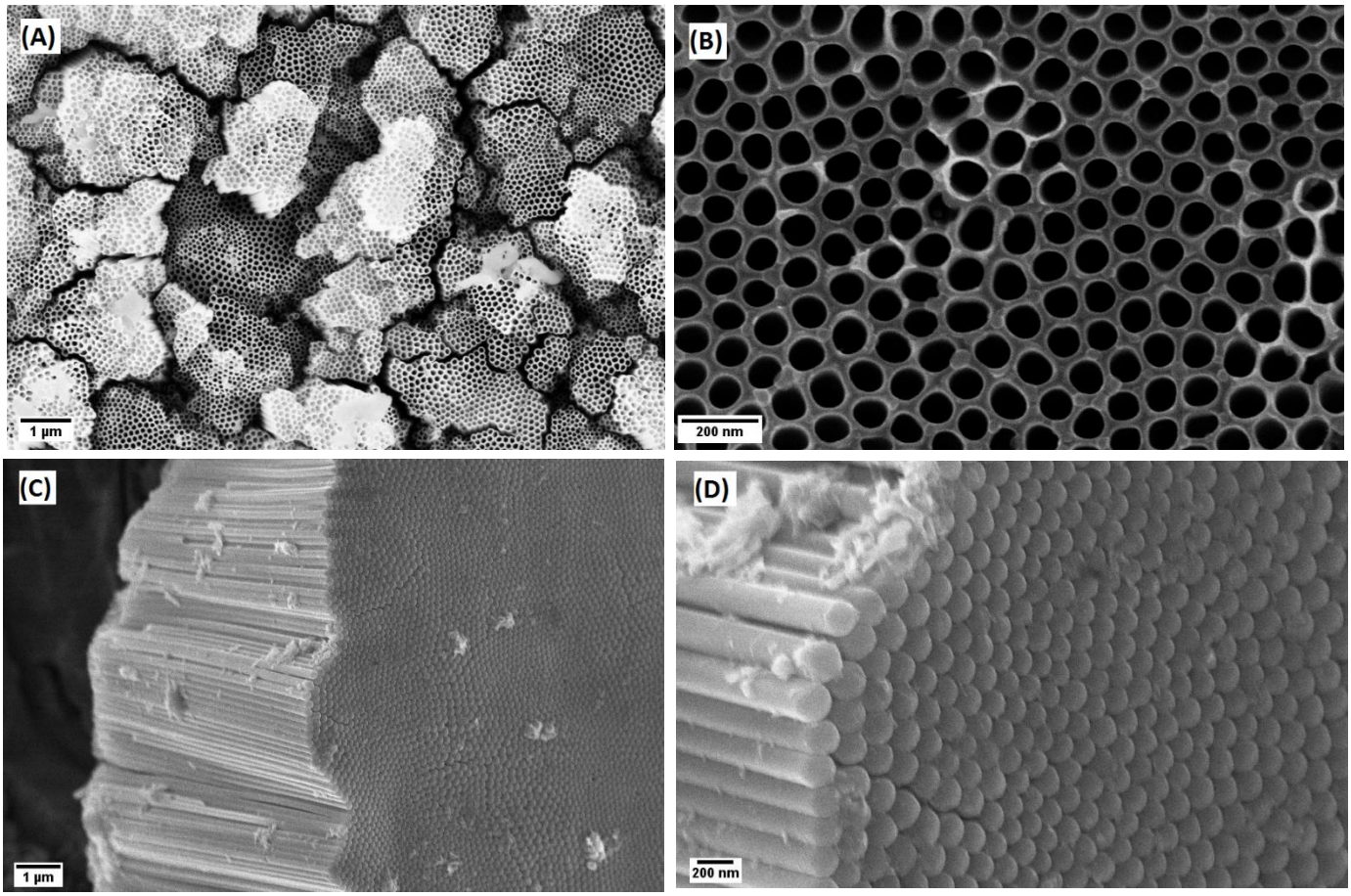

Figure 4.13: FESEM images of as-anodized Ti-17Nb-6Ta with no thermal treatment history. (A) Low magnification top view of the highly ordered, vertically oriented NTs packs, with dissimilar packs' length, (B) high magnification top view of the ordered NTs showing NTs homogenous structure, (C) and (D) side views of NTs detached layers, showing NTs bottom side at lower and higher magnification, respectively.

They can also be described as closely packed NTs assembled into honey-comb like islands separated by grooves. Packed NTs appeared having fused walls at the surface. Side view observed from detached layer or variation in packs length, showed highly defined NTs with distinct, uniform walls and free from circumferential serration. Tubes diameter is observed to be uniform along the length. As observed from bottom view of Figure 4.13 (C) and (D). It can be safely called homogeneous NTs (Homo-NTs), and will be the first morphology of nanoarchitecture proposed for the intended application. NTs dimensions were found to be of average inner diameter 75 ± 5 nm and length of 12 µm. Dissimilar packs' length of NTs is observed in Figure 4.13 (A). It is potentially justified by different etching rates of Ti-17Nb-6Ta alloy components by fluoride containing electrolyte reference to elements activity. This structure of homogeneous NTs was studied for enhancing drug eluting stents by enhancing material biological response and drug loading capacity as will be described in the following sections.

4.1.3.5. Variation in NTs Morphology for Biological Application

Aqueous electrolyte was studied for anodizing Ti-17Nb-6Ta with no thermal treatment history. This was an attempt to reproduce heterogeneous structure observed with Ti-45Nb by using aqueous electrolyte. Samples were anodized using AD4 electrolyte conditions and imaged with FESEM. As seen in Figure 4.14, anodization was successful to produce vertically aligned nanotubes, uniformly distributed on samples' surface. The structure is referred to as heterogeneous NTs (Hetero-NTs) since measurement of inner diameter and wall thickness varied significantly. Tubes' diameter ranged from 80 nm up to 190 nm along the same substrate. Wall thickness varied within range of 6 nm up to 28 nm. However, the length of NTs layer was found to be of average 12 µm. Heterogeneous NTs were fabricated to be studied in comparison with the previously described homogeneous NTs for the intended application. With almost similar layer length for the two morphology, this variable was excluded from the comparison. Effect of surface morphology between Homo- and Hetero- NTs was studied for endothelial tissue biological response and system capacity to load therapeutic agents for drug eluting stents.

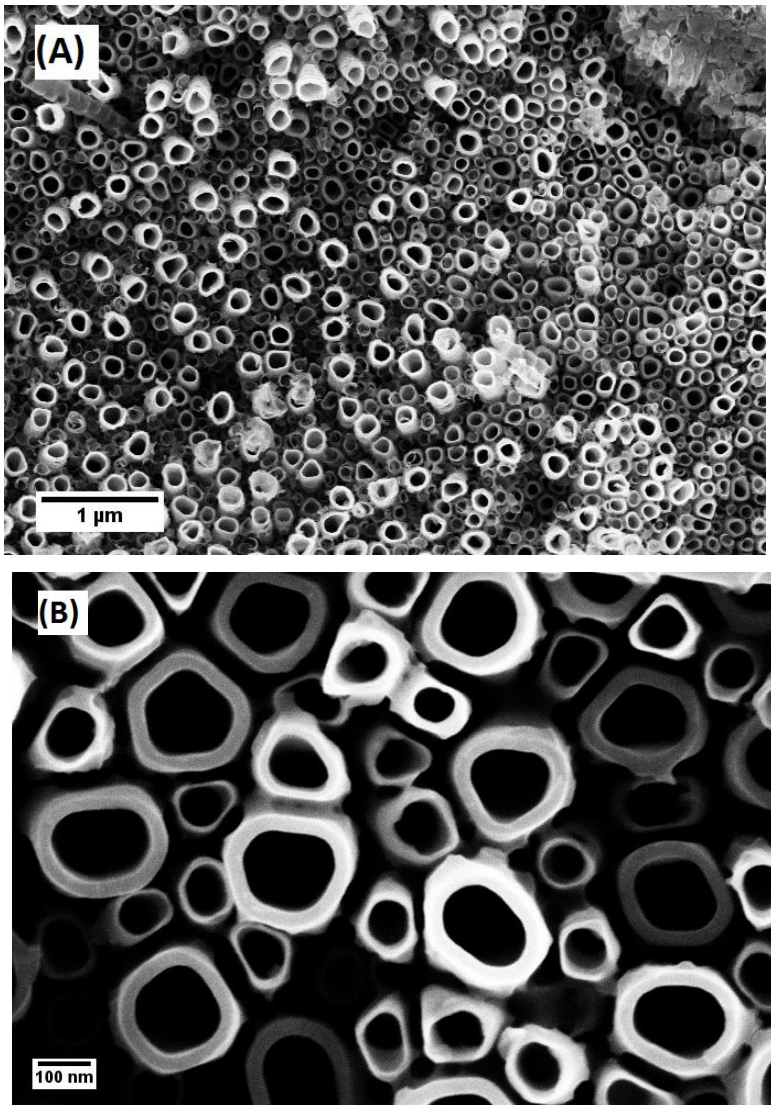

Figure 4.14: Top view FESEM images of as-anodized Ti-17Nb-6Ta sheets using aqueous AD4 electrolyte. (A) and (B) show the heterogeneous NTs dimensions at low and high magnification, respectively.

4.2. Structural and compositional Characterization

Composition and crystallinity of the as-fabricated Ti-17Nb-6Ta samples were first examined using X-ray diffraction (XRD) and Raman spectroscopy on annealed sample at 450 ° C. Figure 4.15, evidently confirms the crystallization of the nanotubes in the anatase phase, with appearance of peaks corresponding to (101), (103), (004), (112), (200), (105), (211), (213) and (220) facets. These peaks are normally indicative of titania NTs anatase phase as reported in literature [173–176]. However, absence or existence of the other alloy components, i.e. Nb and Ta, cannot be confirmed nor denied from these results. It was reported that both Nb and Ta existence with titania may not alter greatly nor postpone its phase transformation from amorphous to anatase [177–179]. Results from Ti-xNb, Ti-xTa- xZr and Ti-xTa annealed samples at 450 ° C revealed the same peaks' positions reported with anatase phase of titania NTs. This indicates possible overlapping of peaks from the three components [180–182].

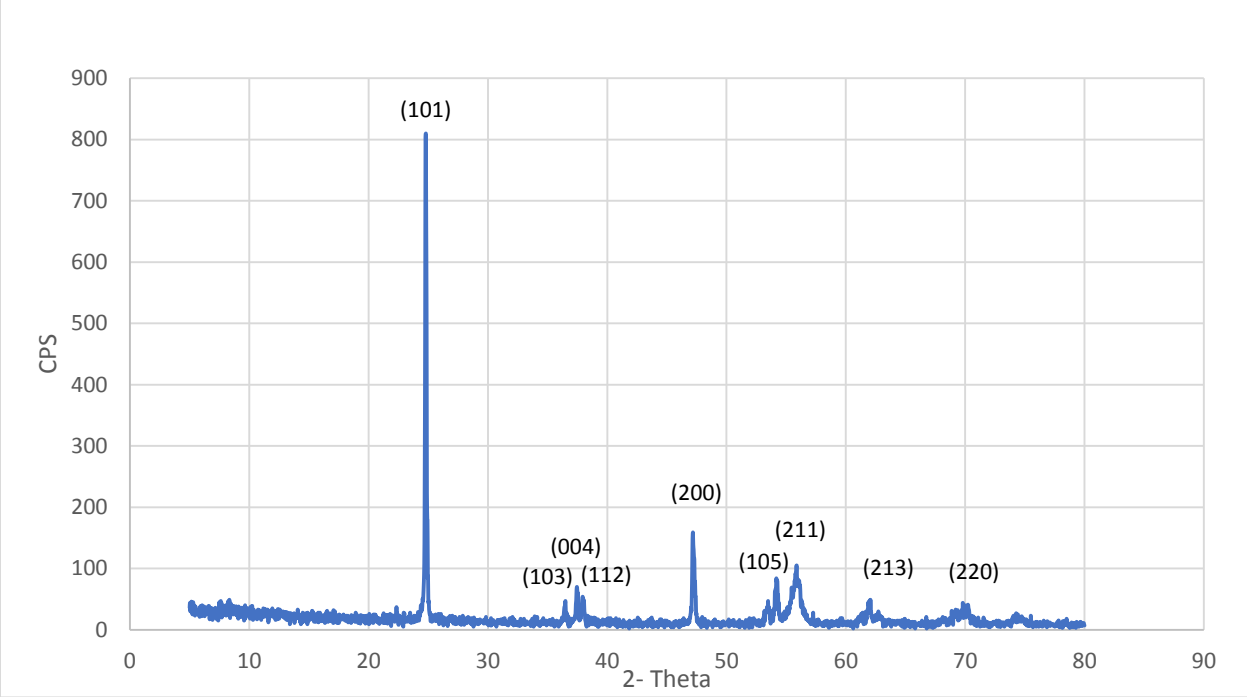

Figure 4.15: X-ray diffraction pattern of as-fabricated Ti-17Nb-6Ta NTs, annealed at 450 ° C for 3 hours.

Results from XRD was supported by Raman spectra, as shown in Figure 4.16. It indicated the tetragonal vibration mode symmetries associated with anatase, of peaks corresponding to E_g, E_g, B_{1g} and A_{1g} modes [174,175]. However, slight shift and broadening of some peaks may be indicative of presence of other elements in the crystal [183]. Yet, no distinctive peaks were revealed for Nb or Ta for confirmation. Accordingly, this could not be considered accurate analysis for surface composition.

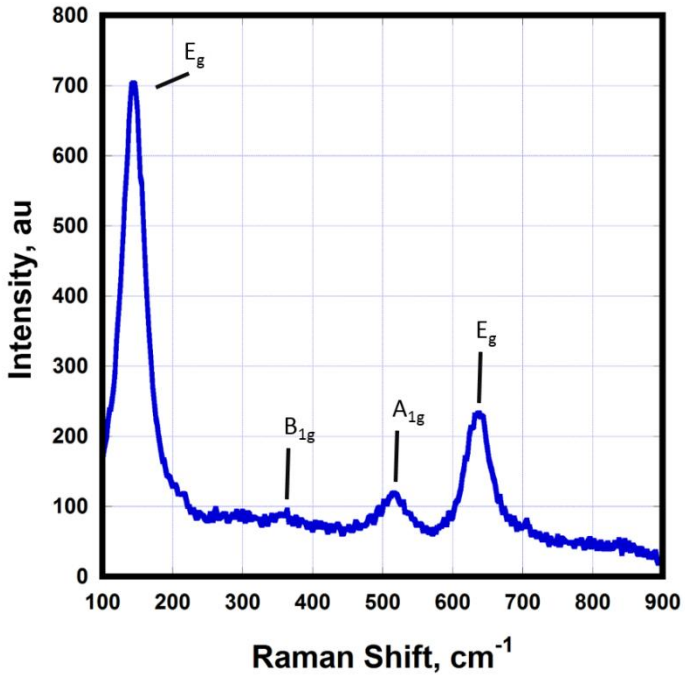

Figure 4.16: Raman spectrum of the fabricated Ti-17Nb-6Ta NTs, annealed at 450 ^{o} C for 3 hours.

More sensitive and accurate technique was, therefore, needed for confirming or denying the formation of mixed oxides on the as anodized surface. The three alloying elements have different activities towards etching and evidence was then needed to make sure the three elements were retained during anodization and within the NTs. Accordingly, X-ray Photoelectron Spectroscopy (XPS) was used, which results in fingerprint elemental analysis. XPS is considered a powerful tool for identifying the surface components, chemical composition and oxidation degrees. Spectra for as anodized Ti-17Nb-6Ta samples, indicated the presence of Ti, Nb, Ta, and O elements, and confirmed the formation of Ti-Nb-Ta mixed oxides, as illustrated in Figure 4.17.

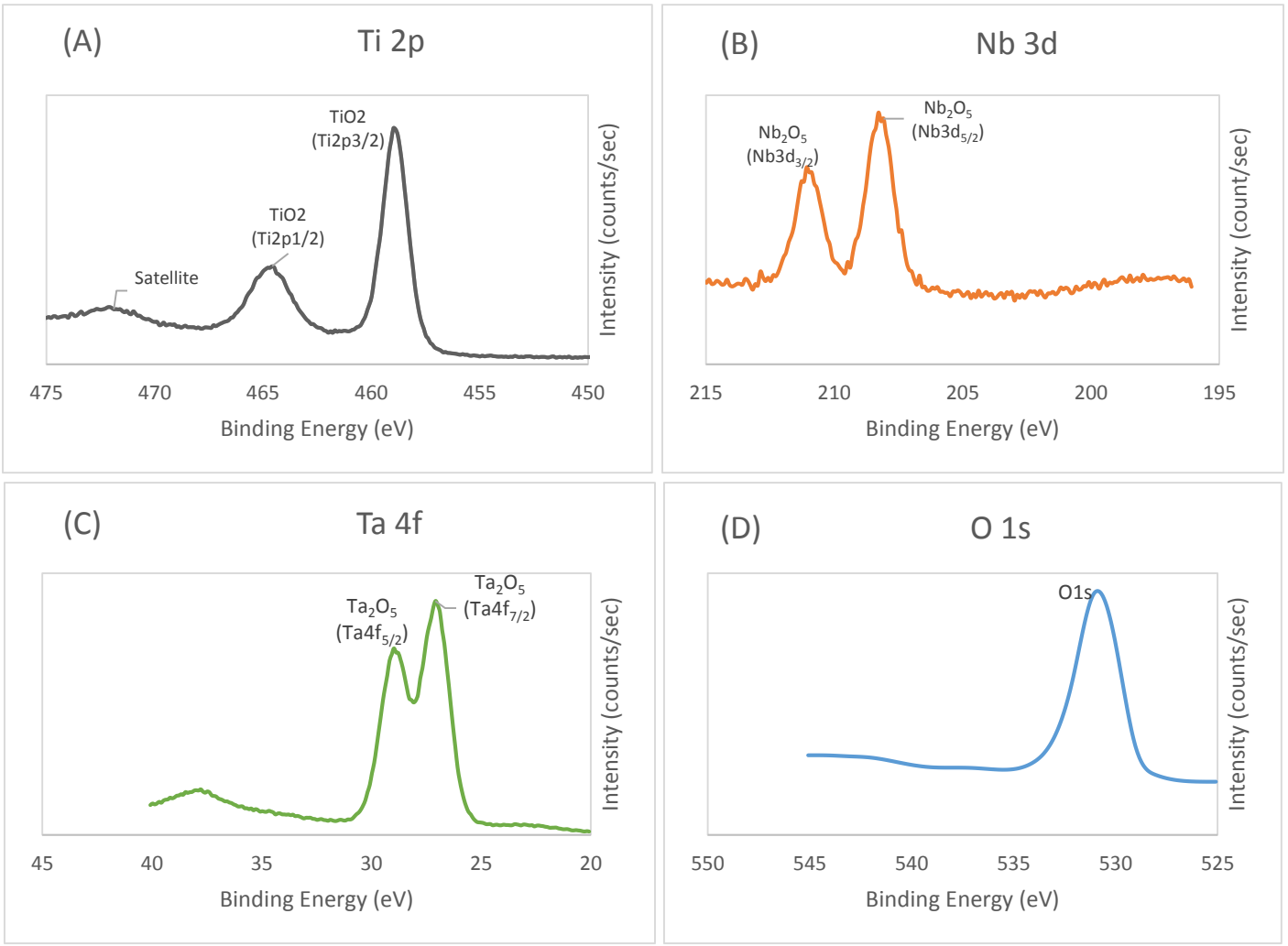

Figure 4.17: XPS spectra of the (A) Ti 2p, (B) Nb 3d, (C) Ta 4f and (D) O 1s emission peaks for Ti-17Nb-6Ta as-anodized formed nanotubes.

Figure 4.17 shows the XPS spectra for the alloy. Figure 4.17 (A) shows two peaks that can be assigned to Ti $2p_{1/2}$ and Ti $2p_{3/2}$. The peaks are located at 464.6 eV and 458.7 eV with spin orbit splitting (Δ) = 5.9 eV associated with Ti^{4+} [(1)]. Figure 4.17 (B) revealed Nb3d doublet at 210.98 eV and 208.08 eV associated with Nb $3d_{3/2}$ and Nb $3d_{5/2}$. It showed spin orbit splitting (Δ) = 2.9 eV, confirming that signals correspond to Nb^{5+} [(2)]. In Figure 4.17 (C), peaks appeared at 29.08 eV for $Ta4f_{5/2}$ and 27.18 eV for $Ta4f_{7/2}$. Spin orbit splitting (Δ) was found to be equal 1.9 eV confirming presence of Ta^{5+}. Finally, Figure 4.17 (D) shows Oxygen indicative peak O1s, with only single peak is observed located at 530.98 eV.

These results were supported by Energy dispersive X-ray spectroscopy (EDX) as a qualitative elemental analysis technique. As observed from Figure 4.18, EDX showed that the surface formed of NTs were composed of Ti, Nb, Ta and O. Overall composition was found to be relatively consistent with the composition of the substrate forming alloy, yet Ta content is slightly higher than expected. This, however, confirms that compositions of NTs depend upon titanium alloy elemental composition.

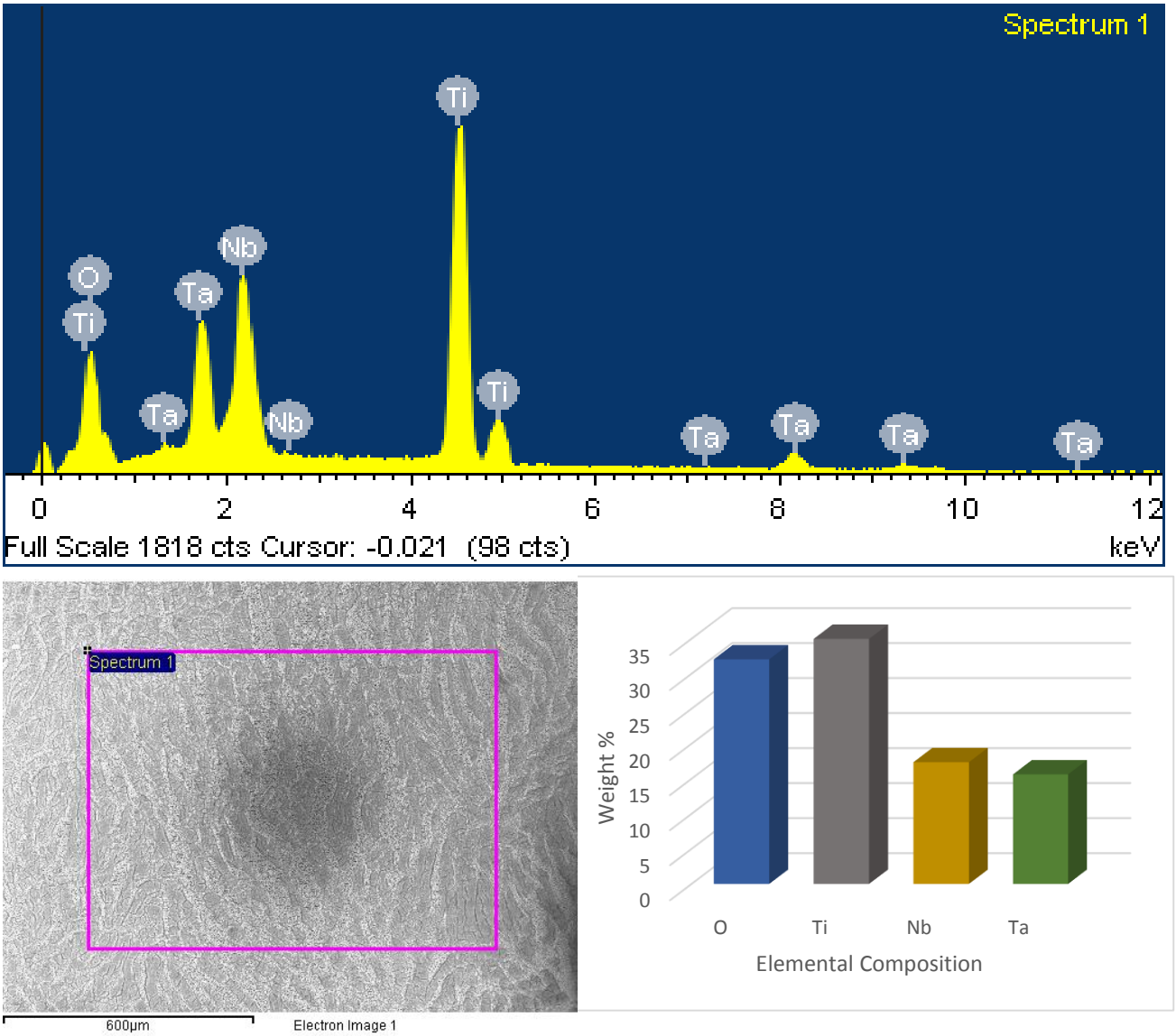

Figure 4.18: EDX peaks and composition of Ti-17Nb-6Ta-1O formed nanotubes, analysed within the specified spectrum

4.3. Nanomechanical Characterization

Not only that material mechanical properties are critical for drug eluting stents, but also biological interaction with material surfaces is sensitive to mechanical properties at the interface. Surface stiffness was found to significantly influence cells fate [57,184].The mechanical properties of the fabricated nanoarchitectures were measured using nanoindentation technique. Nanoindentation tip was used to obtain Young's modulus (a measure of stiffness) and hardness values, before and after annealing. During loading and unloading, hysteresis loop was observed, which indicated that NTs surface has elastic energy dissipation, as seen in Figure 4.19. It can be observed from the curves below, that elastic recovery is higher for annealed sample (Figure 4.19 (B) and (D)) reference to their unannealed counterpart. Also, unloading slope of annealed samples are found to be steeper indicating higher stiffness.

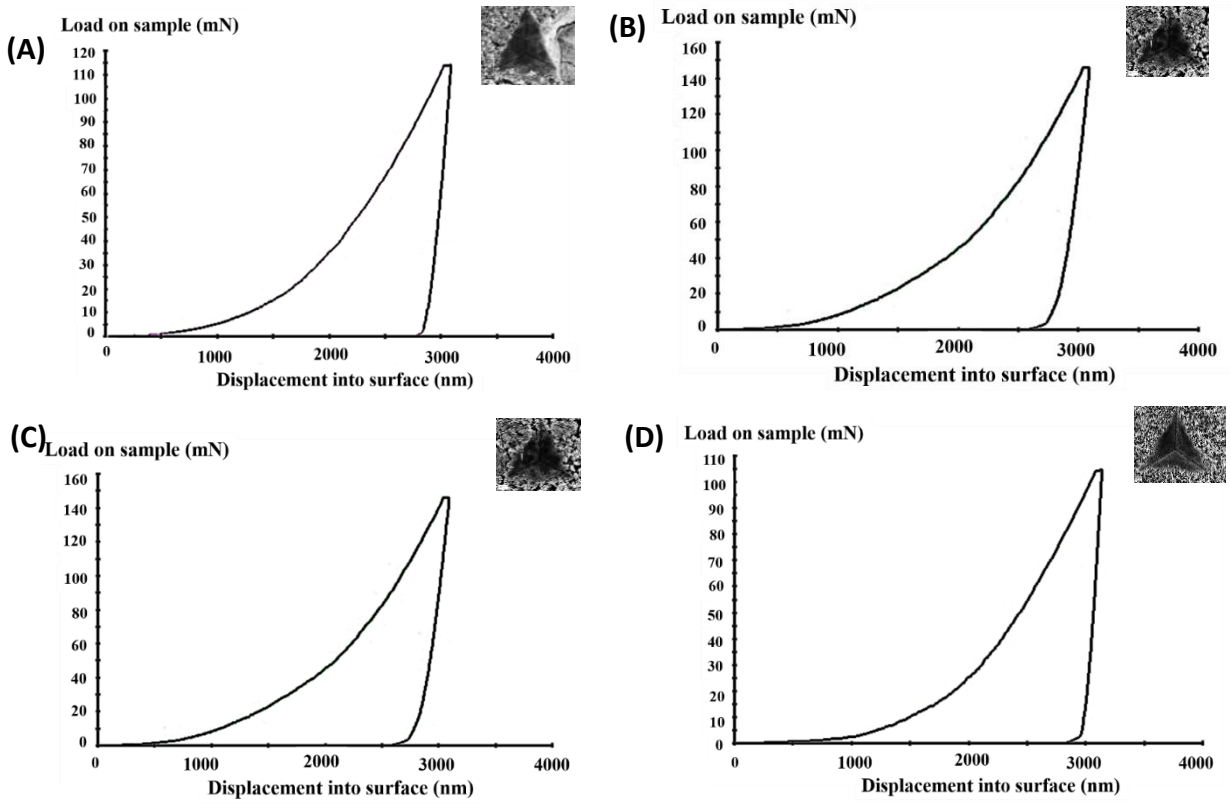

Figure 4.19: Average load-displacement curves from nanoindentation of (A), (B) Homo-NTs and (C), (D) Hetero-NTS, before and after annealing respectively.

From inspecting Figure 4.19, total depth of indentation is much smaller than the NTs layer thickness (12 µm). Accordingly, insights on NTs plastic deformation behavior can be gained without interference from substrate material. Young's modulus and hardness average values were calculated and compared for Homo-NTs and Hetero-NTs before and after annealing, as shown in Figure 4.20. It was found that both Young's modulus and hardness increase with annealing for both Homo- and Hetero-NTs, which can be explained by phase transformation upon annealing. For hardness, Homo-NTs were found to be superior. For Young's modulus, Homo-NTs showed lower values, which does not indicate inferiority within intended application.

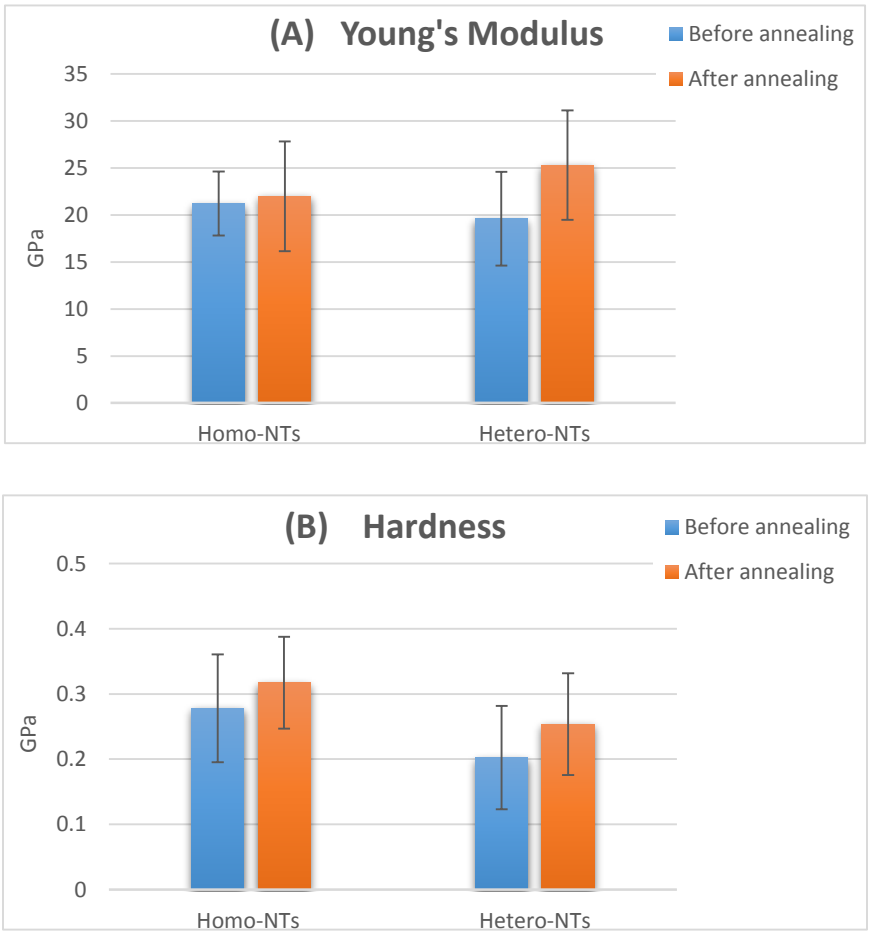

Figure 4.20: Young's modulus and hardness values for Homo- and Hetero-NTs, before and after annealing.

4.4. Influence of Nanoarchitecture Surface Morphology on Biological Response

4.4.1. Cytotoxicity Measurements

As any biomaterial that will be in contact with biological components, assessment of the material's cytotoxicity is crucial to be considered in biomedical applications. This is a mandatory step before considering any in-depth proliferation studies. For Ti-17Nb-6Ta alloy, samples were assessed to ensure not only the safety of the alloy material, but also the effect of the used electrolytes in nanotubes fabrication on materials biocompatibility.

As described in chapter 4, MTT assay was used to assess cytotoxicity for 3 samples' surfaces: 1) Ti-17Nb-6Ta sheets as received, 2) with Homo-NTs and 3) Hetero-NTs structures. Each sample's extract were tested through 3 different dilutions, each repeated eight times for results reproducibility. According to plate design illustrated in chapter 3, microplate reader absorbance results were retrieved as described in Table, 4.1 below. Also readings for blank and cell control were recorded for percentage of cells viability calculations.

Table 4.1: Absorbance results of MTT assay for Ti-17Nb-6Ta samples; as received substrate and the two different nanotubes morphologies fabricated and reported earlier.

	Blank	C. control	Homo-NTs			Hetero-NTs			Alloy substrate			
	1	2	3	4	5	6	7	8	9	10	11	12
A	0.006	0.421	0.422	0.423	0.42	0.423	0.422	0.423	0.421	0.424	0.423	
B	0.007	0.422	0.424	0.421	0.422	0.424	0.421	0.422	0.42	0.421	0.422	
C	0.004	0.423	0.425	0.425	0.423	0.42	0.424	0.423	0.421	0.423	0.422	
D	0.006	0.424	0.423	0.424	0.421	0.422	0.424	0.422	0.424	0.421	0.423	
E	0.005	0.421	0.42	0.422	0.424	0.423	0.421	0.424	0.424	0.422	0.424	
F	0.006	0.423	0.421	0.423	0.423	0.423	0.421	0.422	0.421	0.422	0.421	
G	0.003	0.421	0.421	0.42	0.422	0.423	0.422	0.423	0.421	0.42	0.421	
H	0.006	0.423	0.424	0.422	0.425	0.421	0.423	0.421	0.421	0.424	0.423	

From absorbance reported data, percentage of cell viability for different samples' extract were calculated using the following equation and presented in Figure 4.21:

$$Survival\ rate\ \% = \frac{A\ sample - A_b}{A_c - A_b} \times 100 \qquad (4.1)$$

where A_c is the negative control and A_b is blank.

Figure 4.21. Illustrates the percentage of cells survival rate or cell viability for 1) Ti-17Nb-6Ta sheets with as anodized Homo-NTs, 2) with Hetero-NTs structures, and 3) as received substrate material measured by MTT assay. Data present 3 different dilutions for each sample's extract (0, -1, -2). It can be clearly seen that cells survival rate is about 100% for all samples and different dilutions. This indicates almost no cytotoxicity at all for the substrate alloy material used. It is also clear that results from NTs fabricated using different electrolytes (FG3 for Homo-NTs and AD4 for Hetero-NTs) are as promising as the substrate material. This exclude any possible cytotoxicity from electrolyte after sample cleaning post anodization.

These results are highly consistent with the biocompatibility and hemocomatability reports in literature for Titanium and Titanium alloys [185,186].Such high degree of biocompatibility is attributed to the ability of Ti-based alloys to form a stable oxide layer in most environments. Furthermore, the thicker and more stable oxide layer, the better is the material bioactivity. This has driven earlier attempts to increase biocompatibility and activity of material surfaces by increasing oxide layer through anodization techniques [187-190].

For Drug eluting stents (DES) application, material stability and cytotoxicity are considered crucial. The use of materials with any inflammatory effect can cause local tissue sensitization, which can directly affect the healing process as well as the local thrombogenicity.

In this work, NTs are proposed as platform for enhancing endothelial tissue regeneration as well as to act as drug carriers. Accordingly, it is proposed to replace polymer coating on stents struts, which leaves Ti-17Nb-6Ta substrate and NTs in direct contact with biological components. This confirms the significance of % cells viability results obtained for the material under study. From results reported in Figure 4.21, Ti-17Nb-6Ta can be potential material for DES and can be considered for further in-depth investigation regarding proliferation studies.

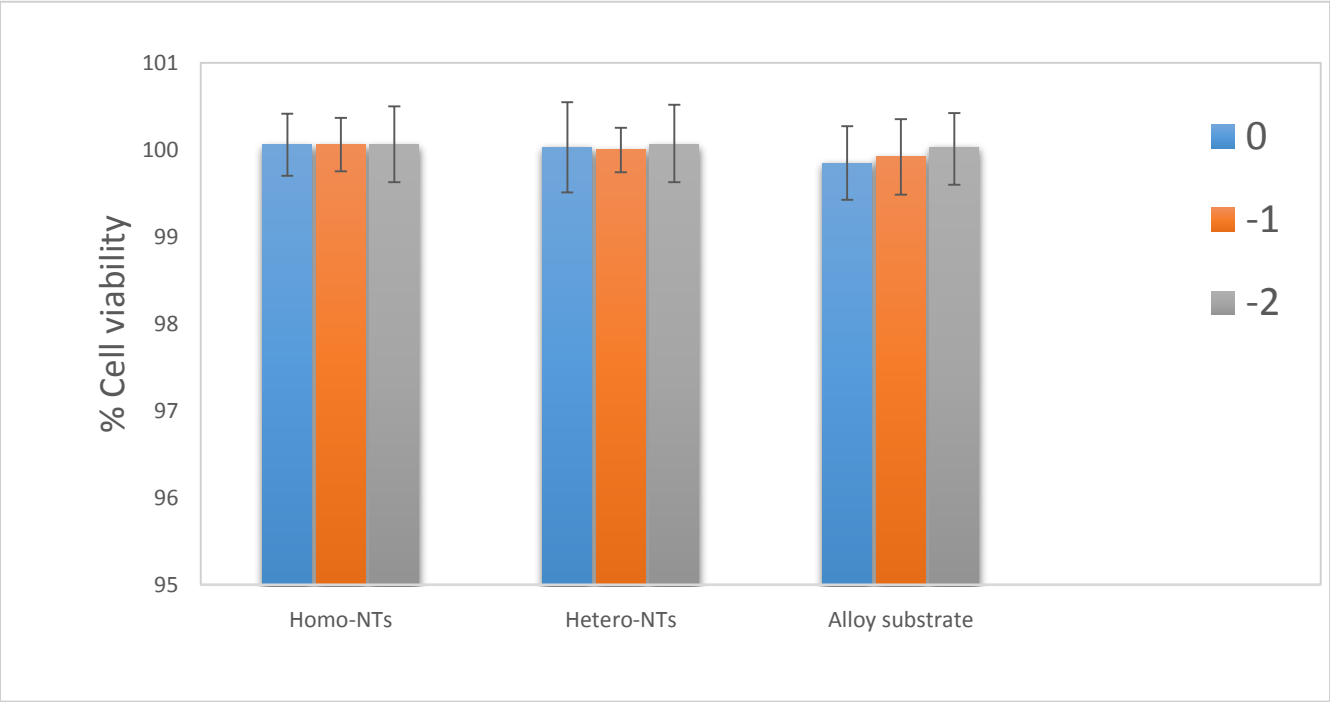

Figure 4.21: Mean values of percentage of cell viability for 1) Ti-17Nb-6Ta sheets with Homo-NTs, 2) with Hetero-NTs structures and as received substrate. It is illustrated for each sample, values for three different dilutions (0, -1, -2) of tested samples extracts.

4.4.2. Activation of Endothelial Cells Growth on Ti-based Nanoarchitectures

Ultimate vascular conditions post percutaneous coronary angioplasty and stenting can be described as fast controlled healing of endothelial cells. Endothelial cells regeneration at site of injury would directly enhance patient prognosis and stenting outcomes. As the inner most lining of the blood vessel, intact endothelial cells can prevent thrombus formation as well as avoid neointimal hyperplasia. This would allow the need of lower doses of local cytotoxic drugs and more importantly would decrease the duration of oral antiplatelet therapy required for the patients.

As reported in chapter 2, nanoarchitectures supported the migration, adhesion and proliferation of mesenchymal stem cells and endothelial cells. Different biological response was studied and reported for samples of different NTs diameters [109, 139-141]. In this work, the influence of nanoarchitecture of as anodized Ti-17Nb-6Ta was studied versus smooth substrate surface of the same material. Furthermore, the effect of another morphology related factor on cells activation was investigated. This factor involved NTs dimensional homogeneity, by comparing endothelial cells proliferation on Homo-NTs prepared by FG3 electrolyte conditions versus Hetero-NTs prepared by AD4 electrolyte conditions.

This section reports studies of endothelial cells proliferation for 3 types of Ti-17Nb-6Ta samples; 1) Smooth surface of as received alloy, 2) Homo-NTs and 3) Hetero-NTs. Proliferation results were reported using 3 different studies:

- Cell counts from Tryptan blue cells viability assay.
- MTT cells viability assay using absorbance data as an indicative measure.
- Visual observation by imaging under FESEM.

4.4.2.1. Trypan Blue Cells Viability Assay

The three different samples underwent tryptan blue viability assay, and for each sample both dead and viable cells were counted under the microscope at specific time intervals of 1, 3 and 7 days. Counted viable cells of the three samples are illustrated and compared below at the specified time intervals, as shown in Figure 4.22.

It is evident from the graphical representation in Figure 4.22 that nanoarchitectures directed better proliferation of endothelial cells than smooth surface of material substrate at the three studied time intervals. This directly supports the proposed hypothesis that surface modification of drug eluting stents with nanotopography would guide faster endothelial healing. Therefore, replacing the DES polymeric coating with NTs can be of great potential towards better stenting outcome in terms of biological response. This shall not only spare the local inflammation that may be caused by used polymer, but also promote endothelial tissue proper healing.

Furthermore, the effect of changing surface topographies through differently anodized samples were compared. Homo-NTs clearly showed higher number of counted cells than Hetero-NTS, indicating better proliferation. This signifies the importance of NTs optimization in terms of dimensional homogeneity, which should be considered for the applications involving tissue regeneration. During endothelialization, nanoarchitectures mimic temporarily extracellular matrix (ECM) guiding and nurturing cells growth [113, 191]. Superior outcome from Homo-NTs may be attributed to better distribution of ions, proteins and nutrients required for the growth, as well as more structured spatial guidance of cells to grow.

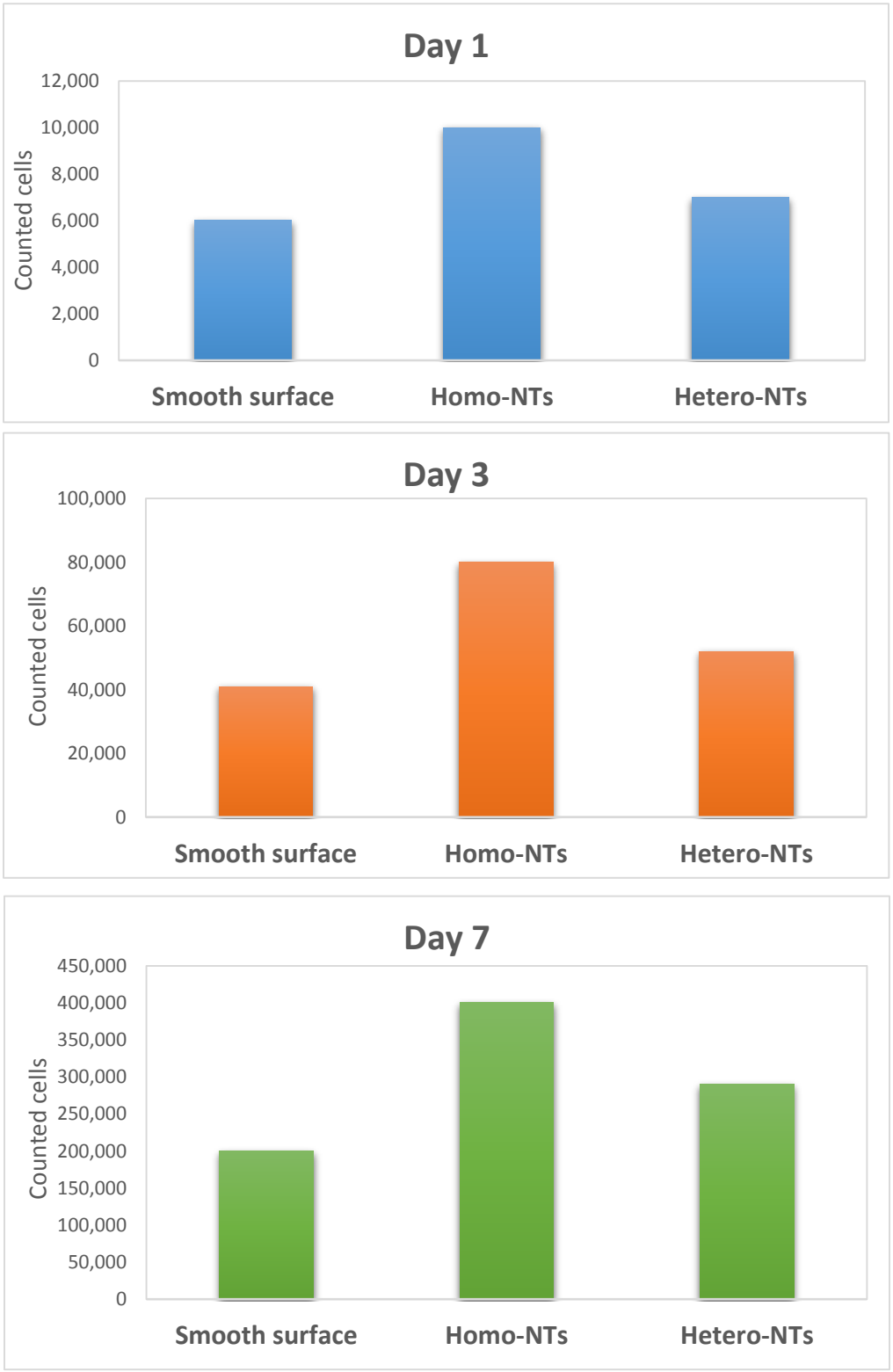

Figure 4.22: Viable endothelial cells count on 1) Ti-17Nb-6Ta smooth surface 2) with Homo-NTs, 3) with Hetero-NTs structures at different time intervals (1, 3 and 7 days)

4.4.2.2. MTT Assay:

For confirming trypan blue assay results, MTT assay was conducted for the same 3 types of samples of Ti-17Nb-6Ta; 1) Smooth surface of as received alloy, 2) Homo-NTs and 3) Hetero-NTs. Absorbance of Formazan solutions was reported as a reflection of viable cells concentration per sample. Reading were accordingly compared, as shown in Figure 4.23. Better outcome with nanoarchitecture was confirmed versus smooth surface. Also, Homo-NTs showed the same trend reported with trypan blue assay as the superior morphology for proliferation among the three samples.

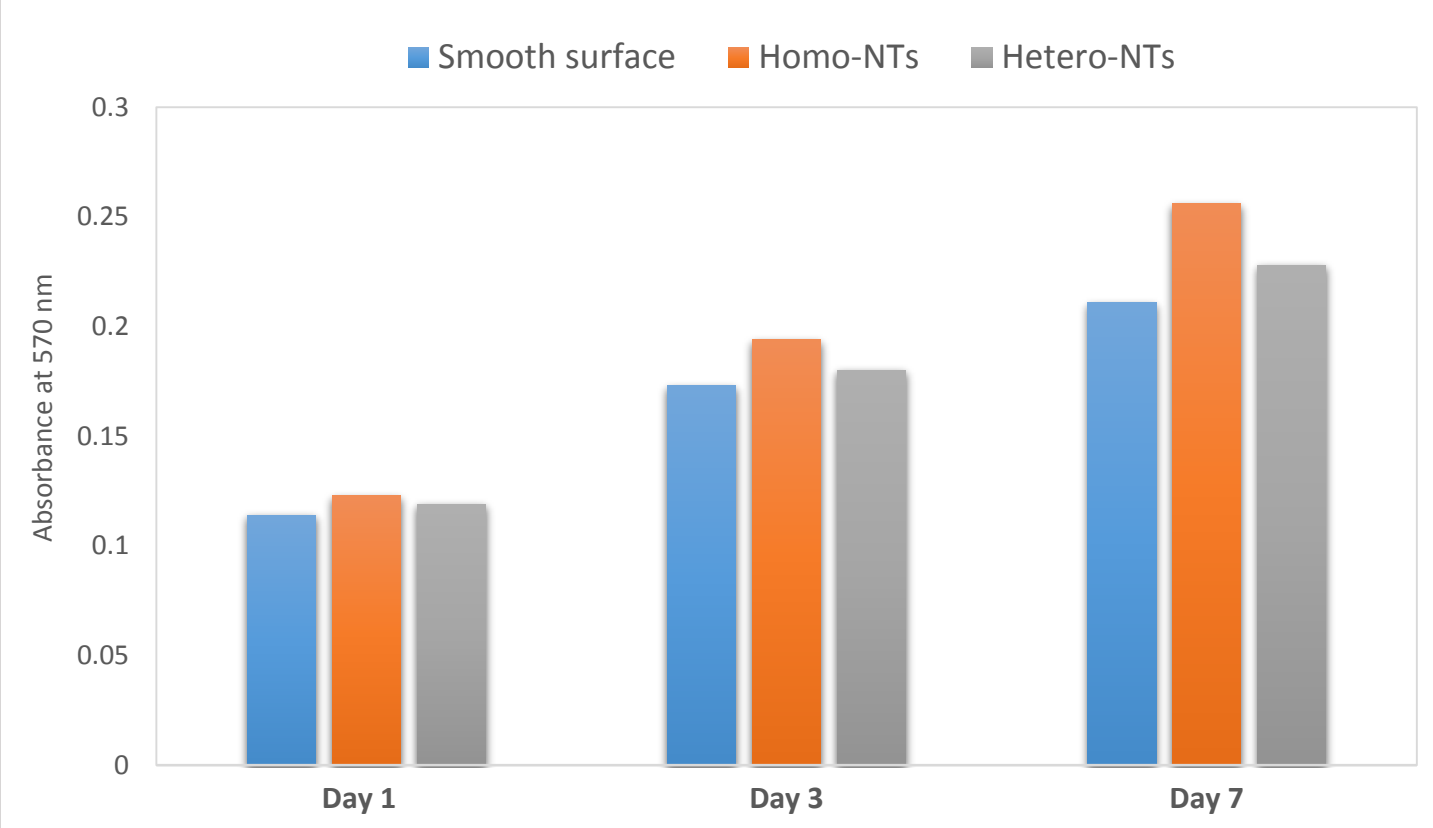

Figure 4.23: Formazan absorbance from MTT cell viability assay for: 1) Ti-17Nb-6Ta smooth surface 2) with Homo-NTs, 3) with Hetero-NTs structures at different time intervals (1, 3 and 7 days)

4.4.2.3. FESEM Imaging of Cells Proliferation

Endothelial cells were grown on the surface of Homo-NTs and Hetero-NTs for 3 days to confirm the effect of dimensional homogeneity on cells' proliferation. Cells were fixed and imaged using FESEM, as shown in Figure 4.24. Cells morphology and degree of proliferation shown in Figure 4.24, confirm the superiority of Homo-NTs in guiding endothelialization over Hetero-NTs.

Images (A),(C) and (E) on the left side of Figure 4.24, represents cells' growth on Homo-NTs, where the island like structure of highly ordered nanotubes can be seen at the highest magnification (E). While, images (B), (D) and (F) on the right side of the figure illustrates cells on Hetero-NTs, and as well at highest magnification (F) NTs with different diameters can be observed.

Elongated endothelial cells are predominantly seen on Homo-NTs. On the same morphology cells are more distributed and almost forming network like structure. Also, cells show more pronounced filopodia protrusions. This indicates better cells migration and proliferation more on the homogeneous structure of NTs, which would directly results in higher cells count as seen in the former assays. Cells cultured on Hetero-NTs, on the other hand, showed more rounded structure, less spread on the surface and not yet crossing into a network. This indicates potential of slower healing rates for Hetero-NTs in applications.

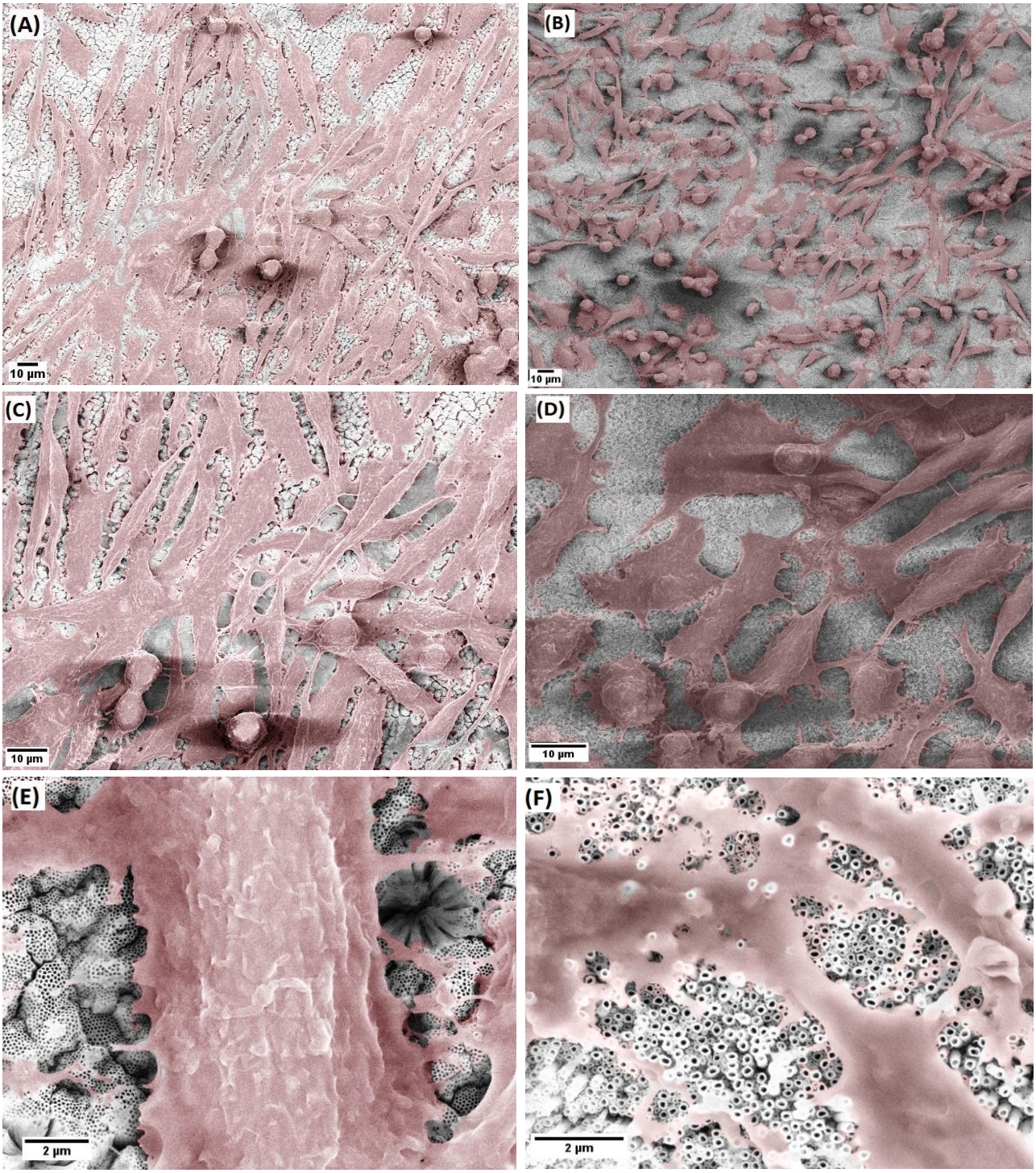

Figure 4.24: Top view FESEM images of endothelial cells grown on NTs surfaces after 3 days. (A), (C) and (E) are cells grown on Homo-NTs at different magnification. (B), (D) and (F) are cells grown on Hetero-NTs at different magnification.

4.5. Ti-based Nanoarchitectures as Drug Reservoir

4.5.1. Drug Loading

Work reported in this section was intended to evaluate the potential use of the fabricated nanoarchitectures as drug reservoir. This is a critical feature for any material to be proposed as a platform for DES surface modification. As polymer coatings replacement, Ti-based NTs are intended to locally deliver any of drug classes used to avoid neointimal hyperplasia. The proposed platform is intended to deliver the drug only into the vascular tissue side and not the vessel lumen. Accordingly, anodized samples were tested for drug loading only on one side of the sheet covered with the NTs layer, to avoid interference or duplication of results from the other NTs layer.

Concentration of loaded drug in 1 cm^2 NTs layer was calculated, using the calibration curve described in chapter 3. This was done for both Homo-NTs and Hetero-NTs of 12 µm length. Amount of loaded drugs were calculated and plotted, as shown in Figure 4.25.

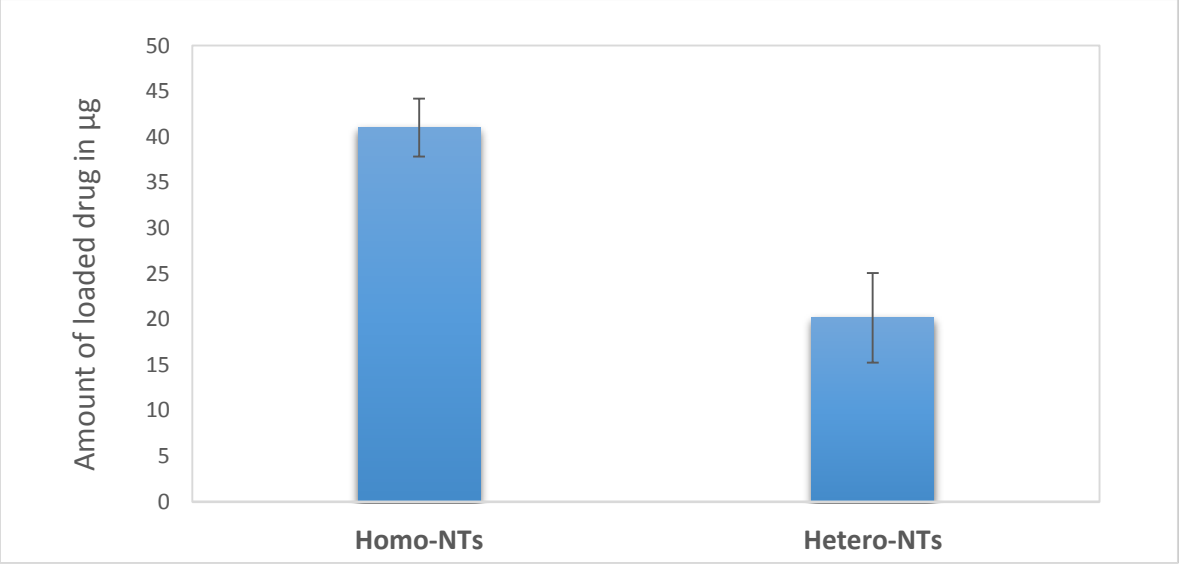

Figure 4.25: Comparison between drug loading capacity of Homo-NTs and Hetero-NTs.

Results were compared between the two NTs morphologies to assess system superiority. It is evident from Figure 4.25 that Homo-NTs drug loading capacity is almost double Hetero-NTs. This can be explained by grooves found with Homo-NTs between islands of compact nanotubes, see Figure 4.26. These grooves can reach width of up to 1 µm. Accordingly, they can act as potential reservoir for higher amounts of drug causing this gap between both platforms. As described, Homo-NTs showed more promising results for both biological response as well as drug loading. Accordingly, it was further studied for its drug release profile using computational analysis.

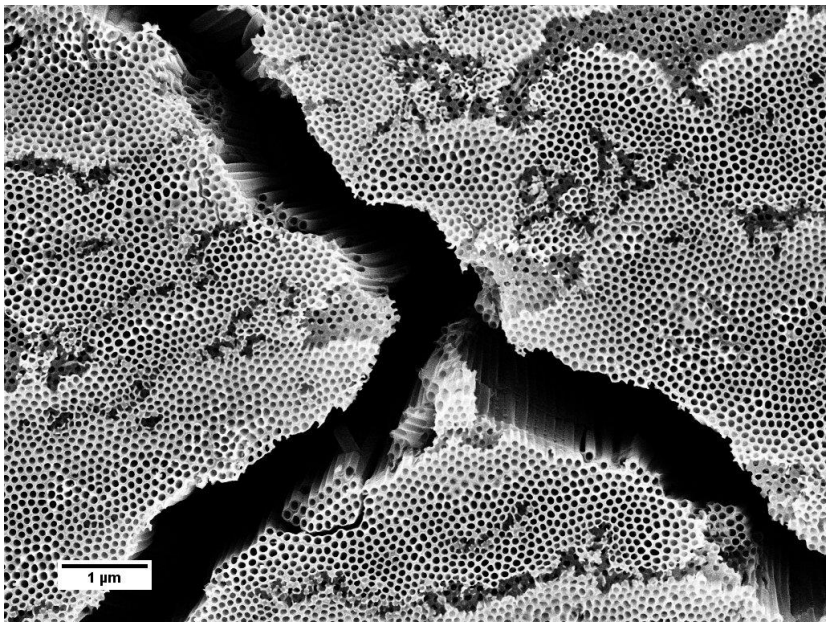

Figure 4.26: FESEM image, top view of Homo-NTs, showing grooves between compact NTs islands

4.5.2. Drug Release by Computational Simulation

In this work, a simulated model was used to examine and describe the release profile of 2'- deoxyadenosine from Homo-NTs. "Transport of diluted species" module was used for the simulation. As concluded from previously reported biological response and drug loading for the two NTs morphologies, results came in favour of Homo-NTs. Accordingly, release behaviour was furthermore predicted for the practically loaded amount of drug from Homo-NTs. In order to simulate the system, the physical model was first defined to identify model's geometry, system parameters, boundary's conditions and equations that would govern the simulation.

Figure 4.27 facilitates the description of the system's physical model. The figure shows a cross section of the vessel at the healthy state (on the left) and after stenting (on the right). With healthy vessels, wall tissue is still intact and demonstrating the three layers building the wall; 1) innermost "Intima" (endothelium lining followed by connective tissue), 2) the middle layer "Media" (composed of smooth muscles) and 3) The connective tissue of the outer layer "Adventitia". However, after stenting, metal struts are embedded into the intima with direct contact with the connective tissue, while endothelium is almost damaged. Stent is taking the shape of a ring, spanning the entire vessel circumference. Atherosclerotic plaque is hypothetically considered to be totally removed during PTCA.

By magnifying at stent-tissue interface, the NTs delivery system is illustrated. Homo-NTs are grown vertically on Ti-alloy substrate, which is embedded in the vessel wall tissue. Drug release is intended to be in the direction of vessel wall only, hence not affected by the central blood flow in the vessel lumen. Therefore, mass transport in the model was identified to be dominated by diffusion and excluded both convection and migration. Accordingly, equation that governed the drug motion was set to be of Fick's law:

$$\frac{\partial \mathrm{c}i}{\partial \mathrm{t}} = \mathbf{D}_i \,.\, \nabla^2 \, \mathbf{c}_i \qquad (4.2)$$

where for species i, $\mathbf{D}_i$ = the diffusion coefficient (m^2 /s), and $\mathbf{c}_i$ = the concentration (mol /m^3).

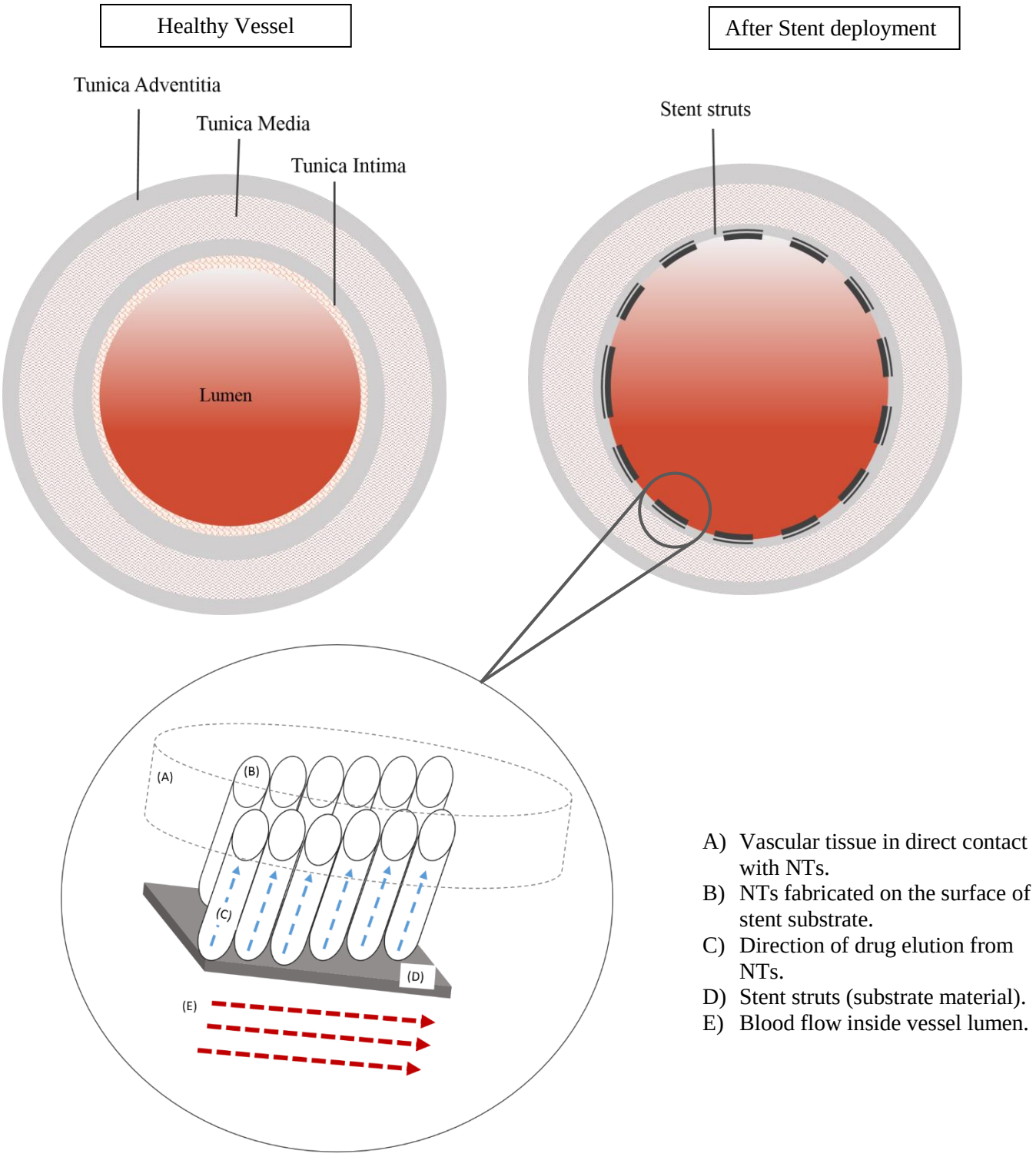

Figure 4.27: Illustration of physical model representing the NTs drug delivery system into vessel's tissue. The Figure is just diagrammatic representation, not representing actual relative dimensions of the system components.

Drug release was assumed to be restricted to the surrounding tissue moving across the connective tissue of Intima layer – as endothelium lining is damaged – and into the Media. Boundary conditions were therefore described to restrict the flux within that system and indicate that flux outside its boundaries is equal to zero (n. $\mathbf{N}_i = 0$). Accordingly, the model geometry was built as shown in Figure 4.28 with 2D spatial dimension, comprising the modeling domains within the system boundaries; the NTs, Intima layer (excluded damaged endothelium and Media layer.

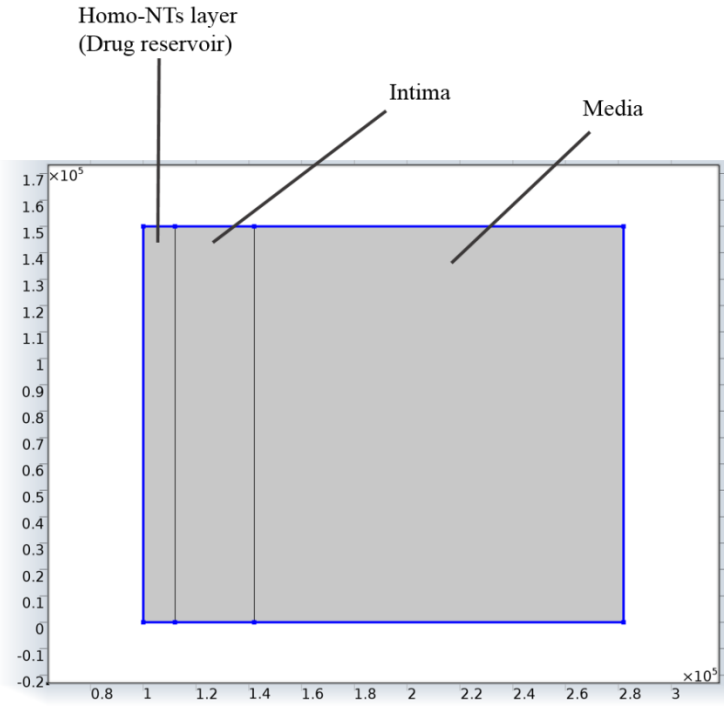

Figure 4.28: 2D geometry of the modeling domains for drug release from NTs.

Simulation parameters were identified reference to the previously reported practical results. Dimensions of Homo-NTs were about 75 nm in diameter and 12 µm in length, as fabricated by FG3 electrolyte conditions. Initial drug concentration in the NTs was 0.001671 mol/m^3, which was loaded within 36 hours in static conditions. Materials of the model domain were identified according to their diffusion coefficient (D_c). For Intima, D_c is = 5.4×10^{-12} m^2/sec and for Media D_c is = 5.0×10^{-14} m^2/sec [192]. This difference in D can directly affect the

drug elution as diffusion coefficient can be the rate limiting step for mass transport across the system. Diffusion coefficient of the drug in the NTs was calculated using the following equation [193]:

$$\sqrt{\frac{M_t}{M_o \times 2}} = \frac{Dt}{\pi h^2} \tag{4.3}$$

where M_t is equal to the amount of drug released at time t, M_o is equal to the initial drug amount and h is the layer thickness.

These values were retrieved from practical data measured for the same drug by Kang, et al [138]. Calculated value of drug diffusion coefficient was found to be = 2.5×10^{-11} m^2/sec. Using the aforementioned parameters, time dependant study was designed for the drug release profile. Concentration distribution of the drug was simulated as a function of time across the NTs and the wall tissue (Intima and Media). Figure 4.29 shows drug concentration across the modeling domains, using the 2D geometry and its 3D representation by axial symmetry at the end of the simulation (3 days). Darkest red area represents the higher drug concentration, while darkest blue represents the lower concentrations.

Time dependant estimation of drug released was used to plot drug concentration in NTs over time. As seen in Figure 4.30, almost 100% of the initial drug amount was released after 3 days. For DES, this rate can be considered faster than required, reference to polymeric coating drug release over duration of one month. This may need more control over the system by for example any of the strategies mentioned in chapter 2, such as polymeric coatings over NTs pores, using drug carriers or external fields [140].

(A)

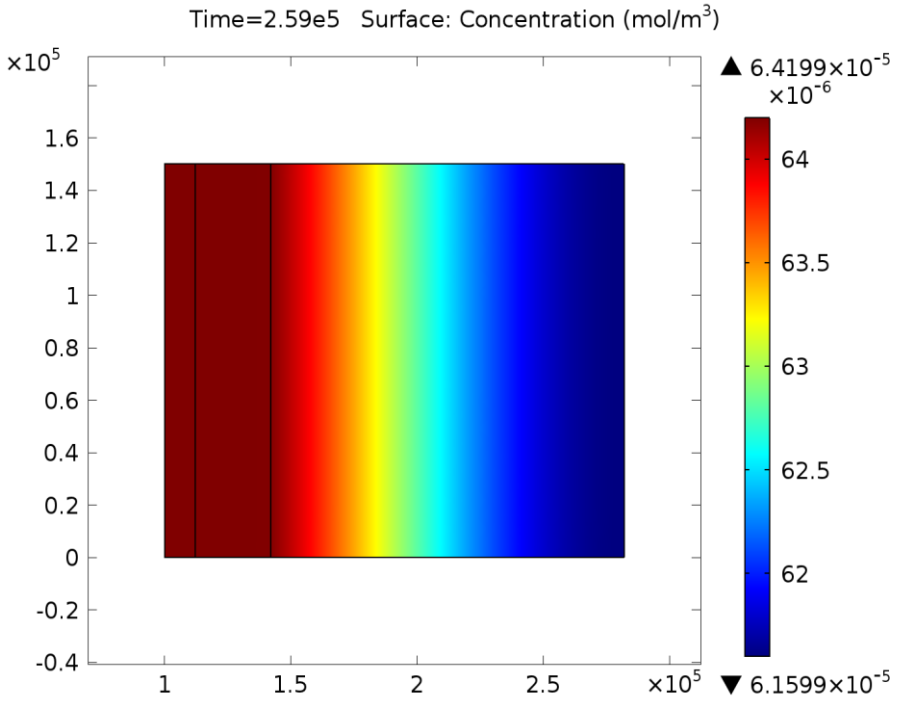

(B)

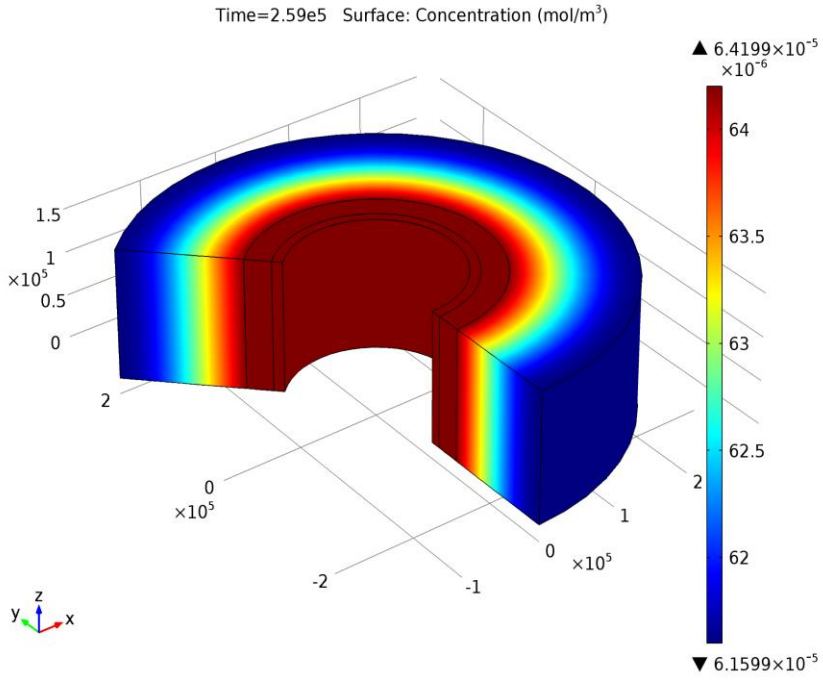

Figure 4.29: Drug concentration over the modeling domain with A) 2D and B) 3D geometry at the end of simulation (3 days).

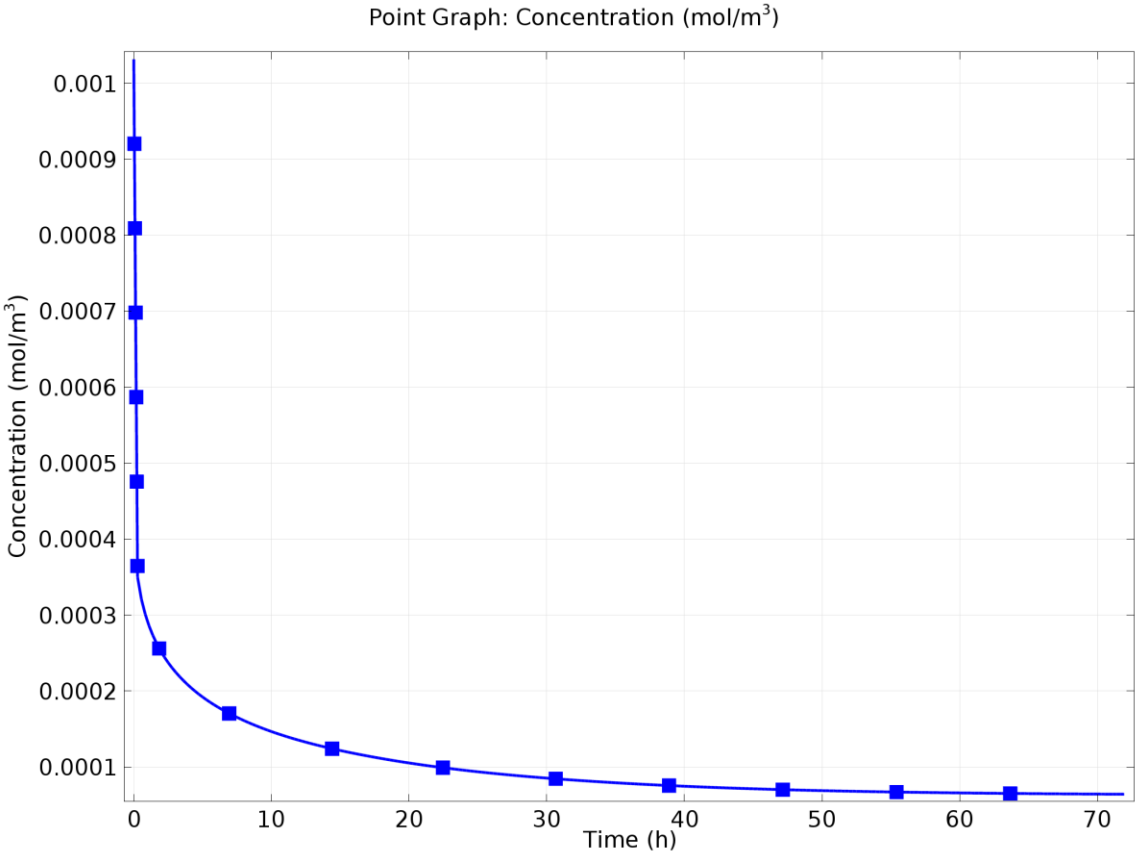

Figure 4.30: Calculated drug concentration in the NTs over time

However, other factors may have resulted in such relatively fast rate other than the inherent properties of the NTs system. This may include the initial amount of loaded drug. It is assumed that drug loading may increase by increasing the initially added drug and the techniques used for loading other than static solutions. This may not only increase the total amount of drug released but also decrease the elution rate. Also, the nature of the drug is a critical factor in such context. The tested drug (2'- deoxyadenosine) is hydrophilic with higher diffusion coefficient than hydrophobic drugs used mainly in the market. Extending the measurement into hydrophobic molecules with lower diffusivity may slow down the rate and sustain the release.

Chapter 5: Conclusions and Future Perspective

Chapter 5: Conclusions and Future Perspective

Complications associated with drug eluting stents arise from its vulnerability to in-stent thrombosis. This is directly attributed to late regeneration of endothelial cells, lining the blood vessels, injured during mechanical perfusion of the vessel. Furthermore, undesired events can be associated with potential hypersensitivity of local biological medium to stent polymeric coating. In this thesis, a biologically active, and possibly drug bearing system was proposed to replace polymeric coating on stent as surface modification. This system comprises self-grown nanoarchitectures for Ti-17Nb-6Ta alloy that has potential for use in fabricating self-expandable stents.

Two nanotube (NTs) morphologies were successfully fabricated for the same substrate using anodization technique: 1) Homo-NTs, characterized by highly ordered, vertically aligned nanotubes of uniform and homogeneous tubes diameter, closely packed into islands separated by grooves. 2) Hetero-NTs, characterized by highly ordered, vertically aligned nanotubes but of non-uniform and heterogeneous tubes diameter, yet, evenly distributed along the substrate. Different morphologies were obtained by using different types of electrolytes and conditions for anodization setup.

XRD and Raman analysis for the as-anodized samples indicated the formation of the anatase phase associated with annealed titania NTs. Possible overlapping of peaks from other alloying elements (Nb and Ta), hindered accurate compositional analysis using those two techniques. Therefore, XPS as more sensitive and highly powerful technique for elemental analysis was used. It was able to confirm the formation of mixture oxides of the alloying elements on the surface without totally losing one of the components during anodization. Elemental analysis was further confirmed with EDX, which showed Ti, Nb, Ta and O with overall composition relatively consistent with the composition of the substrate alloy.

Nanoindentation technique was used to obtain the Young's modulus and hardness values for the fabricated morphologies before and after annealing. It was reported that phase transformation occurred with samples annealed resulted in higher values of Young's modulus and hardness for both samples. Comparative observation between the two morphologies revealed that Homo-NTs showed the higher hardness, while Hetero-NTs gave higher stiffness values.

For influence of the proposed system on endothelial healing, both morphologies (Homo- and Hetero-NTs) were investigated *in-vitro* with cultured vascular endothelial cells. First, cytotoxicity study was done to assess the material biocompatibility. By using, MTT assay it was found that after incubation of samples' extracts with cells for 48 hours, concentration of viable cells were almost similar to cell control. Both morphologies as well as substrate material showed no cytotoxicity and were ready for further biological investigation. For proliferation studies Trypan blue cell count and MTT assay were undertaken for samples cultured with cells for 1, 3 and 7 days. Along the three time intervals, nanoarchitectures showed significantly better results for endothelial cells proliferation. Furthermore, Homo-NTs showed superior activity than Hetero-NTs for biological response.

Drug loading capacity was practically investigated and compared for the two morphologies using 2'- Deoxyadenosine drug. Results were as well in favor of Homo-NTs, which showed higher amount of drug retained from initially added concentration. The drug release profile for this system was then simulated and calculated through computational studies using COMSOL ® Multiphysics software with transport of diluted species module. Within a diffusion controlled physical model, a time dependent study calculated drug concentration released from the NTs into the tissue across time. It reported that almost 100% of the practically loaded amount would be eluted from the NTs within a duration of 3 days. Although this may be considered relatively fast rate for the intended application, it is expected that by increasing initially loaded amount, tuning tubes diameter and using hydrophobic drugs, more sustained release can be obtained.

Finally, for future perspectives some complimentary work can be suggested as follow:

- Further in-depth mechanical investigation of the NTs layer is required to ensure the mechanical integrity of the system during PTCA and on the long term within the vessel.
- Studying surface hydrophilicity, which may directly affect its interaction with blood components and thrombus formation.
- Effect of nanoarchitecture on VSMC proliferation that may influence restenosis.
- Practical investigation of drug release kinetics to support computational calculations.
- Investigating drug loading capacities and release profile with higher initial drug concentrations and for hydrophobic drugs.

References

1. O'Connell, B. M., McGloughlin, T. M. & Walsh, M. T. Factors that affect mass transport from drug eluting stents into the artery wall. *Biomed. Eng. Online* **9,** 2–16 (2010).

2. The top 10 causes of death, *World Health Organization*, (2008). Adapted from: <http://www.who.int/mediacentre /factsheets/fs310/en/index.html> , accessed on February 2015.

3. Mathers, C. D., Boerma, T. & Ma Fat, D. Global and regional causes of death. *British Medical Bulletin* **92,** 7–32 (2009).

4. McMahan, C. A., Gidding, S. S. & McGill, H. C. Coronary heart disease risk factors and atherosclerosis in young people. *Journal of Clinical Lipidology* **2,** 118–126 (2008).

5. Kaazempur-Mofrad, M. R., Wada, S., Myers, J. G. & Ethier, C. R. Mass transport and fluid flow in stenotic arteries: Axisymmetric and asymmetric models. *Int. J. Heat Mass Transf.* **48,** 4510–4517 (2005).

6. Martin, D. M. & Boyle, F. J. Drug-eluting stents for coronary artery disease: a review. *Med. Eng. Phys.* **33,** 148–163 (2011).

7. Pepine, C. The effects of angiotensin-converting enzyme inhibition on endothelial dysfunction: potential role in myocardial ischemia. *Am. J. Cardiol.* **82,** 23–27 (1998).

8. What Are the Signs and Symptoms of Coronary Heart Disease?, *National Heart, Lung and Blood institute*, (2014). Adapted from: <http://www.nhlbi.nih.gov/health/health-topics/topics/cad/signs>, accessed on: February 2015.

9. Khan, W., Farah, S. & Domb, A. J. Drug eluting stents: developments and current status. *J. Control. Release* **161,** 703–12 (2012).

10. Ludman, P. F. Percutaneous coronary intervention. *Medicine* **38,** 438–445 (2010).

11. Burt, H. M. & Hunter, W. L. Drug-eluting stents: A multidisciplinary success story. *Adv. Drug Deliv. Rev.* **58,** 350–357 (2006).

12. Hospital Patient Flow, *Percutaneous transluminal coronary angioplasty*, (2014). Adapted from: <http://imgkid.com/percutaneous-transluminal-coronary-angioplasty-(ptca).shtml>, accessed on: February 2015.

13. Newsome, L. T., Kutcher, M. A. & Royster, R. L. Coronary artery stents: Part i. evolution of percutaneous coronary intervention. *Anesthesia and Analgesia* **107,** 552–569 (2008).

14. Wache, H. M., Tartakowska, D. J., Hentrich, a. & Wagner, M. H. Development of a polymer stent with shape memory effect as a drug delivery system. *J. Mater. Sci. Mater. Med.* **14,** 109–112 (2003).

15. Cardiovascular diseases, *Encyclopedia britannica*, (2010). Adapted from: <http://www.britannica.com/EBchecked/topic/720793/cardiovascular-disease/images-videos/95218/balloon-angioplasty>, accessed on: February 2015.

16. Mani, G., Feldman, M. D., Patel, D. & Agrawal, C. M. Coronary stents: A materials perspective. *Biomaterials* **28,** 1689–1710 (2007).

17. Winslow, R. D., Sharma, S. K. & Kim, M. C. Restenosis and drug-eluting stents. *Mt. Sinai J. Med.* **72,** 81–89 (2005).

18. Lagerqvist, B. *et al.* Long-term outcomes with drug-eluting stents versus bare-metal stents in Sweden. *N. Engl. J. Med.* **356,** 1009–1019 (2007).

19. Head, D. E., Sebranek, J. J., Zahed, C., Coursin, D. B. & Prielipp, R. C. A tale of two stents: perioperative management of patients with drug-eluting coronary stents. *J. Clin. Anesth.* **19,** 386–396 (2007).

20. Kaul, S., Shah, P. K. & Diamond, G. a. As Time Goes By. Current Status and Future Directions in the Controversy Over Stenting. *J. Am. Coll. Cardiol.* **50,** 128–137 (2007).

21. Hong, Y. J. & Jeong, M. H. New Drug-Eluting Stents. *Korean Circ.* **35,** 197–205 (2005).

22. Schwartz, S., Edelman, E. Preclinical Evaluation of Drug-Eluting Stents for Peripheral Applications. *Circulation* **110**, 2498–2505 (2004).

23. Costa, M. a. & Simon, D. I. Molecular basis of restenosis and drug-eluting stents. *Circulation* **111,** 2257–2273 (2005).

24. Sousa, J. E., Serruys, P. W. & Costa, M. a. New frontiers in cardiology: Drug-eluting stents: Part I. *Circulation* **107,** 2274–2279 (2003).

25. Gogas, B. D., McDaniel, M., Samady, H. & King, S. B. Novel Drug-Eluting Stents For Coronary Revascularization. *Trends Cardiovasc. Med.* **24,** 305–313 (2014).

26. Camenzind, E., Steg, P. G. & Wijns, W. Stent thrombosis late after implantation of first-generation drug-eluting stents: A cause for concern. *Circulation* **115,** 1440–1455 (2007).

27. Popma, J., Weiner, B., Cowley, M., Simonton, C., Mccormick, D., Feldman, T. FDA advisory panel on the safety and efficacy of drug-eluting stents: Summary of findings and recommendations. *J. Interv. Cardiol.* **20,** 425–446 (2007).

28. Bhatia, V. & Kaul, U. Coronary Stents- Safety Issues and Current Status. *Med. Updat.* **18,** 70– 75 (2008).

29. Jeewandara, T. M., Wise, S. G. & Ng, M. K. C. Biocompatibility of coronary stents. *Materials (Basel).* **7,** 769–786 (2014).

30. Levine, G., Blankenship, J., Bailey, S., Bittl, J., Cercek, B. ACCF/AHA/SCAI guideline for percutaneous coronary intervention: a report of the American College of Cardiology Foundation/American Heart Association Task Force on Practice Guidelines and the Society for Cardiovascular Angiography and Interventions. *Catheter. Cardiovasc. Interv.* **58,** 44–122 (2011).

31. AL-Mangour, B., Mongrain, R. & Yue, S. Coronary Stents Fracture: An Engineering Approach (Review). *Mater. Sci. Appl.* **04,** 606–621 (2013).

32. Raval, A., Choubey, A., Engineer, C. & Kothwala, D. Development and assessment of 316LVM cardiovascular stents. *Mater. Sci. Eng. A* **386,** 331–343 (2004).

33. Holton, A., Walsh, E., Anayiotos, A., Pohost, G. & Venugopalan, R. Comparative MRI compatibility of 316 L stainless steel alloy and nickel-titanium alloy stents. *J. Cardiovasc. Magn. Reson.* **4,** 423–430 (2002).

34. Okazaki, Y. & Gotoh, E. Metal release from stainless steel, Co-Cr-Mo-Ni-Fe and Ni-Ti alloys in vascular implants. *Corros. Sci.* **50,** 3429–3438 (2008).

35. Liu, C. L., Chu, P. K., Lin, G. Q. & Qi, M. Anti-corrosion characteristics of nitride-coated AISI 316L stainless steel coronary stents. *Surf. Coatings Technol.* **201,** 2802–2806 (2006).

36. Rittersma, S., De Winter, R., Koch, K., Bax, M., Schotborgh, C., Mulder, K., Tijssen, J., Piek, J. Impact of strut thickness on late luminal loss after coronary artery stent placement. *Am. J. Cardiol.* **93,** 477–480 (2004).

37. Poncin, P., Millet, C., Chevy, J. & Proft, J. Comparing and optimizing Co-Cr tubing for stent applications. *Mater Process. Med. Devices Conf.* 25–27 (2004).

38. O'Brien, B. & Carroll, W. The evolution of cardiovascular stent materials and surfaces in response to clinical drivers: A review. *Acta Biomater.* **5,** 945–958 (2009).

39. O'Brien, B. J., Stinson, J. S., Larsen, S. R., Eppihimer, M. J. & Carroll, W. M. A platinum-chromium steel for cardiovascular stents. *Biomaterials* **31,** 3755–3761 (2010).

40. Bhargava, B., De Scheerder, I., Ping, Q., Yanming, H., Chan, R., Kim, H., Kollum, M., Cottin, Y., Leon, M. A novel platinum-iridium, potentially gamma radioactive stent: Evaluation in a porcine model. *Catheter. Cardiovasc. Interv.* **51,** 364–368 (2000).

41. Windecker, S., Mayer, I., De Pasquale, G., Maier, W., Dirsch, O., Degroot, P., Wu, Y., Noll, G., Leskosek, B., Meier, B., Hess, O. Stent coating with titanium-nitride-oxide for reduction of neointimal hyperplasia. *Circulation* **104,** 928–933 (2001).

42. Biehl, V., Wack, T., Winter, S., Seyfert, U. T. & Breme, J. Evaluation of the haemocompatibility of titanium based biomaterials. **19,** 97–101 (2002).

43. Stoeckel, D., Pelton, A. & Duerig, T. Self-expanding Nitinol stents: Material and design considerations. *Eur. Radiol.* **14,** 292–301 (2004).

44. Ther, M. I., Technol, A., Duerig, T. W. & Wholey, M. A comparison of balloon- and self-expanding stents. *Min Invas Ther Allied Technol* **11,** 173–178 (2002).

45. Stentys Self-expanding Coronary Bare-Metal Stent System for Unusual Vessels, *Medgadget,* (2004). Adapted from: <http://www.medgadget.com/2010/03/ stentys_selfexpanding_coronary_baremetal_stent_system_for_unusual_vessels.html>, accessed on: March 2015.

46. Senthilnathan, K. Pseudoelastic shape memory alloy model with stent deployment simulation. Masters degree thesis, State University of New York at Buffalo, Department of Mechanical and Aerospace Egineering, (2010).

47. Hermawan, H., Dubé, D. & Mantovani, D. Developments in metallic biodegradable stents. *Acta Biomater.* **6,** 1693–1697 (2010).

48. Wang, X. *et al.* Polymeric stent materials dysregulate macrophage and endothelial cell functions: Implications for coronary artery stent. *Int. J. Cardiol.* **174,** 688–695 (2014).

49. Otsuki, S., Shiratori, Y., Brugaletta S., Cola, C., Del Blanco, B., Salmeron, R., Diaz, J., Pinar, E., Marti, V., Picart, J., Yuste, V., Sabate, M. Edge Vascular Response After Polymer-Free vs. Polymer-Based Paclitaxel-Eluting Stent Implantation. *Circ. J.* **78,** 2657–2664 (2014).

50. Garg, S. & Serruys, P. W. Coronary stents: Looking forward. *J. Am. Coll. Cardiol.* **56,** 43–78 (2010).

51. Abizaid, A. & Costa, J. R. New drug-eluting stents an overview on biodegradable and polymer-free next-generation stent systems. *Circ. Cardiovasc. Interv.* **3,** 384–393 (2010).

52. Wessely, R., Hausleiter, J., Michaelis, C., Jaschke, B., Vogeser, M., Milz, S., Behnisch, B., Schratzenstaller, T., Renke-Gluszko, M., Stöver, M., Wintermantel, E., Kastrati, A., Schömig, A. Inhibition of neointima formation by a novel drug-eluting stent system that allows for dose-adjustable, multiple, and on-site stent coating. *Arterioscler. Thromb. Vasc. Biol.* **25,** 748–753 (2005).

53. Byrne, R., Iijima, R., Mehilli, J., Pinieck, S., Bruskina, O., Schömig, A., Kastrati, A. Durability of Antirestenotic Efficacy in Drug-Eluting Stents With and Without Permanent Polymer. *JACC Cardiovasc. Interv.* **2,** 291–299 (2009).

54. Nakayama, Y., Nishi, S., Ishibashi-Ueda, H. & Matsuda, T. Surface microarchitectural design in biomedical applications: *In-vivo* analysis of tissue ingrowth in excimer laser-directed micropored scaffold for cardiovascular tissue engineering. *J. Biomed. Mater. Res.* **51,** 520–528 (2000).

55. Louizos, L. -a., Athanasopoulos, P. G. & Varty, K. Microelectromechanical Systems and Nanotechnology: A Platform for the Next Stent Technological Era. *Vasc. Endovascular Surg.* 46(8), 605–609 (2012).

56. Coronary Challenge, *Medical device network market*, (2015). Adapted from: <http://www.medicaldevice-network.com/features/feature98990/feature98990-2.html>, accessed on: March 2015.

57. Smith, B. S., Yoriya, S., Grissom, L., Grimes, C. a. & Popat, K. C. Hemocompatibility of titania nanotube arrays. *J. Biomed. Mater. Res.* **95 A,** 350–360 (2010).

58. Cui, C., Lui, H., Li, Y., Sun, J., Wang, R., Liu, S., Greer, A. Fabrication and biocompatibility of nano-TiO2/titanium alloys biomaterials. *Mater. Lett.* **59,** 3144–3148 (2005).

59. Kasuga, T., Hiramatsu, M., Hoson, A., Sekino, T., Niihara, K. Titania nanotubes prepared by chemical processing. *Adv. Mater.* **11,** 1307–1311 (1999).

60. Sander, M. S., Côté, M. J., Gu, W., Kile, B. M. & Tripp, C. P. Template-assisted fabrication of dense, aligned arrays of titania nanotubes with well-controlled dimensions on substrates. *Adv. Mater.* **16,** 2052–2057 (2004).

61. Adachi, M., Murata, Y., Harada, M. & Yoshikawa, S. Formation of Titania Nanotubes with High Photo-Catalytic Activity. *Chemistry Letters* **29**, 942–943 (2000).

62. Adachi, M., Murata, Y., Okada, I. & Yoshikawa, S. Formation of Titania Nanotubes and Applications for Dye-Sensitized Solar Cells. *Journal of The Electrochemical Society* **150,** G488–493 (2003).

63. Kisumi, T., Tsujiko, A., Murakoshi, K. & Nakato, Y. Crystal-face and illumination intensity dependences of the quantum efficiency of photoelectrochemical etching, in relation to those of water photooxidation, at n-TiO2 (rutile) semiconductor electrodes. *J. Electroanal. Chem.* **545,** 99–107 (2003).

64. Ahu Akin, F., Zreiqat, H., Jordan, S., Wijesundara, M. B. J. & Hanley, L. Preparation and analysis of macroporous TiO2 films on Ti surfaces for bone-tissue implants. *J. Biomed. Mater. Res.* **57,** 588–596 (2001).

65. Shin, H., Jeong, D. K., Lee, J., Sung, M. M. & Kim, J. Formation of TiO2 and ZrO2 nanotubes using atomic layer deposition with ultraprecise control of the wall thickness. *Adv. Mater.* **16,** 1197–1200 (2004).

66. Leskelä, M. & Ritala, M. Atomic layer deposition chemistry: recent developments and future challenges. *Angew. Chem. Int. Ed. Engl.* **42,** 5548–5554 (2003).

67. Guan, Y., Wang, L.-N., Yudong, Z., Lu, X. & Luo, J.-L. Nanotubular surface modification of metallic implants via electrochemical anodization technique. *Int. J. Nanomedicine* **9,** 4421–4435 (2014).

68. Zwilling, V., Aucouturier, M. & Darque-Ceretti, E. Anodic oxidation of titanium and TA6V alloy in chromic media. An electrochemical approach. *Electrochim. Acta* **45,** 921–929 (1999).

69. Gong, D., Grimes, A., Varghese, K., Hu, W., Singh, S., Chen, Z., Dickey, E. Titanium oxide nanotube arrays prepared by anodic oxidation. *Journal of Materials Research* **16,** 3331–3334 (2001).

70. Mor, G. K., Varghese, O. K., Paulose, M., Mukherjee, N. & Grimes, C. A. Fabrication of tapered, conical-shaped titania nanotubes. *Journal of Materials Research* **18,** 2588–2593 (2003).

71. Jun, Y., Park, J. H. & Kang, M. G. The preparation of highly ordered TiO2 nanotube arrays by an anodization method and their applications. *Chem. Commun.* **48,** 6456–6471 (2012).

72. Dawei Gong and Oomman K. Varghese, Wenchong Hu, R.S. Singh, and Zhi Chen, Elizabeth C. Dickey, C. A. G. Titanium oxide nanotube arrays prepared by anodic oxidation. *J. Mater. Res* **12,** 3331–3334 (2001).

73. Allam, N. K. & Grimes, C. A. Effect of cathode material on the morphology and photoelectrochemical properties of vertically oriented TiO2 nanotube arrays. *Sol. Energy Mater. Sol. Cells* **92,** 1468–1475 (2008).

74. Mor, G. K., Shankar, K., Paulose, M., Varghese, O. K. & Grimes, C. A. Use of highly-ordered TiO(2) nanotube arrays in dye-sensitized solar cells. *Nano Lett.* **6,** 215–218 (2006).

75. Jiang, W., Zeng, W., Ma, Z., Pan, Y., Lin, J., Chunsheng, L. Advanced amorphous nanoporous stannous oxide composite with carbon nanotubes as anode materials for lithium-ion batteries. *RSC Adv.* **4,** 41281–41286 (2014).

76. Macák, J. M., Tsuchiya, H., Ghicov, A. & Schmuki, P. Dye-sensitized anodic TiO2 nanotubes. *Electrochem. commun.* **7,** 1133–1137 (2005).

77. Zhu, K., Neale, N. R., Miedaner, A. & Frank, A. J. Enhanced charge-collection efficiencies and light scattering in dye-sensitized solar cells using oriented TiO2 nanotubes arrays. *Nano Lett.* **7,** 69–74 (2007).

78. Paulose, M., Shankar, K., Varghese, K., Mor, K., Hardin, B., Grimes, A. Backside illuminated dye-sensitized solar cells based on titania nanotube array electrodes. *Nanotechnology* **17,** 1446–1448 (2006).

79. Lin, L.-Y., Yeh, M., Lee, P., Chen, H., Vittal, R., Ho, C. Metal-based flexible TiO_2 photoanode with titanium oxide nanotubes as the underlayer for enhancement of performance of a dye-sensitized solar cell. *Electrochim. Acta* **57,** 270–276 (2011).

80. Chen, Q., Xu, D., Xu, Z., Liu, Z. Free-standing TiO 2 nanotube arrays made by anodic oxidation and ultrasonic splitting. *Nanotechnology* **19,** 365708 (2008).

81. Park, J. H., Lee, T.-W. & Kang, M. G. Growth, detachment and transfer of highly-ordered TiO2 nanotube arrays: use in dye-sensitized solar cells. *Chem. Commun. (Camb).* ***35****,* 2867–2869 (2008).

82. Paulose, M., Shankar, K., Yoriya, S., Prakasam, H., Varghese, O., Mor, G., LaTempa, J., Fitzgerald, A., Grimes, A. Anodic growth of highly ordered TiO2 nanotube arrays to 134 microm in length. *The journal of physical chemistry. B* **110,** 16179–16184 (2006).

83. Karthik, S., Gopal, M., Haripriya, P., Sorachon, Y., Maggie, P., Varghese, K., Grimes, A. Highly-ordered TiO 2 nanotube arrays up to 220 μm in length: use in water photoelectrolysis and dye-sensitized solar cells. *Nanotechnology* **18,** 65707 (2007).

84. Paulose, M., Parakasam, H., Varghese, K., Peng, L., Popat, C., Mor, G., Desai, A., Gimes, A. TiO 2 nanotube arrays of 1000 μm length by anodization of titanium foil: Phenol red diffusion. *J. Phys. Chem. C* **111,** 14992–14997 (2007).

85. Cai, Q., Paulose, M. & Grimes, C. a. The effect of electrolyte composition on the fabrication of self-organized titanium oxide nanotube arrays by anodic oxidation. *J. Mater. Res.* **20,** 230–236 (2005).

86. Ruan, C., Paulose, M., Varghese, O. K., Mor, G. K. & Grimes, C. A. Fabrication of highly ordered TiO2 nanotube arrays using an organic electrolyte. *J. Phys. Chem. B* **109,** 15754–15759 (2005).

87. Allam, N. K. & Grimes, C. A. Formation of vertically oriented TiO2 nanotube arrays using a fluoride free HCl aqueous electrolyte. *J. Phys. Chem. C* **111,** 13028–13032 (2007).

88. Hamlekhan, A. *et al.* Fabrication of anti-aging TiO2 nanotubes on biomedical Ti alloys. *PLoS One* **9,** 1–10 (2014).

89. Varghese, O. K. Crystallization and high-temperature structural stability of titanium oxide nanotube arrays. *Mater. Res. Soc.* **18,** 156–165 (2003).

90. Mor, G. K., Varghese, O. K., Paulose, M., Shankar, K. & Grimes, C. A. A review on highly ordered, vertically oriented TiO2 nanotube arrays: Fabrication, material properties, and solar energy applications. *Solar Energy Materials and Solar Cells* **90,** 2011–2075 (2006).

91. Ghicov, A., Tsuchiya, H., Macak, J. M. & Schmuki, P. Annealing effects on the photoresponse of TiO 2 nanotubes. *Phys. Status Solidi* **203,** R28–R30 (2006).

92. Zhao, J., Wang, X., Sun, T. & Li, L. Crystal phase transition and properties of titanium oxide nanotube arrays prepared by anodization. *J. Alloys Compd.* **434,** 792–795 (2007).

93. Yang, Y., Wang, X. & Li, L. Crystallization and phase transition of titanium oxide nanotube arrays. *J. Am. Ceram. Soc.* **91,** 632–635 (2008).

94. Wang, D., Yu, B., Wang, C., Zhou, F. & Liu, W. A novel protocol toward perfect alignment of anodized TiO2 nanotubes. *Adv. Mater.* **21,** 1964–1967 (2009).

95. Lee, K., Kim, D., Roy, P., Paramasivam, I., Birajdar, I., Spiecker, E., Schmuki, P. Anodic formation of thick anatase TiO2 mesosponge layers for high-efficiency photocatalysis. *J. Am. Chem. Soc.* **132,** 1478–1479 (2010).

96. Schmidt-Stein, F., Thiemann, S., Berger, S., Hahn, R. & Schmuki, P. Mechanical properties of anatase and semi-metallic TiO2 nanotubes. *Acta Mater.* **58,** 6317–6323 (2010).

97. Xiong, J., Wang, X., Li, Y. & Hodgson, P. D. Interfacial chemistry and adhesion between titanium dioxide nanotube layers and titanium substrates. *J. Phys. Chem. C* **115,** 4768–4772 (2011).

98. Yu, D., Zhu, X., Xu, Z., Zhong, X., Gui, Q., Song, Y., Zhang, S. Facile Method to Enhance the Adhesion of TiO 2 Nanotube Arrays to Ti Substrate. 8001–8005 (2014).

99. Ghicov, A., Aldabergenova, S., Tsuchiya, H. & Schmuki, P. TiO2–Nb2O5 Nanotubes with Electrochemically Tunable Morphologies. *Angew. Chemie - Int. Ed.* **45,** 6993–6996 (2006).

100. Shrestha, N. K., Nah, Y.-C., Tsuchiya, H. & Schmuki, P. Self-organized nano-tubes of TiO2-MoO3 with enhanced electrochromic properties. *Chem. Commun. (Camb).* 2008–2010 (2009).

101. Yang, Y., Kim, D. & Schmuki, P. Electrochromic properties of anodically grown mixed V2O 5-TiO2 nanotubes. *Electrochem. commun.* **13,** 1021–1025 (2011).

102. Yang, M., Jha, H., Liu, N. & Schmuki, P. Increased photocurrent response in Nb-doped TiO2 nanotubes. *Journal of Materials Chemistry* **21,** 15205 (2011).

103. Nah, Y. C., Ghicov, A., Kim, D., Berger, S. & Schmuki, P. TiO2-WO3 composite nanotubes by alloy anodization: Growth and enhanced electrochromic properties. *J. Am. Chem. Soc.* **130,** 16154–16155 (2008).

104. Kim, D., Fujimoto, S., Schmuki, P. & Tsuchiya, H. Nitrogen doped anodic TiO2 nanotubes grown from nitrogen-containing Ti alloys. *Electrochem. commun.* **10,** 910–913 (2008).

105. Jha, H., Hahn, R. & Schmuki, P. Ultrafast oxide nanotube formation on TiNb, TiZr and TiTa alloys by rapid breakdown anodization. *Electrochim. Acta* **55,** 8883–8887 (2010).

106. Kamkin, A. N., Fishgoit, L. A. & Davydov, A. D. Composition and Structure of Anodic Oxide Films on Titanium-Aluminum Alloys by Fast Electron Reflection Diffraction, Rutherford Backscattering, and Secondary Neutral Particle Mass Spectrometry. *Russ. J. Electrochem.* **39,** 665–670 (2003).

107. Yasuda, K., Schmuki, P. & Yasuda, B. K. Formation of Self-Organized Zirconium Titanate Nanotube Layers by Alloy Anodization. *Adv. Mater.* **19,** 1757–1760 (2007).

108. Vasilev, K., Poh, Z., Kant, K., Chan, J., Michelmore, A., Losic, D. Tailoring the surface functionalities of titania nanotube arrays. *Biomaterials* **31,** 532–540 (2010).

109. Park, J., Bauer, S., Schmuki, P. & Mark, K. Narrow Window in Nanoscale Dependent Activation of Endothelial Cell Growth and Differentiation on TiO 2 Nanotube Surfaces. *Nano Lett.* **9,** 3157–3164 (2009).

110. Minagar, S., Wang, J., Berndt, C. C., Ivanova, E. P. & Wen, C. Cell response of anodized nanotubes on titanium and titanium alloys. *J. Biomed. Mater. Res. - Part A* **101 A,** 2726–2739 (2013).

111. Webster, T. J., Ergun, C., Doremus, R. H., Siegel, R. W. & Bizios, R. Enhanced functions of osteoblasts on nanophase ceramics. *Biomaterials* **21,** 1803–1810 (2000).

112. Hamlekhan, A., Butt, A., Patel, S., Royhman, D., Takoudis, C., Sukotjo, C., Yuan, J., Jurish, G., Mathew, M., Hendrickson, W., Virdi, A., Shokufar, T. Fabrication of anti-aging TiO2 nanotubes on biomedical Ti alloys. *PLoS One* **9,** 1–11 (2014).

113. Oh, S. & Jin, S. Titanium oxide nanotubes with controlled morphology for enhanced bone growth. *Mater. Sci. Eng. C* **26,** 1301–1306 (2006).

114. Wang, N., Li, H., Lu, W., Li, J., Wang, J., Zhang, Z., Liu, Y. Effects of TiO2 nanotubes with different diameters on gene expression and osseointegration of implants in minipigs. *Biomaterials* **32,** 6900–6911 (2011).

115. Kang, C., Park, Y., Choi, H., Oh, S., Lee, K., Choi, S., Shim, J. Osseointegration of Implants Surface-Treated with Various Diameters of TiO 2 Nanotubes in Rabbit. *J. Nanomater.* **2015,** 1–11 (2015).

116. Steele, J. G., Dalton, B. A., Johnson, G. & Underwood, P. A. Polystyrene chemistry affects vitronectin activity: an explanation for cell attachment to tissue culture polystyrene but not to unmodified polystyrene. *J. Biomed. Mater. Res.* **27,** 927–940 (1993).

117. Giordano, C. *et al.* Electrochemically induced anatase inhibits bacterial colonization on Titanium Grade 2 and Ti6Al4V alloy for dental and orthopedic devices. *Colloids Surfaces B Biointerfaces* **88,** 648–655 (2011).

118. Terriza, A., Diaz, A., Yubero, F., Barranco, A., Gonzalez, R., Caballero, G., Vilches, J., Salido, M. Light induced hydrophilicity and osteoblast adhesion promotion on amorphous TiO2. *J. Biomed. Mater. Res. - Part A* **101 A,** 1026–1035 (2013).

119. Chang, W.-Y., Fang, T.-H., Chiu, Z.-W., Hsiao, Y.-J. & Ji, L.-W. Nanomechanical properties of array TiO2 nanotubes. *Microporous Mesoporous Mater.* **145,** 87–92 (2011).

120. Uchida, M., Kim, H.-M., Kokubo, T., Fujibayashi, S. & Nakamura, T. Structural dependence of apatite formation on titania gels in a simulated body fluid. *J. Biomed. Mater. Res. A* **64,** 164–170 (2003).

121. De Scheerder, I., Verbeken, E. & Humbeeck, J. Van. Metallic surface modification. *Semin. Interv. Cardiol.* **3,** 139–144 (1997).

122. Tepe, G., Wendel, P., Khorchidi, S., Schumel, J., Wiskirchen, J., Pusich, B., Claussen, D., Duda, H. Thrombogenicity of various endovascular stent types: an *in-vitro* evaluation. *J. Vasc. Interv. Radiol.* **13,** 1029–1035 (2002).

123. Palmaz, J. C., Benson, A. & Sprague, E. A. Influence of surface topography on endothelialization of intravascular metallic material. *J. Vasc. Interv. Radiol.* **10,** 439–444 (1999).

124. Palmaz, J. C., Bailey, S., Marton, D. & Sprague, E. Influence of stent design and material composition on procedure outcome. *Journal of Vascular Surgery* **36,** 1031–1039 (2002).

125. Sprague, E. A., Luo, J. & Palmaz, J. C. Human aortic endothelial cell migration onto stent surfaces under static and flow conditions. *J. Vasc. Interv. Radiol.* **8,** 83–92 (1997).

126. Van Belle, E., Tio, O., Chen, D., Maillard, L., Chen, D., Kearney, M., Isner, M. Passivation of metallic stents after arterial gene transfer of phVEGF165 inhibits thrombus formation and intimal thickening. *J. Am. Coll. Cardiol.* **29,** 1371–1379 (1997).

127. Van Belle, E., Bauters, C., Asahara, T. & Isner, J. M. Endothelial regrowth after arterial injury: From vascular repair to therapeutics. *Cardiovascular Research* **38,** 54–68 (1998).

128. Inoue, T., Croce, K., Morooka, T., Sakuma, M., Node, K., Simon, I. Vascular inflammation and repair: Implications for re-endothelialization, restenosis, and stent thrombosis. *JACC Cardiovasc. Interv.* **4,** 1057–1066 (2011).

129. Finn, A. V., Joner, M., Nakazawa, G., Kolodgie, F., Newell, J., John, C., Gold, K., Virmani, R. Pathological correlates of late drug-eluting stent thrombosis: Strut coverage as a marker of endothelialization. *Circulation* **115,** 2435–2441 (2007).

130. Nakazawa, G. Stent thrombosis of drug eluting stent: Pathological perspective. *Journal of Cardiology* **58,** 84–91 (2011).

131. Doi, K. & Matsuda, T. Enhanced vascularization in a microporous polyurethane graft impregnated with basic fibroblast growth factor and heparin. *J. Biomed. Mater. Res.* **34,** 361–370 (1997).

132. Nakayama, Y., Nishi, S. & Ishibashi-Ueda, H. Fabrication of drug-eluting covered stents with micropores and differential coating of heparin and FK506. *Cardiovasc. Radiat. Med.* **4,** 77–82 (2003).

133. Dibra, A., Kastrati, A., Mehilli, J., Pache, J., Von Oepen, R., Dirschinger, J., Schomeg, A. Influence of stent surface topography on the outcomes of patients undergoing coronary stenting: A randomized double-blind controlled trial. *Catheter. Cardiovasc. Interv.* **65,** 374–380 (2005).

134. Ma, X., Wu, T. & Robich, M. P. Drug-eluting stent coatings. *Interventional Cardiology* **4,** 73–83 (2012).

135. Wieneke, H. *et al.* Synergistic Effects of a Novel Nanoporous Stent Coating and Tacrolimus on Intima Proliferation in Rabbits. *Catheter. Cardiovasc. Interv.* **60,** 399–407 (2003).

136. Martinez, A. W. & Chaikof, E. L. Microfabrication and nanotechnology in stent design. *Wiley Interdisciplinary Reviews: Nanomedicine and Nanobiotechnology* **3,** 256–268 (2011).

137. Kollum, M. *et al.* Particle debris from a nanoporous stent coating obscures potential antiproliferative effects of tacrolimus-eluting stents in a porcine model of restenosis. *Catheter. Cardiovasc. Interv.* **64,** 85–90 (2005).

138. Brammer, K. S., Oh, S., Gallagher, J. O. & Jin, S. Enhanced cellular mobility guided by TiO2 nanotube surfaces. *Nano Lett.* **8,** 786–793 (2008).

139. Peng, L., Eltgroth, M. L., LaTempa, T. J., Grimes, C. a. & Desai, T. a. The effect of TiO2 nanotubes on endothelial function and smooth muscle proliferation. *Biomaterials* **30,** 1268–1272 (2009).

140. Peng, L., Barckzak, J., Barbeau, A., Xiao, Y., LaTempa, J., Grimes, A., Desai, A. Whole genome expression analysis reveals differential effects of TiO2 nanotubes on vascular cells. *Nano Lett.* **10,** 143–148 (2010).

141. Mohan, C., Sreerekha, R., Divyarani, V., Nair, S., Chennazhi, K., Menon, D. Influence of titania nanotopography on human vascular cell functionality and its proliferation *in-vitro*. *J. Mater. Chem.* **22,** 1326–1340 (2012).

142. Grimes, C. a., Mor, G. K. Use of TiO2 arrays for biological applications, TiO2 Nanotube Arrays. *Springer science + Business media, LLC* 285–314 (2009).

143. Popat, K. C., Eltgroth, M., LaTempa, T. J., Grimes, C. a. & Desai, T. a. Titania nanotubes: A novel platform for drug-eluting coatings for medical implants? *Small* **3,** 1878–1881 (2007).

144. Kang, H.-J., Kim, D. J., Park, S.-J., Yoo, J.-B. & Ryu, Y. S. Controlled drug release using nanoporous anodic aluminum oxide on stent. *Thin Solid Films* **515,** 5184–5187 (2007).

145. Kwak, D.-H., Yoo, J.-B. & Kim, D. J. Drug release behavior from nanoporous anodic aluminum oxide. *J. Nanosci. Nanotechnol.* **10,** 345–348 (2010).

146. Losic, D., Aw, S., Santos, A., Gulati, K., Bariana, M., Aw, S. Titania nanotube arrays for local drug delivery : recent advances and perspectives. *Expert Opin. Drug Deliv.* 1–25 (2014).

147. Ayon, A., Cantu, M., Chava, K., Agrawal, M., Feldman, D., Johnson, D., Patel, D., Marton, D., Shi, E. Drug loading of nanoporous TiO2 films. *Biomed. Mater.* **1,** L11–L15 (2006).

148. Popat, K. C., Eltgroth, M., LaTempa, T. J., Grimes, C. a. & Desai, T. a. Decreased Staphylococcus epidermis adhesion and increased osteoblast functionality on antibiotic-loaded titania nanotubes. *Biomaterials* **28,** 4880–4888 (2007).

149. Zhang, Z., Sun, Y., Tian, A., Xue, X., Wang, L., Alcuhali, A., Bai, Z. Improved antibacterial activity and biocompatibility on vancomycin-loaded TiO2 nanotubes: *In-vivo* and *in-vitro* studies. *Int. J. Nanomedicine* **8,** 4379–4389 (2013).

150. Yao, C. & Webster, T. J. Prolonged antibiotic delivery from anodized nanotubular titanium using a co-precipitation drug loading method. *J. Biomed. Mater. Res. - Part B Appl. Biomater.* **91,** 587–595 (2009).

151. Chennell, P., Feschet-Chassot, E., Devers, T., Awitor, O., Descamps, S., Sautou, V. *In-vitro* evaluation of TiO2 nanotubes as cefuroxime carriers on orthopaedic implants for the prevention of periprosthetic joint infections. *Int. J. Pharm.* **455,** 298–305 (2013).

152. Zhao, L., Wang, H., Huo, K., Cui, L., Zhang, W., Ni, H., Zhang, Y., Wu, Z., Chu, P. Antibacterial nano-structured titania coating incorporated with silver nanoparticles. *Biomaterials* **32,** 5706–5716 (2011).

153. Huo, K., Zhang, X., Wang, H., Zhao, L., Liu, X., Chu, K. Osteogenic activity and antibacterial effects on titanium surfaces modified with Zn-incorporated nanotube arrays. *Biomaterials* **34,** 3467–3478 (2013).

154. Ma, M., Kazemzadeh, M., Hui, Y., Lu, S., Ding, C., Chen, Y., Hancock, W., Wang, R. Local delivery of antimicrobial peptides using self-organized TiO(2) nanotube arrays for peri-implant infections. *J. Biomed. Mater. Res. Part A* **100,** 278–285 (2012).

155. Lai, S., Zhang, W., Lui, F., Wu, C., Zeng, D., Sun, Y., Xu, Y., Fang, Y., Zhou, W. TiO2 Nanotubes as Animal Drug Delivery System and *In-vitro* Controlled Release. *J. Nanosci. Nanotechnol.* **13,** 91–97 (2013).

156. Jia, H. & Kerr, L. Sustained Ibuprofen Release Using Composite Poly(Lactic-co-Glycolic Acid)/Titanium Dioxide Nanotubes from Ti Implant Surface. *J. Pharm. Sci.* **102,** 2341–2348 (2013).

157. Gulati, K., Ramakrishnan, S., Aw, S., Atkins, J., Findlay, M., Losic, D. Biocompatible polymer coating of titania nanotube arrays for improved drug elution and osteoblast adhesion. *Acta Biomater.* **8,** 449–456 (2012).

158. Shokuhfar, T., Sinha-Ray, S., Sukotjo, C. & Yarin, A. L. Intercalation of anti-inflammatory drug molecules within TiO2 nanotubes. *RSC Adv.* **3,** 17380–17386 (2013).

159. Aw, M. S., Addai-Mensah, J. & Losic, D. A multi-drug delivery system with sequential release using titania nanotube arrays. *Chemical Communications* **48,** 3348 (2012).

160. Neupane, P., Park, S., Bae, S., Yi, K., Uo, M., Watari, F., Lee, H. Titania nanotubes supported gelatin stabilized gold nanoparticles for medical implants. *Journal of Materials Chemistry* **21,** 12078 (2011).

161. Lai, M., Cai, K., Zhao, L., Chen, X., Hou, Y., Yang, Z.. Surface Functionalization of TiO 2 Nanotubes with Bone Morphogenetic Protein 2 and Its Synergistic Effect on the Differentiation of Mesenchymal Stem Cells. **12**, 1097–1105 (2011).

162. Koo, T.-H., Borah, J., Xing, Z., Moon, S., Jeong, Y., Kang, I. Immobilization of pamidronic acids on the nanotube surface of titanium discs and their interaction with bone cells. *Nanoscale Res Lett* **8,** 1–9 (2013).

163. Kodama, A., Bauer, S., Komatsu, A. Asoh, H., Ono, S., Schmuki, P. Bioactivation of titanium surfaces using coatings of TiO2 nanotubes rapidly pre-loaded with synthetic hydroxyapatite. *Acta Biomater.* **5,** 2322–2330 (2009).

164. Zhao, L., Wang, H., Huo, K., Zhang, X., Wang, W., Zhang, Y., Wu, Z., Chu, P. The osteogenic activity of strontium loaded titania nanotube arrays on titanium substrates. *Biomaterials* **34,** 19–29 (2013).

165. Moon, S. H., Lee, J., Park, S., Lee, H., Soh, J., Bae, S., Kim, S. Bioactivity of Ti-6Al-4V alloy implants treated with ibandronate after the formation of the nanotube TiO 2 layer. *Journal of Biomedical Materials Research - Part B **8**, 2053–2059 Applied Biomaterials* (2012).

166. Wei, H., Wu, S., Feng, Z., Zhou, W., Dong, Y., Wu, G., Bai, S., Zhao, Y. Increased fibroblast functionality on CNN2-loaded titania nanotubes. *Int. J. Nanomedicine* **7,** 1091–1100 (2012).

167. Gulati, K., Atkins, G. J., Findlay, D. M. & Losic, D. Nano-engineered titanium for enhanced bone therapy. *Biosensing and Nanomedicine* **6,** 1–6 (2013).

168. Chen, X. Cai, K., Fang., Lai, M., Hou, Y., Li, J., Luo, Z., Hu, Y., Tang, L. Fabrication of selenium-deposited and chitosan-coated titania nanotubes with anticancer and antibacterial properties. *Colloids Surfaces B Biointerfaces* **103,** 149–157 (2013).

169. Program, B. E. & Falls, S. A Polymer-Free Paclitaxel Eluting Coronary Stent : Effects of Solvents , Drug Concentrations and Coating Methods. **42,** 1170–1184 (2014).

170. Xiao, X. Yang, L., Guo, M., Pan, C., Cai, Q., Yao, S. Biocompatibility and *in-vitro* antineoplastic drug-loaded trial of titania nanotubes prepared by anodic oxidation of a pure titanium. *Sci. China, Ser. B Chem.* **52,** 2161–2165 (2009).

171. Daemen, J., Wenaweser, P., Tsuchida, K., Abrecht, L., Vaina, S., Morger, C., Kukreja, N., Juni, P, Sianos, G., Hellige, G., Van Domburg, R., Hess, O., Boersma, E., Meier, B., Windecker, S., Serryus, W. Early and late coronary stent thrombosis of sirolimus-eluting and paclitaxel-eluting stents in routine clinical practice: data from a large two-institutional cohort study. *Lancet* **369,** 667–678 (2007).

172. Gulati, K., Aw, M. S. & Losic, D. Nanoengineered drug-releasing Ti wires as an alternative for local delivery of chemotherapeutics in the brain. *Int. J. Nanomedicine* **7,** 2069–2076 (2012).

173. Liu, W., Gao, J., Zhang, F. & Zhang, G. Preparation of TiO2 Nanotubes and Their Photocatalytic Properties in Degradation Methylcyclohexane. *Mater. Trans.* **48,** 2464–2466 (2007).

174. Sharmoukh, W. & Allam, N. K. TiO_2 nanotube-based dye-sensitized solar cell using new photosensitizer with enhanced open-circuit voltage and fill factor. *ACS Appl. Mater. Interfaces* **4,** 4413–8 (2012).

175. Maiyalagan, T., Viswanathan, B. & Varadaraju, U. V. Fabrication and characterization of uniform TiO2 nanotube arrays by sol-gel template method. *Bull. Mater. Sci.* **29,** 705–708 (2006).

176. Thamaphat, K., Limsuwan, P. & Ngotawornchai, B. Phase Characterization of TiO 2 Powder by XRD and TEM. *Kasetsart J. (Nat. Sci.)* **42,** 357–361 (2008).

177. Liu, H., Ding, D., Ning, C. & Li, Z. Wide-range hydrogen sensing with Nb-doped TiO2 nanotubes. *Nanotechnology* **23,** 015502 (2012).

178. Arbiol, J., Cerda, J., Dezanneau, G., Cirera, A., Peiro, F., Cornet, A., Morante, J. Effects of Nb doping on the TiO2 anatase-to-rutile phase transition. *J. Appl. Phys.* **92,** 853–861 (2002).

179. Altomare, M., Lee, K., Killian, M. S., Selli, E. & Schmuki, P. Ta-doped TiO2 nanotubes for enhanced solar-light photoelectrochemical water splitting. *Chem. - A Eur. J.* **19,** 5841–5844 (2013).

180. Jang, S. H., Choe, H. C., Ko, Y. M. & Brantley, W. A. Electrochemical characteristics of nanotubes formed on Ti-Nb alloys. *Thin Solid Films* **517,** 5038–5043 (2009).

181. Clima, S., Pourtoit, G., Sven , E., Stefan, G., Marc, H., Dirk, W., Jorge, K. Dielectric Response of Ta2O5, Nb2O5, and NbTaO5 from First-Principles Investigations. *J. Electrochem. Soc.* **157,** G20–G25 (2010).

182. Choe, H. C. Nanotube and Micropore of Ti Alloy Systems for Biocompatibility. *Mater. Sci. Forum* **654-656,** 2061–2064 (2010).

183. Aldabergenova, S. B., Ghicov, A., Albu, S., Macak, J. M. & Schmuki, P. Smooth titania nanotubes: Self-organization and stabilization of anatase phase. *J. Non. Cryst. Solids* **354,** 2190–2194 (2008).

184. Kress, S., Neumann, A., Weyand, B. & Kasper, C. Stem cell differentiation depending on different surfaces. *Adv. Biochem. Eng. Biotechnol.* **126,** 263–83 (2012).

185. Liu, X., Chu, P., Ding, C. Surface modification of titanium, titanium alloys, and related materials for biomedical applications. *Mate.r Sci. Eng*. **121**, 47–49 (2004).

186. Long, M., Rack, H. Titanium alloys in total joint replacement – a materials science perspective. *Biomater*. **19**, 1621–1639 (1998).

187. Sul, Y., Johansson, C., Petronis, S., Krozer, A., Jeong, Y., Wennerberg, A. Characteristics of the surface oxides on turned and electrochemically oxidized pure titanium implants up to dielectric breakdown: the oxide thickness, micropore configurations, surface roughness, crystal structure and chemical composition. *Biomater*. **23**, 491–501 (2002).

188. Yang, B., Uchida, M., Kim, H., Zhang, X., Kokubo, T. Preparation of bioactive titanium metal via anodic oxidation treatment. *Biomater*. **25**, 1003–1010 (2004).

189. Dyer, C., Leach, J. Breakdown and efficiency of anodic oxide growth on titanium. *Electrochem. Soc*. **125**, 1032–1038 (1978).

190. Marchenoir, J., Loup, J., Masson, J. Study of porous layers formed by anodic- oxidation of titanium at high voltages. *Thin Solid Films*. **369**, 66–357 (1980).

191. Smith, I., Liu, X., Smith, L., Ma, P. Nanostructured polymer scaffoldsfor tissue engineering and regenerative medicine. *Wiley interdisciplinary reviews-Nanomedicine and nanobiotechnology*. **2**, 226–236 (2009).

192. Mongrain, R., Faik, I., Leask, R., Rodés-Cabau, J., Larose, É., Bertrand, O. Effects of diffusion coefficients and struts apposition using numerical simulations for drug eluting coronary stents. *Biomechanical Eng*. **129**, 733–742 (2007).

193. Ferrero, D., Doelker, E. Towards elucidation of the drug release mechanism from compressed hydrophilic matrices made of cellulose ethers. II. Evaluation of a possible swelling-controlled drug release mechanism using dimensionless analysis. *J Control Release*. **141**, 223-33 (2010).